

---

# Probing Single Molecules and Binding Networks

Ferdinand Greiss

---

Dissertation



München, Januar 2017



# Probing Single Molecules and Binding Networks

DETECTION OF SINGLE MOLECULES ON THE MULTI-CELLULAR SCALE WITH REFLECTED  
LIGHT-SHEET MICROSCOPY AND PROBING THE COOPERATIVITY OF BINDING NETWORKS  
WITH HIGH-THROUGHPUT THERMOPHORESIS

Dissertation  
zur Erlangung des Grades  
Doktor der Naturwissenschaften (Dr.rer.nat.)

an der Fakultät für Physik  
der Ludwig-Maximilians-Universität  
München



vorgelegt von

**Ferdinand Greiss**

aus München

Erstgutachter: Prof. Dr. Dieter Braun

Zweitgutachterin: Prof. Dr. Petra Schwille

Eingereicht am: 17. Januar 2017

Tag der mündlichen Prüfung: 9. März 2017



# Zusammenfassung

Biologische Prozesse haben sich im Lauf der Zeit aus den Interaktionen einzelner Moleküle zur Orchestrierung ganzer Organismen entwickelt. Biophysikalische Messplattformen fördern das Wissen über jeden dieser Schritte und werden dabei helfen die unterschiedlichen Aspekte zu vereinen. In dieser Arbeit wurden zwei quantitative Methoden für die Biophysik entwickelt. Beide repräsentieren Instanzen, die an den verschiedenen Enden des Spektrums sitzen: Die Untersuchung einzelner Moleküle und die Charakterisierung von Bindungsnetzwerken.

In der Literatur wurde reflektierende Lichtscheibenmikroskopie verwendet, um die vorteilhaften Eigenschaften der freien 3D-Abbildung und die Empfindlichkeit zum Detektieren einzelner Moleküle zu kombinieren. Die Technik verwendet einen Spiegel, der das Lichtblatt auf die Brennebene des Erfassungsobjektivs reflektiert. In dieser Arbeit wurde ein fixiertes Mikropisma eingeführt, das die Verwendung von Objektiven mit hoher numerischer Apertur erlaubt und die optische Ausrichtung vereinfacht. Gemeinsam wurden einzelne 10 kDa Dextran-Alexa647 Moleküle tief im *Drosophila* Embryo im Spätstadium etwa 80  $\mu\text{m}$  über dem Deckglas aufgenommen. Die Detektion und Verfolgung auf der multizellulären Ebene zeigte unterschiedliche Verhaltensweisen, die stark mit dem jeweiligen Ort korrelierten. Während im Perivitellin-Raum Brownsche Bewegung nachgewiesen werden konnte, wurde ein aktiver Transport in einzelnen Zellen der Epidermis beobachtet. Durch komplementäre Beobachtungen mit Rab5-GFP wurde der aktive Transport von Vesikeln dem endosomalen Transport zugeschrieben. Der Nachweis von Einzelmolekülen auf der multizellulären Ebene bei verschiedenen Probertiefen ermöglicht und fördert die Untersuchung ihrer Rolle wie der Bindung von DNA als Transkriptionsfaktoren.

Die Bildung supramolekularer Komplexe findet sich in vielen biologischen Systemen und ist die Grundlage für kooperatives Verhalten. Zu diesem Zweck wurde eine Strategie als zweites Projekt entwickelt, um die Affinität von Molekülen in komplexen Bindungsnetzwerken zu untersuchen. Unter Verwendung des Prinzips der Thermophorese wurde eine Hochdurchsatz-Plattform entworfen, um Affinitäten in kleinen Volumina von 500 nL und standardisierten 1536 Microplatten zu messen. Die Plattform ermöglichte die thermodynamische Aufklärung eines heterotrimeren DNA-Komplexes, der die Struktur und topologische Eigenschaft biologischer Systeme widerspiegelt. Jeder intermediäre Bindungszustand wurde gleichzeitig mit einem einzigen Fluoreszenzfarbstoff untersucht. Durch systematische Basenpaar-Variationen wurde eine gekoppelte Bindung zwischen scheinbar unabhängigen Bindungsstellen gefunden, die aus der Struktur des Drei-Wege-Übergangs hervorgeht.

Zusammen zeigen die beiden Projekte komplementäre biophysikalische Methoden und geben Einblicke in die Einzelmolekül-Diffusivität auf multizellulärer Ebene und der Bildung von Komplexen auf molekularer Ebene.



# Abstract

Biological processes have evolved from the simple interaction of two molecules to the orchestration of entire organisms. Biophysical measurement platforms advance the knowledge about each of these fields and help to eventually combine all the pieces. In this work, the different aspects of biology were tackled with two newly developed quantitative methods for biophysics. Both represent instances sitting at the different ends of the spectrum: the investigation of single molecules and the characterization of binding networks.

In literature, reflective light-sheet microscopy was employed to combine the beneficial attributes of free 3D imaging and the sensitivity to detect single molecules. The technique employs a mirror that reflects the light sheet onto the focal plane of the detection objective in order to selectively excite the sample. In this work, a fixed micro prism with reflective surface allowed to employ high numerical aperture objectives while keeping the optical alignment procedure at a minimum. Together, single 10 kDa Dextran-Alexa647 molecules were recorded deep in the late-stage *Drosophila* embryo roughly 80  $\mu\text{m}$  above the cover slip surface. The detection and tracking on the multi-cellular scale revealed different behaviors that strongly correlated with the respective location. While Brownian motion was detected in the perivitelline space, active transportation was observed in individual cells of the epidermis. With complementary experiments using Rab5-GFP, the active transportation of vesicles was attributed to endosomal trafficking. The detection of single molecules on the multi-cellular scale at different sample depths enables and fosters to study their role such as transcription factor binding to DNA.

The formation of supramolecular complexes is found in many biological systems and is the basis for cooperative behavior. To this end, a strategy was developed as second project to probe the affinity of molecules in complex binding networks. Using the principle of thermophoresis, a high-throughput platform was designed to measure affinities in small volumes of 500 nL and standard 1,536 well plates. The platform enabled to elucidate the thermodynamic properties of a heterotrimeric DNA complex that portrays the structure and topological property of biological systems. Each intermediate binding state was probed simultaneously with one single fluorescent dye. Through systematic base pair variations, a coupled binding between seemingly independent binding sites was found to arise from the structure of the three-way junction. In conclusion, the thermodynamic characterization of arbitrary binding networks improves the basic understanding of relevant processes such as self-assembly and complex formation.

Together, the two projects present complementary biophysical methods and give insight into the single molecule diffusivity on the multi-cellular level and the formation of supramolecular complexes on the molecular one.



# Contents

<b>Abstract (English/Deutsch)</b>	
<b>List of figures</b>	<b>vii</b>
<b>List of tables</b>	<b>ix</b>
<b>1 Introduction</b>	<b>1</b>
<b>2 Single Molecule Imaging in living <i>Drosophila</i> Embryos with Reflected Light-Sheet Microscopy</b>	<b>3</b>
2.1 Introduction and Motivation . . . . .	4
2.1.1 Noise & Background . . . . .	4
2.1.2 The Frontiers of Fluorescence Microscopy . . . . .	6
2.2 Results and Discussion . . . . .	7
2.2.1 Optical Setup . . . . .	7
2.2.2 3D Imaging Capabilities . . . . .	10
2.2.3 Single Molecule Imaging <i>In Vivo</i> . . . . .	10
2.3 Conclusion . . . . .	15
2.4 Materials and Methods . . . . .	16
2.4.1 Optical Setup . . . . .	16
2.4.2 Light-Sheet Characterization . . . . .	16
2.4.3 3D Volume Imaging . . . . .	17
2.4.4 Image Processing - FFT Filtering . . . . .	17
2.4.5 <i>In Vivo</i> Single Molecule Experiments . . . . .	17
<b>3 Probing Binding Networks with High-Throughput Thermophoresis</b>	<b>19</b>
3.1 Motivation and Introduction . . . . .	20
3.1.1 Cooperativity and Binding Networks in Nature . . . . .	21
3.1.2 Biophysical Instrumentation . . . . .	21
3.1.3 The Principles of Thermophoresis . . . . .	22
3.1.4 Two-State Binding Model . . . . .	23
3.2 Results . . . . .	25

## Contents

---

3.2.1	High-Throughput Thermophoresis Binding Assay . . . . .	25
3.2.2	Heterotrimeric Binding Networks . . . . .	26
3.3	Discussion and Conclusion . . . . .	33
3.4	Materials and Methods . . . . .	34
3.4.1	Assembly of the High-Throughput Thermophoresis Assay . . . . .	34
3.4.2	ATP Aptamer . . . . .	35
3.4.3	Synthetic DNA Binding Network . . . . .	35
3.4.4	Simulation and Optimization of Heterotrimeric Binding Networks . . . . .	36
<b>A</b>	<b>Assorted Project</b>	<b>37</b>
A.1	Numerical Benchmarking of Standing-Wave Multi-Focal Microscopy for Rapid Volume Imaging . . . . .	38
A.1.1	Introduction and Motivation . . . . .	38
A.1.2	Technology . . . . .	38
A.1.3	Numerical Simulations . . . . .	40
A.1.4	Conclusions . . . . .	42
<b>B</b>	<b>Supporting Material</b>	<b>43</b>
B.1	Single Molecule Imaging in living <i>Drosophila</i> Embryos with Reflected Light- Sheet Microscopy . . . . .	44
B.2	Probing Binding Networks with High-Throughput Thermophoresis . . . . .	45
	<b>Bibliography</b>	<b>57</b>
	<b>Associated Publications</b>	<b>59</b>

# List of Figures

2.1	Signal-to-background ratio in fluorescence microscopy . . . . .	5
2.2	Assembly of a reflected light-sheet microscope . . . . .	7
2.3	Geometry of the light sheet with different beam input diameters . . . . .	8
2.4	Volume imaging with <i>Drosophila</i> embryos . . . . .	9
2.5	Single molecule detection and tracking in the late-stage <i>Drosophila</i> embryo . .	11
2.6	Fast Fourier transform (FFT) algorithm to optimize raw images . . . . .	13
2.7	Active transport of single particles on multi-cellular scale . . . . .	14
3.1	The complexity of biological binding networks . . . . .	20
3.2	The principles of thermophoresis and binding curves . . . . .	23
3.3	High-throughput micro-scale thermophoresis platform . . . . .	25
3.4	Principle of heterotrimeric binding network . . . . .	27
3.5	Experimental data of synthetic DNA binding networks . . . . .	29
3.6	Error estimation . . . . .	31
A.1	Optical setup for standing-wave multi-focal microscopy . . . . .	39
A.2	Simulated single particle images for widefield, SW-MFM, and light sheet mi- croscopy . . . . .	40
A.3	Images of simulated spheres with different illumination strategies . . . . .	41
B.1	Implementation of the reflected light-sheet microscope . . . . .	44
B.2	Supplementing binding curve between A-Cy5 and C . . . . .	45
B.3	The principle of bootstrapping confidence intervals . . . . .	45
B.4	LabView control software for HT-MST . . . . .	46
B.5	LabView analysis software for HT-MST (MST Analysis 1.0.vi) . . . . .	47





## List of Tables

3.1	Estimated Gibbs free energy for individual steps in the heterotrimeric DNA binding networks . . . . .	32
3.2	Pseudo-code of high-throughput micro-scale thermophoresis workflow . . . .	34
3.3	DNA sequences for synthetic heterotrimeric binding network . . . . .	36



# 1 Introduction

Social, physical, and chemical networks have at least one thing in common: They are described by their nature of interactions: strength, topology, and temporal behavior. With all the possible combinations employed, the life forms of today were able to evolve from rather simple chemical material to the emergent economies of complex multicellular systems (beehive, fish school, bird flock, ...). In biological networks, the complexity explodes as one tries to further include the various cell types and fascinating strategies for communication on the different spatial scales.

Hence, the reduction of systems to their functional minimum is a contemporary approach to get a systematic view on these subjects. The problem is tackled from both directions, bottom-up and top-down. So, either the approach consists of building biological systems from their isolated parts or, on the other side, to reduce the complexity to its minimal constituents. A popular mind-set in this regard is that - in order to understand life - one has to be able to build or engineer it (Elowitz and Lim, 2010). Nonetheless, the bioengineering of systems does not start by randomly changing the unknown system, but firstly through observation and study. Only after initial experiments, the objective of changing parameters, conditions, or environments, can begin, starting the recursive cycle of learning and testing. To advance our understanding and to develop precise models with predictive power, a quantitative biophysical characterization is required. My work tries to improve on methods which utilization allows the quantitative description of biological systems. I motivate and describe the two methods in the following chapters:

- The observation of single molecules and their behavior on the multi-cellular scale with **reflected light-sheet microscopy**
- The study of biological binding networks with a **high-throughput micro-scale thermophoresis instrument**



## **2** Single Molecule Imaging in living *Drosophila* Embryos with Reflected Light-Sheet Microscopy

Modified and partially reproduced with permission from:

Greiss, F., Deligiannaki, M., Jung, C., Gaul, U., & Braun, D. (2016). Single-Molecule Imaging in Living *Drosophila* Embryos with Reflected Light-Sheet Microscopy. *Biophysical Journal*, 110(4), 939–946. <http://doi.org/10.1016/j.bpj.2015.12.035>

Copyright ©2016 Biophysical Society. Published by Elsevier Inc.

Contributions:

F.G. and D.B. constructed the optical setup and F.G. analyzed the data. F.G. and M.D. performed the experiments. F.G., M.D., C.J., U.G., and D.B. contributed to designing the experiments, discussion, and writing the manuscript.

## 2. Single Molecule Imaging in living *Drosophila* Embryos with Reflected Light-Sheet Microscopy

---

### 2.1 Introduction and Motivation

Technological advances made it possible for molecular biology to be studied on the single molecule level in living cells. The behavior of single macromolecules answers interesting questions that were formerly hidden in the ensemble-averaged experiments. For instance, what is the search mechanism of transcription factors for their binding site? How do they propagate through the densely packed environment of a nucleus? Does their movement couple distant gene loci? Many biological questions were or will be answered through single-molecule observations (Xie et al., 2008).

For the field of single-molecule research, far-field fluorescence microscopy is the essential tool to noninvasively and selectively probe the position of single fluorophores with nanometer precision and millisecond time resolution. The high autofluorescence background present in living organisms often prevents from imaging at such high accuracy. In addition to sample preparation (Sanamrad et al., 2014) and fluorescent labeling (Izeddin et al., 2014), optical background rejection is the major challenge in modern fluorescence microscopy. Here, the problem and partial solutions of fluorescence background is discussed.

#### 2.1.1 Noise & Background

The useful information that is contained within a single microscopy image is characterized by the signal-to-noise (S/N) ratio

$$S/N = \frac{S}{\sigma} \quad (2.1)$$

where  $S$  is the number of photons from the signal of interest and  $\sigma$  the total noise level. Since the fluorescence emission rates of fluorescent dyes peak at  $\sim 10^8 \text{ s}^{-1}$ , reducing the background signal is the contemporary objective to optimize in far-field fluorescence microscopy (Sandison and Webb, 1994).

Shot noise gives a lower limit on the noise level of optical methods. The noise level obeys a Poisson distribution which sets the mean and variance value to be equal. The noise is given by  $\sigma = \sqrt{S+B}$  where  $B$  is the number of photons generated by the background signal. The sensor noise  $n_S$  further introduces a noise source that needs to be considered and finally gives the ratio

$$S/N = \frac{S}{\sqrt{S+B+n_S^2}} \quad (2.2)$$

A simple model without detector noise was published with different background rejection

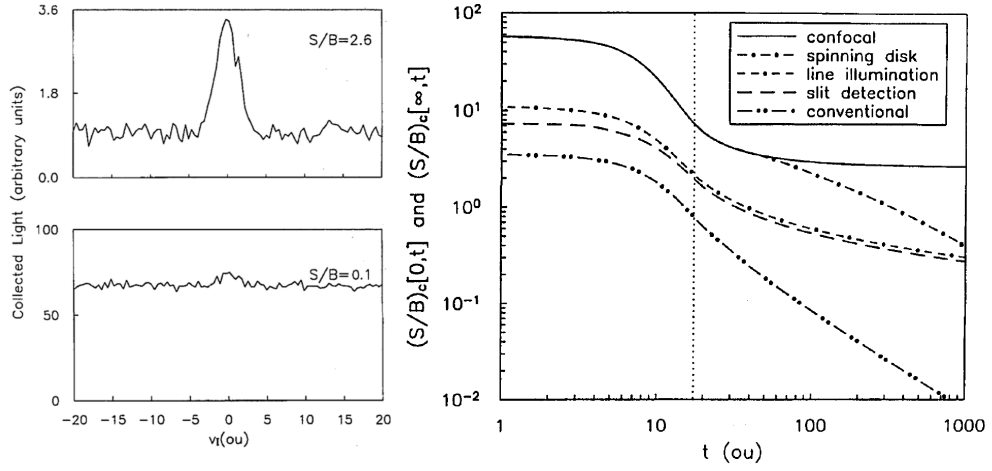


**Figure 2.1** – Signal-to-Background (S/B) ratio. Illustrative graph of point source in the presence of two different background levels. The background signal covers the actual signal at low signal-to-background (S/B) ratios. The dependence of the S/B ratio for a continuous sample on microscope geometry and sample thickness  $t$  in optical units (ou). As consideration, the first lateral and axial zeros of the point-spread function are  $3.83$  ou and  $4\pi$  ou, respectively. Illustrations is taken from (Sandison and Webb, 1994)

methods (Sandison and Webb, 1994). In the discussion, the signal  $S$  originates from a continuous sample larger than the point-spread function (PSF) with a number of fluorescent molecules  $N_d = c_0 V_e$ . The sample sits in the center of a volume of thickness  $t$  immersed by a uniform background  $B$  (auto-fluorescence). The relation between S/N and the signal-to-background ratio (S/B) is then given by

$$S/N = S^{1/2} \sqrt{\frac{S/B}{1 + S/B}} \quad (2.3)$$

In Fig. 2.1, a point source on the optical axis is simulated with different levels of background signal. The data highlights the importance of the S/B ratio for the excavation of information from noisy images. The S/B ratio is further plotted for different techniques of optical sectioning (various microscopy geometries).

They found that the background of confocal microscopy depends exclusively on the size of the detection aperture  $\nu_D$  with  $1.4\pi\nu_D^2$  and stays constant as soon as the volume thickness exceeds the confocal excitation volume. In contrast, the background of conventional microscopy increases with volume thickness according to  $4\pi(0.97t - 7.9)$ . The non-radial aperture geometries introduce higher background level and the spinning disk geometry loses S/B when the different excitation beams overlap. In conclusion, the optical sectioning is able to reduce the background signal with little to no reduction in the collection efficiency. However, except for

## 2. Single Molecule Imaging in living *Drosophila* Embryos with Reflected Light-Sheet Microscopy

---

spinning disk, all scanning methods reduce the temporal resolution drastically and render single-molecule imaging difficult. More advanced methods are therefore discussed in the next section.

### 2.1.2 The Frontiers of Fluorescence Microscopy

With its excellent S/N ratio, total-internal-reflection microscopy (TIRFM) is widely used for single molecule studies *in vitro* and to observe membrane-associated events at the single molecule level *in vivo* (Li and Xie, 2011; Ulbrich and Isacoff, 2007). While out-of-focus signal is greatly reduced by the selective excitation of only a few hundred nanometers, TIRFM is, however, intrinsically restricted to image regions near a refractive index mismatch.

Highly inclined laminated microscopy (HILO) was developed for three-dimensional single molecule imaging within single cells and has been shown to be able to detect single membrane proteins in living animals by virtue of optimized protein labeling (Zhan et al., 2014). Difficulties arise, however, when an attempt is made to image dense regions where the increased HILO light sheet thickness lowers the S/N ratio (Tokunaga et al., 2008).

### Light-Sheet Microscopy

Originally developed for imaging morphogenetic processes on a multicellular scale (Huisken, 2004), light-sheet microscopy (LSM) offers the most promising addition to single molecule imaging techniques (Chen et al., 2014; Ritter et al., 2010; Gebhardt et al., 2013; Friedrich et al., 2009; Galland et al., 2015). Several groups have been able to demonstrate protein binding to DNA in the nucleus of salivary gland cells (Ritter et al., 2010) and stem cell spheroids (Chen et al., 2014). Samples are optically sectioned via sheet-like excitation volumes parallel to the focal plane of the detection objective. The orthogonal arrangement of illumination and detection objective restricts the use to low to medium numerical aperture objectives that results in a poor photon transmission efficiency. Maximizing photon yield is however crucially needed for single molecule imaging.

In this work, the principles of reflected light-sheet microscopy (RLSM) were adapted as introduced by Gebhardt et al. (Gebhardt et al., 2013) and recently implemented as single-objective RLSM (soSPIM) by Galland et al. (Galland et al., 2015). RLSM uses a small reflective element to circumvent the spatial limitations imposed by conventional LSM. The excitation light beam is deflected shortly after the illumination objective onto the focal plane of a detection objective. The following sections show that the alignment can be readily performed with commercially available micro prisms that are attached to standard microscope cover slips (custom made by Optikron GmbH, Jena, Germany). Thus, samples can be placed directly onto the disposable platform while avoiding time-consuming handling or preparation steps. In fact, the 3D

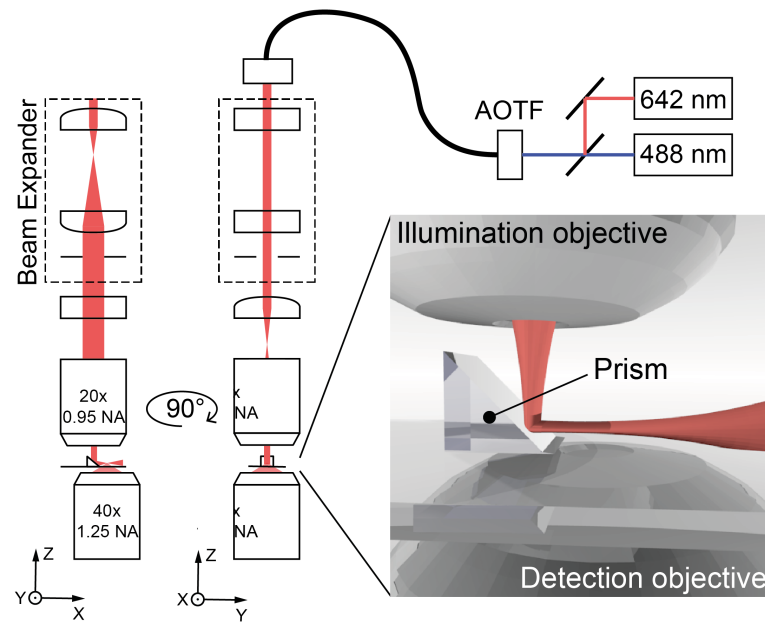


**Figure 2.2** – Assembly of a reflected light-sheet microscope. 642 nm and 488 nm laser lines are modulated via AOTF and coupled into the optical system. A cylindrical beam expander forms an enlarged elliptical beam profile. Within the beam expander, the diameter of the illumination beam is adjusted using a spherical aperture that controls the final beam waist along the Z axis in the sample plane. A cylindrical lens conjugates the back focal plane of the illumination objective to give a collimated beam along the Y axis in the sample plane. The light sheet is reflected via a micro prism onto the focal plane of a high-NA detection objective. The setup is illustrated from two different directions to highlight the elliptical beam geometry.

epidermal structure was reconstructed and, moreover, single Dextran-Alexa647 molecules were observed in the surrounding of the epidermis of living and highly opaque late-stage *Drosophila* embryos.

## 2.2 Results and Discussion

### 2.2.1 Optical Setup

The assembly of the optical setup with opposed detection and illumination objective was realized with a few custom-made and commercial parts on an inverted microscope. An autonomous illumination module with lasers, acousto-optic tunable filter (AOTF) and single-mode optical fiber were assembled to easily connect the light source with the actual microscope. Achromatic lenses were used to maintain constant dimensions of the beam input diameter across different illumination wavelengths. A maximal beam input diameter of ~12 mm was obtained with the 5x beam expander and the calibrated spherical aperture. A 150

## 2. Single Molecule Imaging in living *Drosophila* Embryos with Reflected Light-Sheet Microscopy

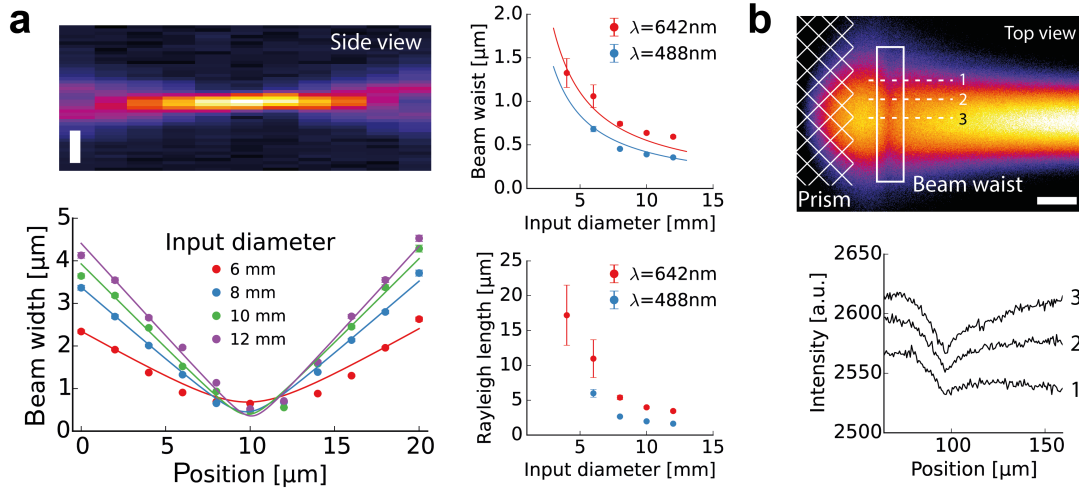


**Figure 2.3** – Geometry of the light sheet with different beam input diameters. (a) Raw data of measured light sheet profile along propagation direction every 2 μm without reflection at 488 nm. Vertical scale bar, 2 μm. Gaussian beam propagation and fits are shown for 488 nm and 4 different beam input diameters. Beam waist and Rayleigh length were extracted from fits for 488 nm and 642 nm. (b) Imaging of the light sheet after reflection of the micro prism in Cy5 in water. Line profiles are shown for 3 different positions along the light sheet width. Scale bar, 40 μm.

mm achromatic cylindrical lens controlled the light sheet width by conjugating the back focal plane of the illumination objective (Fig. 2.2).

The geometrical properties of the excitation light sheet were quantified with different beam input diameters. Therefore, the light sheet's cross-section was measured by projecting it without reflection onto the focal plane of the detection objective in water. By moving the detection objective across the beam waist in a step-wise fashion, the beam width was determined at 11 different propagation depths. The reconstructed profile was fitted to Gaussian beam propagation to obtain the beam waist for different beam input diameters (Fig. 2.3a). The beam waist was found to agree with the theory (Ritter, 2011) and is computed with

$$w = \frac{2\lambda f}{\pi n r} \quad (2.4)$$

where  $\lambda$  is the illumination wavelength,  $f$  the focal length of the illumination objective ( $f=9$  mm),  $n$  the refractive index of water ( $n=1.333$ ), and  $r$  the incident beam radius.

Furthermore, the light sheet profile was visualized after reflection of the micro prism by illuminating 500 nM Atto488 and Cy5 in water. By estimating the light sheet waist position along the detection objective's focal plane, a total light sheet tilt below  $\sim 1.5^\circ$  was achieved (Fig.

2.3b).

In the following experiments, a 642 nm laser line was used for single-molecule excitation, which results in lower autofluorescence from the biological sample, and the 488 nm laser line to localize the epidermal structure. The beam input diameter was adjusted to 7 mm in order to create a final light sheet of  $\sim 1 \mu\text{m}$  thickness ( $\sim 11 \mu\text{m}$  Rayleigh length) at 642 nm and  $\sim 0.6 \mu\text{m}$  ( $\sim 8 \mu\text{m}$  Rayleigh length) at 488 nm wavelength.

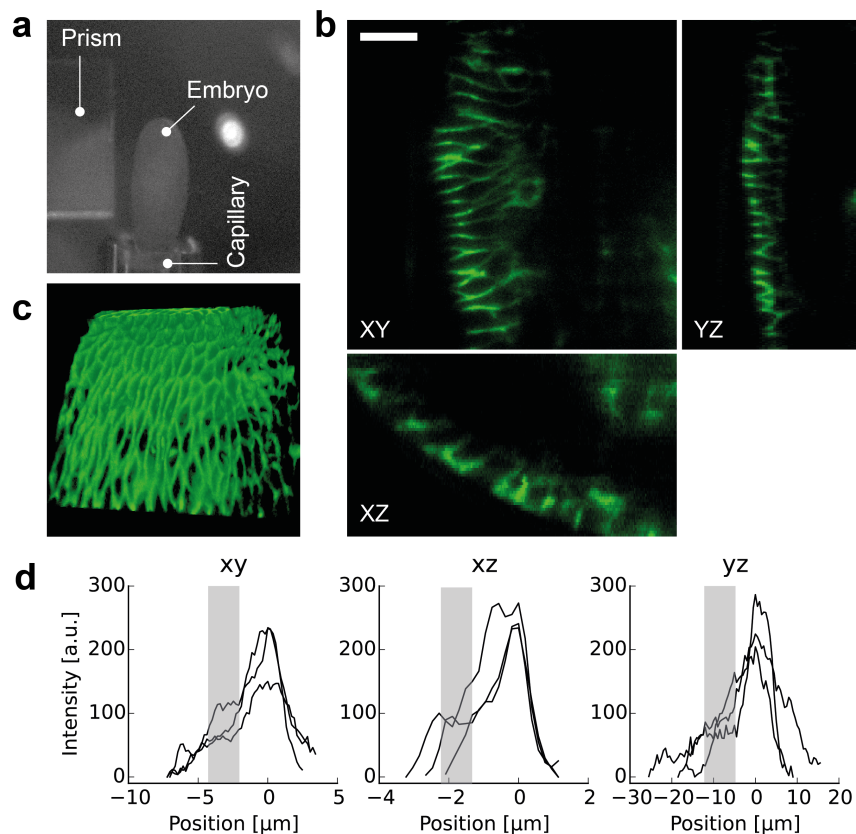


**Figure 2.4** – Volume imaging. (a) Positioning of *Drosophila* embryo with a capillary in front of the micro prism's reflective surface. A motorized linear actuator moved the capillary and the embryo in Z. (b) Orthogonal views of acquired images with  $0.5 \mu\text{m}$  resolution along Z. Scale bar,  $10 \mu\text{m}$ . NrgGFP accumulates at the apicolateral site of epithelial cells to hinder free diffusion along the paracellular space. (c) Reconstructed 3D volume of the epidermal structure. The  $\sim 1 \mu\text{m}$  light sheet thickness for optimal single molecule imaging is accompanied by a limited region of homogeneous illumination (Fig. 2.3). Thus, the 3D volume imaging was restricted on the outer epidermal layer. (d) Line profiles along the cell-cell junction revealed a  $\sim 2$ -fold increase in NrgGFP signal at the apicolateral site ( $0 \mu\text{m}$ ) compared to the basolateral site (gray bar) in all three space directions.

## 2. Single Molecule Imaging in living *Drosophila* Embryos with Reflected Light-Sheet Microscopy

---

### 2.2.2 3D Imaging Capabilities

To investigate the ability of 3D sectioning with the optical setup, a late-stage *Drosophila* embryo was positioned on the tip of a micro-scale capillary with 180  $\mu\text{m}$  inner diameter, expressing GFP-tagged Neuroglian (NrgGFP, Fig. 2.4a). Mounting the embryo with common heptane glue as used during live imaging of *Drosophila* with a confocal microscope on the glass capillary rendered a fast, robust and user-friendly way for micrometer positioning. A linear actuator offered a resolution of 0.5  $\mu\text{m}$  in Z-direction that was sufficient to obtain image stacks of the epidermal structure (Fig. 2.4).

It is important to note that the penetration depth is limited by light scattering as experienced with light sheet techniques. Furthermore, the light sheet thickness of  $\sim 1 \mu\text{m}$  provided a good S/N ratio for single molecule imaging, but reduced the applicability on the global embryonic scale. Therefore, the focus was laid on the outer epidermal structure to test the volume imaging capabilities of the RLSM implementation (Keller, Philipp J et al., 2010).

As a member of the membrane-associated septate junction (SJ) complex, Neuroglian is strongly expressed and readily detected with 13  $\mu\text{W}$  ( $\sim 130 \text{ W/cm}^2$ ) at an excitation wavelength of 488 nm. As expected, NrgGFP accumulated at the apicolateral site where the properly formed SJ complex impedes free diffusion along the paracellular space (Fig. 2.4b and c) (Genova, 2003). The data was further analyzed by measuring the intensity profile along the lateral membrane of some cells. Background-corrected intensity profiles (Fig. 2.4d) show intensity peaks (200-300 counts) at 0  $\mu\text{m}$  with lower intensity plateaus (gray bar, 50-100 counts). The roughly 2-fold increase of NrgGFP signal towards the apicolateral site holds true for all 3 spatial projections, which indicates homogeneous illumination within the region of interest.

### 2.2.3 Single Molecule Imaging *In Vivo*

In recent years, single molecule imaging was successfully applied to a wide array of biological specimen ranging from the nucleus of single eukaryotic cells (Chen et al., 2014; Ritter et al., 2010; Gebhardt et al., 2013; Galland et al., 2015) to membrane proteins in *C. elegans* (Zhan et al., 2014). To test, whether freely diffusing single molecules are detectable in the highly opaque *Drosophila* embryo (Keller, Philipp J et al., 2010) which presents an important model system in different fields of biology, a solution of 10 kDa Dextran was introduced as single molecule probe. It is being widely used for transportation studies in the biological context (Deligiannaki et al., 2015; Fabrowski et al., 2013; Pluen et al., 1999).

To this end, syncytial blastoderm embryos were collected and immediately injected with 10 kDa Dextran-Alexa647 and placed in a dark humid chamber. Embryos were staged (15 h AEL) and individually placed in water with their anterior-posterior axis parallel to the micro prism's reflective surface (Fig. 2.5a). 3D mounting was unpractical for this purpose, because high-

speed image acquisition is essential for single molecule imaging in solution. As schematically depicted in Figure 2.5a, the light sheet waist was positioned in the lower left quadrant, since optical aberrations along the illumination as well as the emission path worsened the S/N ratio when imaging in deeper tissue (Keller, Philipp J et al., 2010).

Since morphogenetic movement was negligible during the time scale of imaging, the GFP and Alexa647 channel could be acquired consecutively. Again, NrgGFP (488 nm laser line for excitation with  $60 \text{ W/cm}^2$ ) was used to adjust the light sheet and the focal position of the detection objective. Due to the interdependence of SJ proteins for localization, NrgGFP is now evenly distributed along the lateral membrane in the SJ mutant *pasiflora1 $\Delta$*  (Deligiannaki et al., 2015) and therefore clearly outlines the epidermal structure (Fig. 2.5b, center panel).

In the Alexa647 channel, immobilized intensity spots showed bleaching steps during the first few seconds of acquisition, confirming the detection of single molecules in living *Drosophila* embryos (1-2 dyes per Dextran according to manufacturer). Particle locations of bleaching step trajectories were found manually and their intensity was corrected for background signal. A locally dependent emission justifies the uneven level of signal counts for spatially separated fluorophores (Fig. 2.5d).

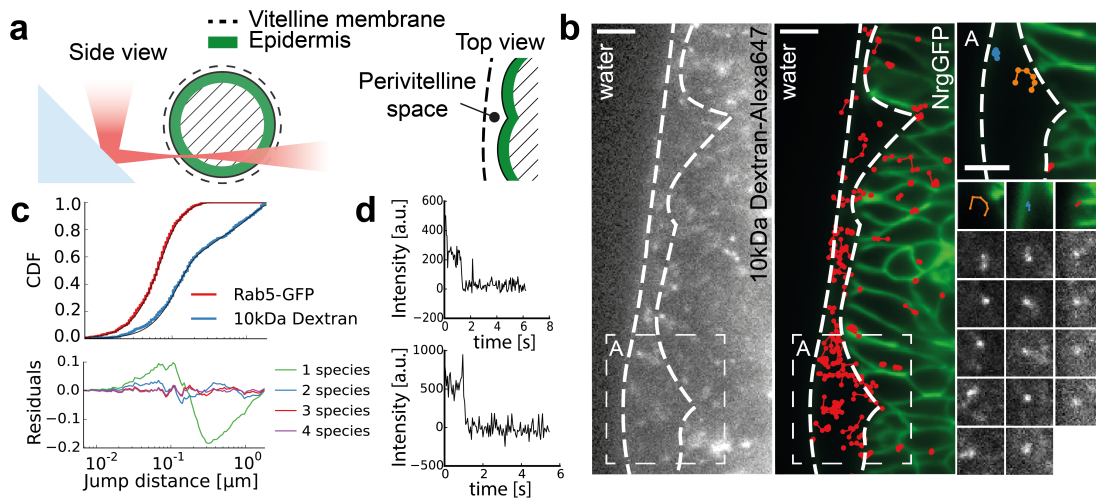


**Figure 2.5** – Single molecule detection and tracking. (a) Illustration of the excitation path and cross-section of embryo at the region of interest. Imaging at the lower left quadrant of the embryo reduced optical aberrations. (b) Single raw image of 10 kDa Dextran-Alexa647 and the temporal average of NrgGFP with superimposed trajectories. Scale bar,  $10 \mu\text{m}$ . Sub-region and tracks show examples for fast (left), medium (center), and slow (right) particles. Scale bar,  $5 \mu\text{m}$ . (c) Cumulative distribution function (CDF) of jump distances pooled from 3 different embryos and a 3-component model fitted. Additionally, CDF and fitted curve (2-component model) is shown for Rab5-GFP particles found in the *Drosophila* embryo (d) Two examples of Alexa647 bleaching steps found during the first seconds of imaging with the 642 nm laser line.

## 2. Single Molecule Imaging in living *Drosophila* Embryos with Reflected Light-Sheet Microscopy

---

Instead of the mean square displacement, the jump-distance distribution (Kues et al., 2001; Schütz et al., 1997; Crank, 1975; Chen et al., 2014) was used to study the diffusive behavior of single molecules. The jump-distance distribution is sampled by analyzing each single jump from  $t$  to  $t+1$  and, hence, allows the proper use of short trajectories and can be further extended to include multiple species with distinct diffusion coefficients. The probability of a particle jumping from its position at  $t$  to a shell of radius  $r$  and width  $dr$  at  $t+1$  is given by

$$p(r, t)dr = \frac{1}{4\pi D\tau} \exp\left(-\frac{r^2}{4D\tau}\right)2\pi r dr \quad (2.5)$$

where  $D$  is the diffusion coefficient and  $\tau$  the time delay. By integrating the probability function from  $\rho = 0$  to  $\rho = r$ , the cumulative distribution is obtained

$$P(r, \tau) = \int_0^r \frac{\rho}{2D\tau} \exp\left(-\frac{\rho^2}{4D\tau}\right) d\rho = 1 - \exp\left(-\frac{r^2}{4D\tau}\right) \quad (2.6)$$

The cumulative distribution of jump distances extracted from *Drosophila* embryos was fitted to models with 1, 2, 3, and 4 different numbers of species ( $=N$ ) using

$$P(r, \tau) = 1 - \sum_{i=1}^N A_i \exp\left(-\frac{r^2}{4D_i\tau}\right) \quad (2.7)$$

and  $\sum_{i=1}^N A_i = 1$ . Here,  $D_i$  and  $A_i$  are the diffusion coefficient and fraction of diffusive species  $i$ , respectively. The model quality was compared using residuals between predicted and actual data.

Before automatic tracking was utilized, the immobile fluorescent fraction and low frequency bleaching kinetics were first removed using a fast Fourier transform (FFT) algorithm (Fig. 2.6 and details see the Materials and Methods section). Prior to applying the FFT filter on the biological data, 46 nm diameter beads were imaged and tracked with and without filtered image sequences to exclude possible artifacts introduced by the proposed temporal filter. As seen in Figure 2.6b, no apparent difference between the cumulative distributions of both data sets could be observed. Fitting the jump distance cumulative distribution to a 1-component model, led to the same diffusion coefficient for both data sets ( $D_{raw} = 4.62 \pm 0.04 \mu\text{m}^2/\text{s}$ ,  $D_{FFT} = 4.63 \pm 0.03 \mu\text{m}^2/\text{s}$ ).

Single particles in *Drosophila* embryos were then detected and tracked with TrackMate after FFT filtering. Particles were excluded from further analysis when exceeding a certain size (diameter  $> 1.84 \mu\text{m}$ ) or tracks being outside of the expected lifetime range (3 frames  $\leq$  included

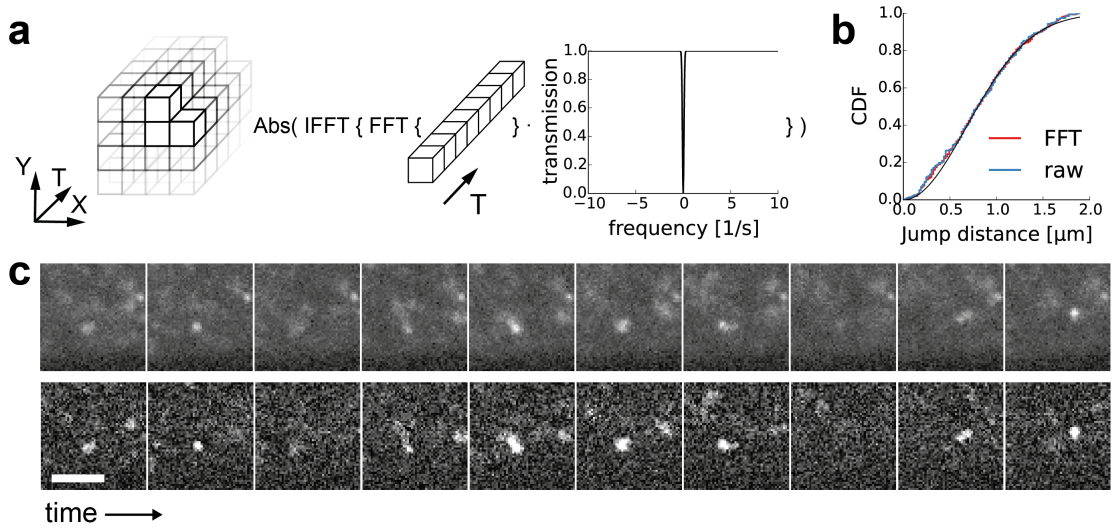


**Figure 2.6** – Image processing. (a) Every pixel in the image stack was independently processed using the temporal FFT filter. A Gaussian window was applied to remove immobile fraction and bleaching kinetics in order to improve the automatic spot detection. (b) Cumulative distribution function (CDF) of freely diffusing 46 nm diameter beads before and after FFT filtering. (c) Image sequences of freely diffusing 10 kDa Dextran-Alexa647 in *Drosophila* embryos are shown for unfiltered (upper row) and filtered (lower row) data sets. Scale bar, 5  $\mu\text{m}$ .

tracks  $\leq 30$  frames). The cumulative jump distance distribution for all tracks was fitted to models consisting of 1, 2, 3, and 4 components. The acquired data was best described by a 3-component model without overfitting as indicated by the calculated residuals (Fig. 2.5c;  $A_1 = 0.56$  with  $D_1 = 0.068 \pm 0.001 \mu\text{m}^2/\text{s}$ ,  $A_2 = 0.16$  with  $D_2 = 0.520 \pm 0.032 \mu\text{m}^2/\text{s}$  and  $A_3 = 0.28$  with  $D_3 = 6.404 \pm 0.072 \mu\text{m}^2/\text{s}$ ).

To investigate the spatial distribution of fast, medium, and slow diffusing components, the apparent diffusion coefficient was calculated for a time lag of 50 ms, averaged over all equally spaced time lags in each track and superimposed the color-coded mean track position onto the temporal averaged NrgGFP image stack. Diffusion coefficients are plotted on a log scale to account for the wide range of values (Fig. 2.7a). It appears that fast tracks ( $\sim 6.4 \mu\text{m}^2/\text{s}$ ) occur in the free space between vitelline membrane and epidermis. A similar diffusion coefficient of  $7 \mu\text{m}^2/\text{s}$  was reported for a 23 kDa morphogen in the extracellular space of living zebrafish embryos by FCS (Yu et al., 2009).

In contrast, slower particles were mostly found in the epidermal structure and seemed to obey directional movement, challenging the Brownian motion model. Mean square displacement curves for long trajectory acquisitions were fitted to the anomalous diffusion model

$$\langle x^2 \rangle = 4D\tau^\alpha \quad (2.8)$$

## 2. Single Molecule Imaging in living *Drosophila* Embryos with Reflected Light-Sheet Microscopy

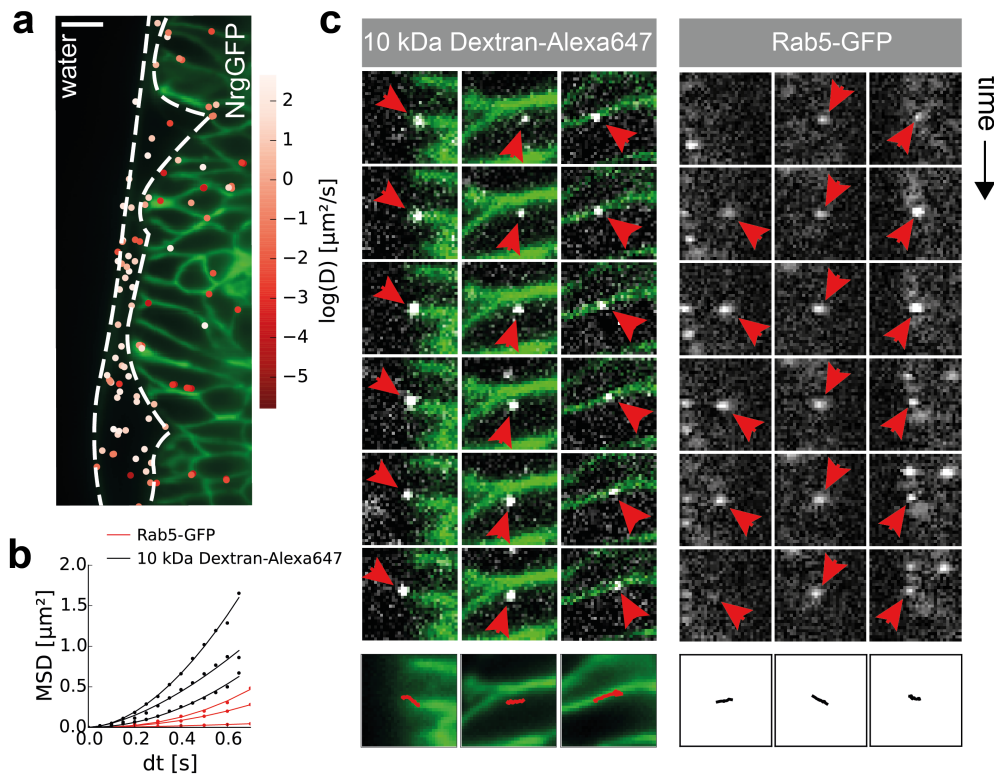


**Figure 2.7** – Spatial heterogeneity of diffusion. (a) Superimposed mean track position with color-coded apparent diffusion coefficient. The apparent diffusion coefficient was calculated for all equally spaced time lags of 50 ms along entire individual trajectories. Fast diffusion coefficients are mainly found in the perivitelline space. In contrast, slow particles are mostly found in the paracellular space or at the cell cortex of epidermal cells. Scale bar, 10  $\mu\text{m}$ . (c) Six representative time-lapse image sequences for particles associated with Dextran-Alexa647 (first three columns, green: NrgGFP) and Rab5-GFP (last three columns) with directional movement. Tracks were extracted and (b) MSD curves revealed anomalous diffusion coefficients of  $\alpha > 1$  for all six examples.

where  $D$  is the diffusion coefficient and  $\alpha$  is the exponent accounting for anomalous diffusion (Metzler and Klafter, 2000; Revery et al., 2015). Directional movement (active transportation of particles) was indicated by  $\alpha > 1$ . Slow particles were found to move in a directed manner along the cell cortex as well as the paracellular space (Fig. 2.7b and c;  $D_1 = 0.87 \pm 0.03 \mu\text{m}^2/\text{s}^{1.81}$ ,  $\alpha_1 = 1.81 \pm 0.05$ ;  $D_2 = 0.37 \pm 0.02 \mu\text{m}^2/\text{s}^{1.97}$ ,  $\alpha_2 = 1.97 \pm 0.09$ ;  $D_3 = 0.47 \pm 0.03 \mu\text{m}^2/\text{s}^{1.57}$ ,  $\alpha_3 = 1.57 \pm 0.08$ ). The slow directional movement of particles suggests active vesicle trafficking as a possible explanation. This interpretation is supported by a study that proposed dynamin-dependent vesicle transportation of morphogens ( $D = 0.10 \mu\text{m}^2/\text{s}$ ) during wing development in *Drosophila* (Kicheva et al., 2007). Additionally, previous experimental data found that  $\sim 80\%$  of Dextran-positive structures co-localize with the GFP-tagged endosomal marker Rab5 during cellularization of early *Drosophila* embryos (Fabrowski et al., 2013).

To further test the interpretation of endosomal trafficking, time-lapse movies were acquired in *Drosophila* embryos with Rab5-GFP expression. Before analysis, the image sequence was again processed using the FFT filter and the same frequency transmission window. The transportation direction appeared to align perpendicular to the anterior-posterior embryonic axis. The same preferred directionality could be observed for the Dextran-Alexa647 particles. Moreover, similar diffusion coefficients found by the cumulative distribution (Fig. 2.5c;  $A_1 = 0.78$  with  $D_1 = 0.0112 \pm 0.0001 \mu\text{m}^2/\text{s}$  and  $A_2 = 0.22$  with  $D_2 = 0.052 \pm 0.002 \mu\text{m}^2/\text{s}$ ) and the mean-square displacements (Fig. 2.7b;  $D_1 = 0.270 \pm 0.019 \mu\text{m}^2/\text{s}^{2.341}$ ,  $\alpha_1 = 2.341 \pm 0.138$ ;  $D_2 = 0.148 \pm 0.005 \mu\text{m}^2/\text{s}^{2.108}$ ,  $\alpha_2 = 2.108 \pm 0.007$ ;  $D_3 = 0.020 \pm 0.001 \mu\text{m}^2/\text{s}^{1.578}$ ,  $\alpha_3 = 1.578 \pm 0.046$ ) support the interpretation.

However, a key problem one has to keep in mind, is the comparison of fitted diffusion coefficients. The particle's transportation direction with respect to the imaging plane impairs the 2-dimensional tracking. Particles that translate along the light sheet will exhibit a higher diffusion coefficient than particles traversing across it.

## 2.3 Conclusion

Methodologically, this work showed that by adapting reflected light-sheet microscopy, single molecule imaging is readily achievable even within the highly opaque *Drosophila* embryo. Commercially available micro prisms offer a user-friendly and fast way to obtain the reflective surface that is necessary for RLSM. The setup could be easily supplemented with oil-immersion detection objectives that would, however, limit the accessible imaging depth. In principle, the same optical approach could be used for single-cells studies when grown in 3D cell culture. Yet, it is important to note that reflected light-sheet microscopy techniques are excluded from a few  $\mu\text{m}$  space above the coverslip surface because of their geometrical restrictions and consequently make the relative positioning of mirror and sample central (Gebhardt et al., 2013).

The presented RLSM implementation will not only offer an alternative to high-resolution imaging techniques, e.g. spinning disk microscopy, to image particles, but most importantly will give way to study the fundamental level of stochastic single molecule dynamics from the multicellular perspective. Additionally, biologically more relevant data for cell biology will be generated since the principles of light-sheet microscopy give the additional advantage of reduced photo-bleaching and photo-toxic effects (Pampaloni et al., 2015).

## 2. Single Molecule Imaging in living *Drosophila* Embryos with Reflected Light-Sheet Microscopy

---

### 2.4 Materials and Methods

#### 2.4.1 Optical Setup

Two laser lines were collinearly aligned via mirror and dichroic beam splitter (488 nm, 50 mW 488-50 Sapphire, Coherent Inc.; 642 nm, 140 mW, LuxX642, Omicron GmbH). Laser lines were modulated by an AOTF (AOTF4C-VIS-TN, Opto-Electronics) within a few  $\mu\text{s}$  and triggered with the camera TTL exposure output signal. The beam was collimated after the optical fiber by a reflective collimator (RC04FC-P01, Thorlabs) to a beam diameter of 4 mm. A cylindrical 5x Keplerian beam telescope expanded the beam diameter (cylindrical achromatic doublets 50/250 mm; ACY254-050-A/ACY254-250-A, Thorlabs). A spherical aperture (SM1D12C, Thorlabs) further controlled the final beam diameter (4 to 12 mm) and, hence, the light sheet thickness. A single cylindrical lens (150 mm cylindrical achromatic doublets, ACY254-150-A, Thorlabs) conjugated the back focal plane of a 20x and 0.95 NA water-immersion objective (XLUMPLFL20XWIR, Olympus, W.D.: 2 mm) to define the light sheet width. The entire optical illumination block was moved with a XYZ manual translation stage (PT3/M, Thorlabs) on a custom-made breadboard that was attached to a commercial inverted Zeiss (Axiovert Observer D1.m, Zeiss) microscope (Fig. 2.2 and Fig. B.1).

The coverslip (1.5#, 22x60 mm, Menzel) with custom attached 500x500x500  $\mu\text{m}$  micro prism (Optikron GmbH, Jena, Germany) was placed under the microscope to reflect the illumination beam onto the focal plane of a high-NA water-immersion objective (40x, 1.25NA, CFI Apochromat 40x WI Lambda-S, Nikon). Collected fluorescent signal was cleaned by a double-color emission-filter for 642 nm and 488 nm (ZET488/640, AHF Analysentechnik) and projected onto the EM-CCD camera (Cascade II 512, Photometrics) after further 2.5x magnification (2.5x C-Mount Adapter, Zeiss).

#### 2.4.2 Light-Sheet Characterization

Light sheet profiles were obtained by imaging the beam without reflection by the micro prism. By moving along the propagation direction of the illumination beam in a step-wise manner, cross sections at every position were extracted and fitted to  $g = a \exp(-2(x - b)^2 / w_z^2) + d$ , where  $b$  is the lateral shift,  $d$  the baseline,  $w_z$  the width of the Gaussian beam at propagation position  $z$ ,  $a$  the amplitude and  $x$  the position perpendicular to the propagation direction. The extracted beam widths at different  $Z$  positions were then fitted to Gaussian beam propagation. Beam waist and Rayleigh length were extracted with  $w_z = w_0 \sqrt{1 + ((z - b) / z_r)^2}$  and  $2z_r = 2\pi w_0^2 / \lambda$ , where  $b$  is the lateral shift,  $z$  the propagation position,  $\lambda$  the wavelength and  $w_0$  the beam waist, respectively. All fits were performed with a nonlinear least-square algorithm implemented in SciPy (Jones et al., 2007).

### 2.4.3 3D Volume Imaging

*Drosophila* embryos endogenously expressing GFP-tagged Neuroglian were raised at 25 °C and prepared according to established protocols. Briefly, embryos were picked at embryonic stages 14-15, dechorionated for 5 min with 50% household bleach, washed with water and placed on a fresh grape juice agar stripe. Single embryos were placed on a cover slip with their anterior or posterior site pointing towards the capillary holder. A mounted 180 µm capillary (TSP180350, Optronis GmbH, Kehl, Germany) with heptane glue was then slowly moved towards the embryo and lifted after a few seconds of drying time. A motorized linear actuator (Z steps of 0.5 µm; Z625B, Thorlabs) controlled the custom-made capillary holder in Z. Camera exposure time was set to 50 ms with 2500 Gain. The power of the 488 nm illumination laser was kept at 130 µW (~130 W/cm<sup>2</sup>). Images were analyzed and visualized with Fiji (ImageJ) and the plugin Volume Viewer.

### 2.4.4 Image Processing - FFT Filtering

Inspired from image correlation spectroscopy (Potvin-Trottier et al., 2013), a Gaussian window filter in the frequency space was employed to simplify the automatic spot detection. The filtering removed the immobile fraction and bleaching kinetics. For this purpose, image stacks were FFT transformed, multiplied with the transmission window  $w(f) = 1 - \exp(-f^2/2f_h^2)$ , where  $f$  is the frequency and  $f_h$  the cut-off frequency ( $f_h = 0.08 \text{ s}^{-1}$ ), and transformed back into real space. First, the FFT filter was benchmarked with tracks obtained from beads with 46 nm diameter (FluoSpheres 660/680, Thermo Scientific) diffusing in water. Settings were chosen to obtain similar raw images as acquired during *Drosophila* imaging (50 ms exposure time, 0 gain, 1x binning, frame shift with 10 MHz read-out speed). All the spots and tracks were then extracted from image sequences with TrackMate (Schindelin et al., 2012). All steps were processed with Python 2.7 and the SciPy packages for optimization, data handling and visualization (Jones et al., 2007).

### 2.4.5 *In Vivo* Single Molecule Experiments

In typical injection experiments, embryos are dechorionated and covered with halocarbon oil to prevent dehydration while supplying sufficient oxygen. To accommodate the use of the illumination objective, the injection protocol (Iordanou et al., 2011) was modified as follows: *pasiflora*<sup>Δ</sup> embryos (Deligiannaki et al., 2015) expressing GFP-tagged Neuroglian were picked at the syncytial blastoderm stage, placed on a double-sided tape and desiccated for 10 minutes. Embryos were covered with halocarbon oil to avoid further desiccation and injected with a solution of 1 µg/µl 10 kDa Dextran-Alexa Fluor 647 (1x PBS, Life Technology). After the injection, the embryos were placed in a dark and humid chamber to incubate for ~20 hours

## 2. Single Molecule Imaging in living *Drosophila* Embryos with Reflected Light-Sheet Microscopy

---

until they had reached embryonic stages 14-15. Embryos were carefully washed with n-Heptane in a collection vial to remove residual halocarbon oil, rinsed 3x with PBTw (PBS, 0.1% Tween 20) buffer, and further processed as described in the 3D volume imaging section. Under wide-field microscopy, the gut morphology served as a marker for the final staging (stage 15 to early 16) right before the experiments were conducted. Normally developed embryos were closely positioned with their anterior-posterior axis parallel to the micro prism without overlapping with each other. All steps of this procedure, except for the imaging, were carried out at 18 °C. The fly strains were obtained from published sources: *pasiflora1<sup>Δ</sup>* (Deligiannaki et al., 2015), *GFP trap Nrg<sup>G00305</sup>* (Morin et al., 2001), *paired-Gal4, UAS-Rab5-GFP* (Bloomington Drosophila Stock Center, BDSC). All strains were raised at 25 °C.

After FFT filtering, single molecule particles were tracked with TrackMate (Schindelin et al., 2012). Data was processed with Python 2.7 and the SciPy packages for optimization, data handling and visualization (Jones et al., 2007). Camera settings were chosen to optimize image quality (50 ms exposure time, 3800 gain, 1x binning, frame shift with 10 MHz read-out speed). The laser intensity was set to 60  $\mu$ W ( $\sim 60$  W/cm<sup>2</sup>) at 488 nm and 1.4 mW ( $\sim 1.4$  kW/cm<sup>2</sup>) at 642 nm. Other single molecule studies used comparable laser power densities (Gebhardt et al., 2013).

### **3 Probing Binding Networks with High-Throughput Thermophoresis**

Reprinted with permission from:

Greiss, F, Kriegel, F, Braun, D. (2017). Probing the Cooperativity of Binding Networks with High-Throughput Thermophoresis. *Analytical Chemistry*, 89(4), 2592–2597, <http://doi.org/10.1021/acs.analchem.6b04861>

Copyright ©2017 American Chemical Society.

#### 3.1 Motivation and Introduction

Systems biology studies the complex networks often depicted as large interconnected graphs with proteins as nodes and their interactions as undirected edges. The topology of graphs is characterized by their degree of interconnections:  $Q = 2m / (n(n - 1))$ , where  $n$  is the number of nodes (proteins) and  $m$  the number of edges (interactions). The biological networks possess a myriad of different degrees of connections; binding hubs or subnetworks. Living cells use the various topologies to compute, respond, and maintain homeostasis.

The entire network of all protein-protein interactions is called the *interactome*. The yeast two-hybrid (Y2H) screen is one of the techniques to get a sense of protein interactions in the cell. Here, the transcription factor GAL4 is separated into its two domains - a DNA-binding domain and a transcription-activation domain. Each domain is covalently fused to one binding partner of interest and when the two proteins interact, the GAL4 domains come close and, together, activate the transcription of a reporter gene. The assay was developed and implemented as a high-throughput biochemical screen in *S. cerevisiae* (Uetz et al., 2000).

In a similar study, researches found that most of the fully connected subnetworks (cliques,  $Q=1$ ) in protein-protein interaction networks have 6-7 proteins. They further found >50 protein clusters that were highly connected - but not fully connected - ( $Q < 1$ ) and contained 4 to 35 protein members (Spirin and Mirny, 2011). One can therefore conclude that nature commonly prefers to form protein complexes and utilize the modularity of protein functions to create biochemical networks. The quantification of networks is an essential component towards understanding their properties.

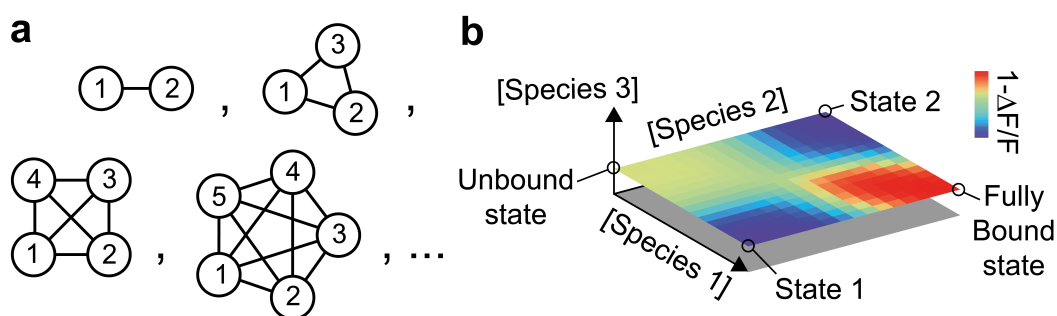


**Figure 3.1** – The complexity of biological binding networks. (a) The analogy of biological networks to graph theory. In the graph, molecular species enter as nodes and their intermolecular interactions as edges. The number of molecular states increases with node number  $n$  as  $(2^n - n)$  in a fully connected network (clique). (b) Sampling the high-dimensional concentration space to investigate complex binding networks. Thermophoresis can be used to generate depletion planes that display thermodynamic information and the transition of a molecule from the unbound state to state 1, state 2, ... and to the fully bound state.

### 3.1.1 Cooperativity and Binding Networks in Nature

Quantifying the effect of cooperativity of homotropic protein binding is an important and well-described field in biochemistry. For historic reasons, the binding of oxygen to hemoglobin is a widely known and thoroughly studied case of a positive homotropic reaction network. Homotropic cooperativity means that oxygen together with other oxygen molecules binds in a mutually supportive manner. Many relevant reaction networks include heterotropic or homotropic binding, both being negative or positive; with weak and strong cooperative effects (Deutman et al., 2009; Tian et al., 2012). The binding of transcription factors (TF) to DNA is for instance often observed to be cooperative between different (heterotropic) or identical (homotropic) TFs in order to support the binding of others (Sayou et al., 2016; Nikolov et al., 1995; Léger et al., 2014).

Interestingly, various regulatory networks in biology have been reported in the literature to contain three different species forming a cooperative heterotrimeric reaction network (Schlessinger et al., 2000; Verstraete et al., 2014; Mantovani, 1999). For example, the CRISPR-based adaptive immunity system of bacteria and archaea was reported to form a heterotrimeric complex (sgRNA-Cas9-dsDNA) as central active unit (Dong et al., 2016). These molecular complexes accumulate modular functions that transcend the capabilities of the isolated parts.

### 3.1.2 Biophysical Instrumentation

Nowadays, the binding of two proteins is commonly probed in high throughput by sophisticated instrumentation to gain a thorough biophysical measure. The methods have given us deep insights into molecular interactions and their contributions to cellular processes. They also enriched our view on the complexity of molecular binding (Sharon et al., 2012; Buenrostro et al., 2014; Nutiu et al., 2011). However, high-throughput assays are still lacking when it comes to the investigation of the formation of protein complexes.

In this study, the development of a novel high-throughput micro-scale thermophoresis (HT-MST) setup is described that is able to measure in addition to simple two species binding, also the formation of molecular complexes in small volumes using 1,536-well plates. Unlike other methods, thermophoretic measurements do not require a size difference between fluorescent ligand and bound protein (Rossi and Taylor, 2011) or the immobilization of biomolecules (Buenrostro et al., 2014; Nutiu et al., 2011). But they give a sensitive measure for a multitude of different molecular properties, a combination of size, effective charge, and the hydration shell (Reichl et al., 2015) that can change upon binding to its partner. The measurements are performed purely optically in bulk fluid and have successfully been applied to a number of challenging experimental conditions (Seidel et al., 2012, 2013; Lippok et al., 2012; Dong et al., 2016), e.g. in cell-free extract and human blood serum.

### 3. Probing Binding Networks with High-Throughput Thermophoresis

---

#### 3.1.3 The Principles of Thermophoresis

Thermophoretic binding measurements employ the movement of molecules along a temperature gradient that is described by the thermal mass flux

$$j_{T,i} = -c_i v_{T,i} = -c_i D_{T,i} \nabla T \quad (3.1)$$

where  $\nabla T$  is the local temperature gradient and  $D_{T,i}$  the thermal diffusion coefficient for species  $i$  with concentration  $c_i$ . In micro-scale thermophoresis experiments, the temperature gradient is generated by local infrared irradiation that is assumed to be propagation-invariant along the observation volume. The diffusion term

$$j_{D,i} = -D_i \nabla c_i \quad (3.2)$$

counteracts the thermal movement. At steady state, the total mass flux is described by  $j_{tot,i} = j_{D,i} + j_{T,i} = 0 = -D_i \nabla c_i - c_i D_{T,i} \nabla T$  and, after integration and with the assumption of temperature-independent  $D_{T,i}$  and  $D_i$ , gives

$$c_{T,i} = c_i \exp(-S_{T,i} \Delta T) \quad (3.3)$$

with the ratio  $S_{T,i} = D_{T,i}/D_i$  termed the *Soret* coefficient. Continuing along the lines given by (Lippok et al., 2012), the linearization for small temperature gradients further leads to  $c_{T,i} = c_i(1 - S_{T,i} \Delta T)$ . Most importantly for the consideration of binding networks, the change in fluorescent signal  $\Delta F$  as experimental readout then permits the quantification of different molecular states because of the linear superposition principle:

$$\Delta F/F = \Delta T \frac{\sum_i c_i f_i S_i}{\sum_i c_i f_i} \quad (3.4)$$

where  $f_i$  is the fluorescence quantum efficiency for molecular state  $i$  and  $S_i$  is the apparent Soret coefficient

$$S_i = \frac{\partial f_i}{f_i \partial T} - S_{T,i} \quad (3.5)$$

that combines the temperature dependence of the fluorescent dye and the thermophoretic depletion. Usually, fluorescence quantum efficiency is assumed to be independent of the molecular state and finally yields

$$\Delta F/F = \Delta T \frac{\sum_i c_i S_i}{\sum_i c_i}. \quad (3.6)$$

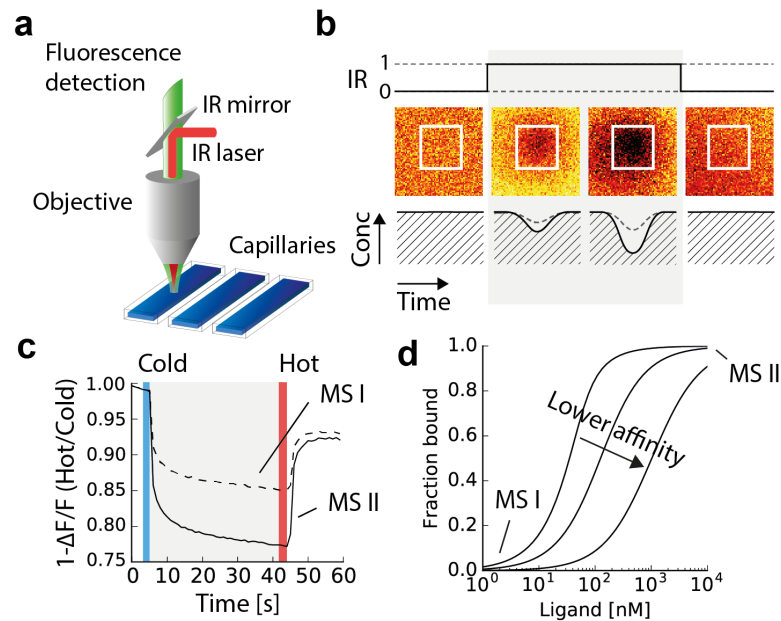


**Figure 3.2** – The course of thermophoretic experiments. (a) The optical schematic to perform thermophoretic measurements as published elsewhere. The illustration is adapted from (Jerabek-Willemsen et al., 2011). (b) The fluorescent signal of the labeled species is acquired over time (averaged from indicated box in images at the top) with local IR heating for each ligand concentration and gives (c) the depletion ( $1 - \Delta F/F$ ) that is used to extract the molecular states (MS). (d) The thermophoretic information can be utilized to measure binding curves between e.g. two molecules. Illustrative binding curves are shown in bottom right graph and calculated with equation 3.9 with a receptor concentration of 50 nM and different  $K_d$ s.

As a consequence, the different states given by  $S_i$  and  $S_j$  with  $i \neq j$  are readily extracted and enable the complete thermodynamic mapping of protein complex formation with more than two molecules. However, since the movement of biomolecules along a temperature gradient is not fully understood, predicting the Soret coefficient for the different molecular states is currently limited and has to be explored experimentally (Reichl et al., 2015, 2014; Maeda et al., 2012; Wolff et al., 2016).

### 3.1.4 Two-State Binding Model

The binding of two molecules (chemicals, proteins, lipids, ...) in a well-stirred environment is described with a two-state model using mass action law



with molecule A and molecule B to bind each other to form AB in a reversible reaction until the equilibrium is reached. The mass action law is the assertion that the rate of chemical reactions

### 3. Probing Binding Networks with High-Throughput Thermophoresis

---

is proportional to the product of the concentration of reactants. For the simple two-state model, we can therefore derive the following equations:

$$\begin{aligned} [\dot{A}] &= [\dot{B}] = -[\dot{AB}] \\ [\dot{A}] &= r_{off} - r_{on} = k_{off}[AB] - k_{on}[A][B] \end{aligned}$$

With the total reaction rate equal zero at steady-state and considering mass conservation,  $[A]_0 = [AB] + [A]$  and  $[B]_0 = [AB] + [B]$ , the analytical equation for the reversible binding of two species can be derived

$$K_d = \frac{k_{off}}{k_{on}} = \frac{[A][B]}{[AB]} = \frac{([A]_0 - [AB])([B]_0 - [AB])}{[AB]} \quad (3.8)$$

where  $[i]$  is the free concentration of species  $i$  at steady-state equilibrium,  $[i]_0$  the initial concentration of species  $i=\{A, B, AB\}$ ,  $k_{on}$  the association rate, and  $k_{off}$  the dissociation rate. Solving equation 3.8, gives the bound fraction  $x$  as

$$x = \frac{[AB]}{[B]_0} = \frac{[A]_0 + [B]_0 + K_d - \sqrt{([A]_0 + [B]_0 + K_d)^2 - 4[A]_0[B]_0}}{2[B]_0} \quad (3.9)$$

The equation is plotted in Fig. 3.2d with A as ligand. Using equation 3.6, we obtain the relation of bound fraction  $x$  with the experimental read-out of the fluorescently labeled species B and AB:

$$\Delta F/F = \Delta T(xS_{AB} + (1-x)S_B) \quad (3.10)$$

At a high concentration of species A ( $[A] \gg [B]$ ), the bound fraction  $x$  approaches 1 and gives the Soret coefficient  $S_{AB}$  of species AB. In contrast, a very low concentration of species A ( $[A] \ll [B]$ ) yields the Soret coefficient  $S_B$  of species B. Inserting equation 3.9 in equation 3.10 yields the final relation

$$\Delta F/F = \Delta T \left( S_B + (S_{AB} - S_B) \frac{[A]_0 + [B]_0 + K_d - \sqrt{([A]_0 + [B]_0 + K_d)^2 - 4[A]_0[B]_0}}{2[B]_0} \right) \quad (3.11)$$

that allows to estimate the dissociation constant  $K_d$  in combination with the measured depletion values for different concentrations of species A and a constant concentration of fluorescently labeled species B (see Fig. 3.2 and Fig. 3.3d). All initial concentrations are known a priori.

## 3.2 Results

### 3.2.1 High-Throughput Thermophoresis Binding Assay

The already well-established technique of micro-scale thermophoresis (MST) was extended to a high throughput assay using standardized 1,536-well plates. To this end, a custom-build optical setup with infrared laser, LEDs for excitation, multiple filter sets and a detection unit (CCD) was supplemented by a motorized 3-axis stage to approach individual microwells (Baaske et al., 2010; Seidel et al., 2014). A detailed description of all parts and protocol steps can be found in the methods section.

An acoustic liquid handler was used to transfer droplets (2.5 nl) into 1,536-well plates and to concurrently generate the optimal dilution series for the evaluation of binding constants. After the volume transfer, the sample solution was centrifuged to coalesce droplets and then manually covered with mineral oil to prevent evaporation. Furthermore, the oil layer maintained a fairly constant boundary during thermophoresis measurements. As published recently, the oil-water interface is known to induce Marangoni convection upon heating. According to

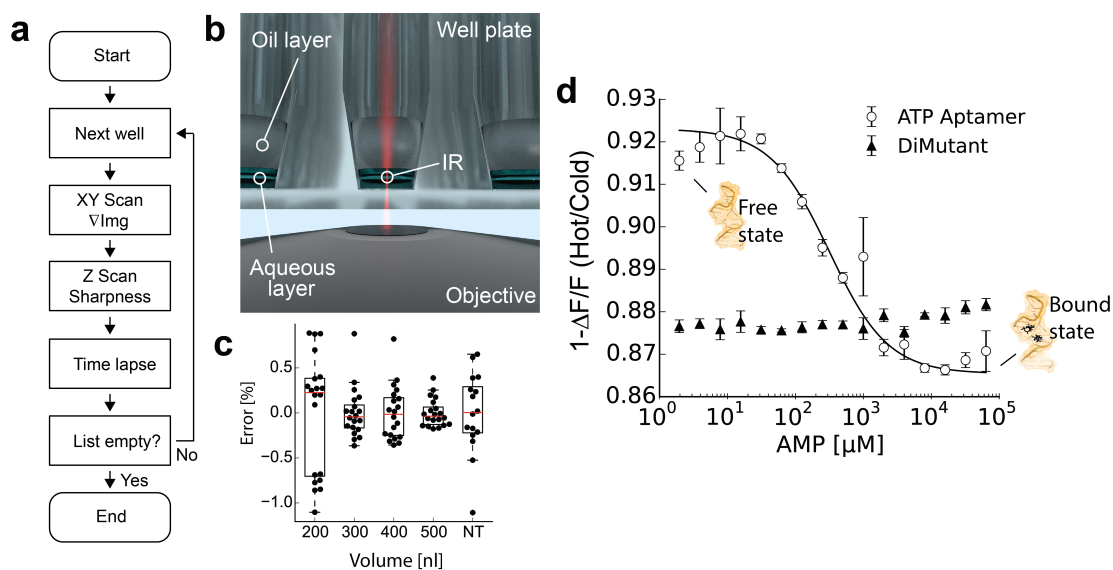


**Figure 3.3** – The automatized workflow of HT-MST and experimental results. (a) Automatized workflow for each well in the 1,536-well plate. X, Y and Z scan minimized the overall measurement error. (b) Sample is covered with mineral oil and imaged from bottom. An infrared laser (IR) induces the local temperature gradient for MST measurements. (c) Total measurement error with different sample volumes compared to the commercial Nanotemper (NT) instrument. A solution of 1  $\mu\text{M}$  DNA-Cy5 dissolved in water was used for benchmarking purposes. (d) The acquired binding curve for the ATP Aptamer to adenosine-5'-monophosphate (AMP) and with the control of a dinucleotide mutant in selection buffer. Error bars represent SD ( $N=3$ ).

### 3. Probing Binding Networks with High-Throughput Thermophoresis

---

numerical simulations, the thermophoretic contribution is however still pronounced and can be extracted with minor compromise (Seidel et al., 2014).

Before actual thermophoretic experiments were started, each well was automatically aligned along the X, Y, and Z direction in order to minimize variations across data points (~1 min for all alignment steps). Notably, the water-oil interface was observed to tilt during centrifugation and subsequently accumulated sample volume asymmetrically. The alignment along the X and Y direction was therefore implemented in a first optimization step to ensure a constant sample layer thickness at the desired region of interest. Using the alignment procedure, the error contribution was minimized. In a second step, the well border was moved into the region of interest and the image sharpness was maximized along the Z direction. The image sharpness was defined as the maximum value of the normed gradient in every fluorescence slice along the acquired Z stack. Both on-the-fly procedures proved to be robust and even helped to overcome minor initial misalignments (Fig. 3.3).

Taken together, the commercial MST setup (Monolith NT.015, Nanotemper GmbH, Germany) with standard treated capillaries and the newly developed HT-MST performed similarly. The error was measured as the depletion deviation from the average for different well positions and capillaries as obtained by HT-MST and the commercial MST setup, respectively. Settings for both benchmarking protocols were chosen to maximize signal-to-noise while minimizing bleaching and to reach comparable depletion values (~0.8). For optimal dilution and depletion reproducibility, a sample volume of 500 nl was used for all following experiments (Fig. 3.3c).

As first realistic performance test, the affinity of an ATP-Aptamer and its dinucleotide mutant to adenosine-5'-monophosphate (AMP) was measured. The *in vitro* design of aptamers provides a powerful way for the production of strongly binding receptors to arbitrary molecules of interest. Experimentally, the ATP aptamer and AMP concentrations were automatically produced with the acoustic liquid handler. A slightly increased dissociation constant was found for the ATP-Aptamer ( $310 \pm 40 \mu\text{M}$  versus  $87 \pm 5 \mu\text{M}$ ) and no detectable binding to its mutant after ~24 h of incubation (Seidel et al., 2014; Baaske et al., 2010). Data were averaged between three different experiments. In summary, the acoustic liquid transfer, the automated dilution series, and thermophoretic measurements were optimized to give robust binding curves (Fig. 3.3d).

#### 3.2.2 Heterotrimeric Binding Networks

Returning to binding networks, a 3-body network is discussed as a consequence of its biological relevance. The heterotrimeric network provides one striking instance that is frequently encountered as structural intermediate and as topological analog in biological systems such as signal transduction and transcription regulation (Schlessinger et al., 2000; Mantovani, 1999;



### 3. Probing Binding Networks with High-Throughput Thermophoresis

---

equal.

$$K_d^{AB} K_d^{AB-C} = K_d^{CB} K_d^{CB-A} = K_d^{AC} K_d^{AC-B} \quad (3.15)$$

This relation holds for all heterotrimeric reaction networks at equilibrium and is readily expanded to more complex reaction networks. Using the Gibbs free energy  $\Delta G_i^\circ = RT \ln K_d^i$ , we finally arrive at our initial statement about path independence:

$$\Delta G_{AB}^\circ + \Delta G_{AB-C}^\circ = \Delta G_{CB}^\circ + \Delta G_{CB-A}^\circ = \Delta G_{AC}^\circ + \Delta G_{AC-B}^\circ \quad (3.16)$$

Experimentally, the heterotrimeric reaction network was implemented using three DNA species that contained an orthogonal set of binding sites. This simplified and artificial test bed allowed to study and establish the theoretical and experimental framework of cooperative heterotrimeric binding.

#### Heterotrimeric DNA Binding Networks

The network consisted of three different DNA species; every individual could bind to the two other species. For this purpose, each DNA species contained two orthogonal binding sites that could bind to the reverse complement of the other species and therefore supported the binding of the third species. In addition, two species featured a hairpin structure in order to increase the depletion resolution between free, intermediate, and fully bound states (Fig. 3.4).

The sequence design of orthogonal binding sites is already well described in literature by the farthest string problem (Garg et al., 2012). It can be dealt employing the Bron-Kerbosch algorithm to find the maximal cliques in undirected graphs. The graph was generated with all possible permutations of an eight base sequence that were only linked if a combination of Hamming distance and common strings exceeded a defined threshold. Then, the Bron-Kerbosch algorithm was employed to find the generated cliques.

Since the procedure is known to be an NP-complete problem (Ouyang et al., 1997), a random subset of the sequence space was sampled, then, the same algorithm was executed several times and the obtained sequences were ranked by information entropy which is computed with  $\sum_l p_l \log_2(p_l)$  where  $p_l$  is the frequency of the base  $l$  in the DNA sequence.

The three species were then assembled together with the different sequences, their reverse complements, a poly(T) bridge between adjacent binding sites and the hairpin structure. As a final step, the three compiled species were cross-checked with NUPACK (Zadeh et al., 2010) for unwanted side reactions (Fig. 3.4).

For the parameter estimation, a 2D titration scheme was developed that superseded the widely known procedure that is commonly being used for the binding of two species. That is keeping

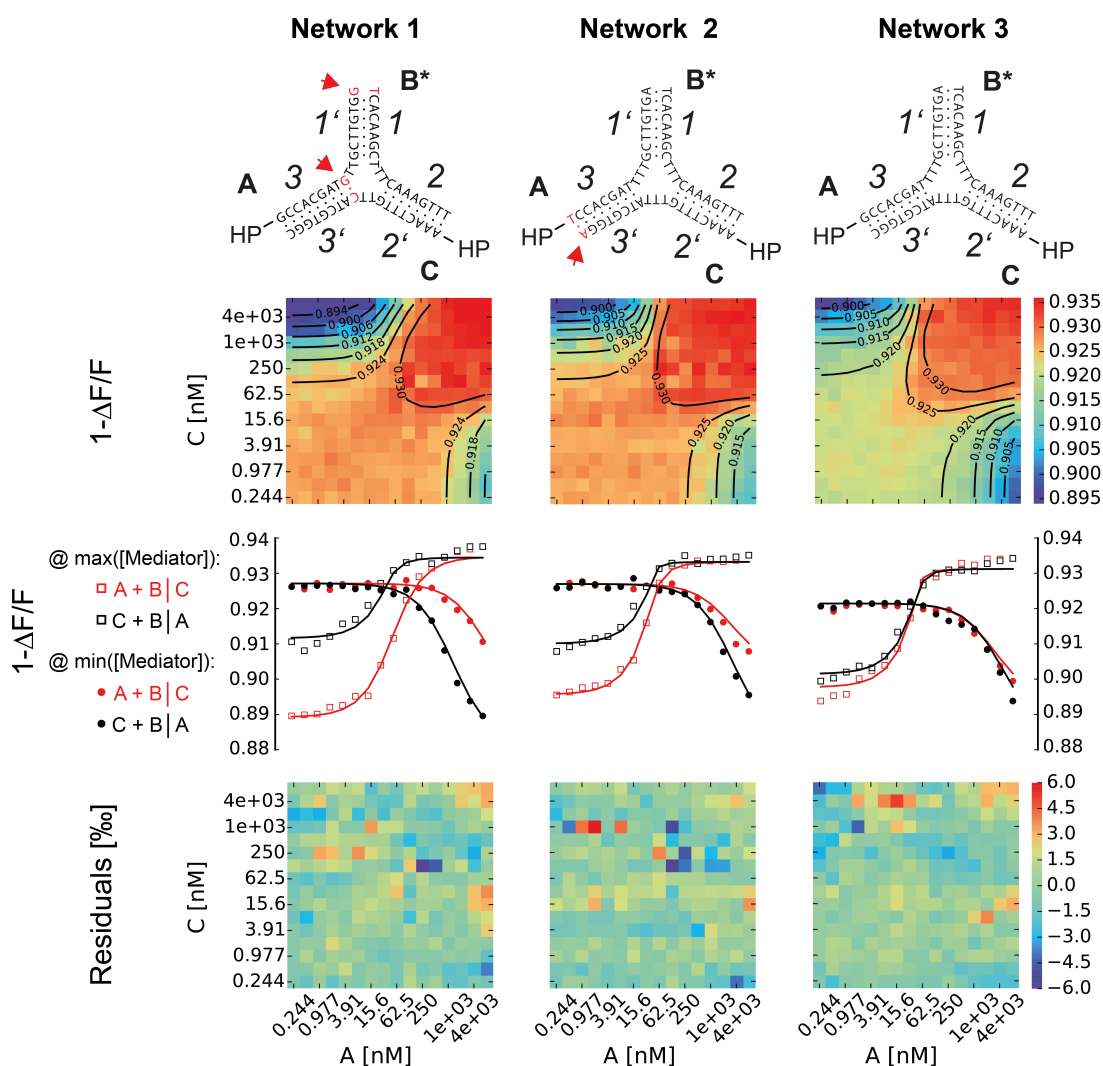


**Figure 3.5** – Experimental HT-MST data for the heterotrimeric DNA binding network. Experimental HT-MST depletion data with superimposed fit (second row, shown as black contour lines) are shown for all three DNA networks with orthogonal single-point mutations (first row, mutations highlighted in red; HP = hair pin). The corresponding parameter and error estimates are given in Table 3.1.

Single binding curves of experimental data (squares, dots) and fits for the heterotrimeric system (lines) taken from 2-dimensional depletion data for minimal and maximal mediator concentration as indicated after the vertical line in the legend (third row). Unlike for low mediator concentration, a standard 2-body binding behavior can in general no longer be assumed for high mediator concentration. Fitting residuals are randomly distributed and demonstrated no systematic error between model and data (fourth row). Every final data set for each network was averaged from three replicates.

one fluorescently labeled species at constant concentration and titrating the non-labeled species. Since the binding of heterotrimeric systems is described by 6 affinity constants and 4

### 3. Probing Binding Networks with High-Throughput Thermophoresis

Soret coefficients, the data sampling was extended from the 1-dimensional to a 2-dimensional space and the number of data points were increased from 16 to 256. More precisely, the fluorescently labeled species was kept constant and the two other non-labeled species were titrated across the predicted binding constants. In this way, an orthogonal and log-spaced 2-dimensional grid in concentration space was generated (see Fig. 3.1b and Fig. 3.5).

The 2-dimensional concentration space was found to be sufficient for parameter estimation, including the spared dimension of the third species could however potentially optimize the parameter estimation even further. For the parameter optimization, the ordinary differential equations for a heterotrimeric binding network are derived according to mass action law and further simplified to compute the association constants  $K_a^i = 1/K_d^i = k_{on}^i/k_{off}^i$  with  $k_{off}^i = 1s^{-1}$ .

$$\begin{aligned}
 \frac{d[A]}{dt} &= -K_a^{AB}[A][B] - K_a^{AC}[C][A] - K_a^{CB-A}[CB][A] + [AB] + [AC] + [ABC] \\
 \frac{d[B]}{dt} &= -K_a^{AB}[A][B] - K_a^{CB}[B][C] - K_a^{AC-B}[AC][B] + [AB] + [CB] + [ABC] \\
 \frac{d[C]}{dt} &= -K_a^{AC}[C][A] - K_a^{CB}[B][C] - K_a^{AB-C}[AB][C] + [AC] + [CB] + [ABC] \\
 \frac{d[AB]}{dt} &= -[AB] - K_a^{AB-C}[AB][C] + K_a^{AB}[A][B] + [ABC] \\
 \frac{d[AC]}{dt} &= -[AC] - K_a^{AC-B}[AC][B] + K_a^{AC}[C][A] + [ABC] \\
 \frac{d[CB]}{dt} &= -[CB] - K_a^{CB-A}[CB][A] + K_a^{CB}[B][C] + [ABC] \\
 \frac{d[ABC]}{dt} &= K_a^{AB-C}[AB][C] + K_a^{AC-B}[AC][B] + K_a^{CB-A}[CB][A] - 3[ABC]
 \end{aligned}$$

The simulations were carried out until the steady state for all species was reached. Since species B was fluorescently labeled in the experiments, the depletion was further computed according to equation 3.6 with

$$\Delta F/F = \frac{S_B[B] + S_{AB}[AB] + S_{CB}[CB] + S_{ABC}[ABC]}{[B]_T} \quad (3.17)$$

where  $[B]_T = [B] + [AB] + [CB] + [ABC]$ .

For the following discussion, the estimated dissociation constants were converted to Gibbs free energy with  $\Delta G_i^\circ = RT \ln K_d^i$ . Here, the thermodynamic relation of equation 3.16 should hold within the limits of the experimental errors (see Table 3.1). Assuming independent binding of two adjacent binding sites of a single DNA species, the sum of Gibbs free energy of the two individual binding sites should further equal that of the combined sites, e.g.  $\Delta G_{AB}^\circ + \Delta G_{AC}^\circ = \Delta G_{CB-A}^\circ$ .

First, the binding of the reference DNA construct was measured without any mismatches

(Table 3.1, Fig. 3.5, Network 3). As expected, the free energy between the single binding site of the dimeric state, and the paired binding site of the trimeric state showed a roughly 2-fold increase for Network 3 and further demonstrated the predicted strong cooperative effect ( $\Delta G_A^\circ$ : -7.5 for the binding of A+B and -8.2 for A+C;  $\Delta G_B^\circ$ : -7.5 for A+B and -7.3 for C+B;  $\Delta G_C^\circ$ : -8.2 for A+C and -7.3 for C+B;  $\Delta G_{CB-A}^\circ$ : -13.7;  $\Delta G_{AC-B}^\circ$ : -12.8;  $\Delta G_{AB-C}^\circ$ : -13.2; all values are given in kcal/mol; see Table 3.1). However, a fairly constant reduced Gibbs free energy between the paired and summed binding sites ( $\Delta G_{CB-A}^\circ - \sum \Delta G_A^\circ = 2.0$ ;  $\Delta G_{AC-B}^\circ - \sum \Delta G_B^\circ = 2.0$ ;  $\Delta G_{AB-C}^\circ - \sum \Delta G_C^\circ = 2.3$ ; all values in kcal/mol) was found to contradict the assumption about independent binding sites. This deviation can be explained by the loss in conformational flexibility of the poly(T) junction through the transition to the heterotrimeric state. Other

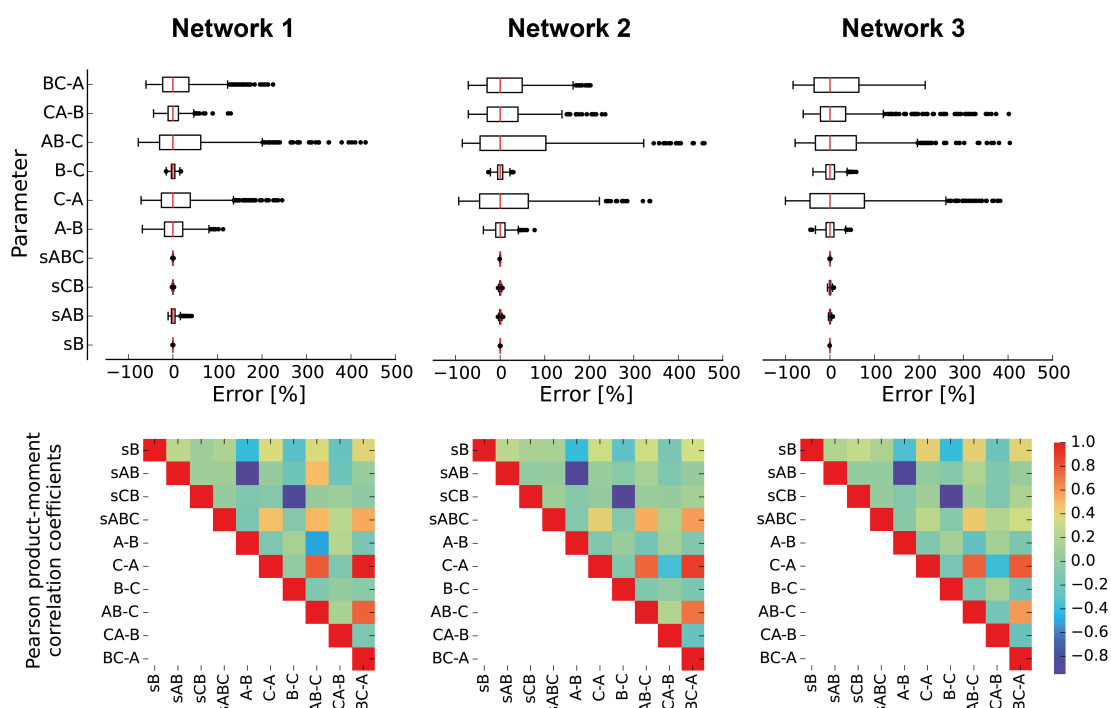


**Figure 3.6** – Error estimation for the three different DNA binding networks and their parameters (upper row) and correlations (lower row). The bootstrap method is graphically depicted in the Supporting Figure B.3. The distributions were found to be skewed for most of the binding affinities (CB-A, AC-B, AB-C, B-C, C-A, A-B) while the different Soret coefficients (sABC, sCB, sAB, sB) demonstrated a symmetric distribution with smaller error. The correlation matrix was estimated linearly according to Pearson's correlation with the experimentally obtained data and the bootstrapped distributions. A fairly strong correlation exists between the non-labeled species AC and the trimeric binding constants. Also, a negative correlation of the Soret coefficients of AB and CB was found that could be explained by the insufficient maximal concentration of titrated ligand (binding plateau at high ligand concentration not reached). The amount of DNA was limited because of secondary low-affinity side-reactions (see Supplementary Fig. B.2).

### 3. Probing Binding Networks with High-Throughput Thermophoresis

studies supportingly showed that bulged DNA three-way junctions could further stabilize the heterotrimeric complex by an extension of the single-stranded region (Lilley, 2000).

By exchanging one single base pair of C:G with one base pair of A:T at the 3 and 3' binding site (Table 3.1, Fig. 3.5, Network 2), the expected reduction in binding affinity between species A and C was measured. This observation confirmed that the proposed titration scheme is able to inclusively resolve the remaining 2-Body binding that is not directly accessible by the fluorescence readout (see Fig. 3.4a, state 3). The found binding constant was verified through the direct labeling of species A and a standard binding curve between species A-Cy5 and C ( $\Delta G_{AC}^{\circ} = -7.6 \pm 0.04$  kcal/mol). Again, the free energy between the two single binding sites and the combined one showed a roughly 2-fold increase in binding energy ( $\Delta G_A^{\circ}$ : -7.5 for A+B and -7.7 for A+C;  $\Delta G_B^{\circ}$ : -7.5 for A+B and -7.5 for C+B;  $\Delta G_C^{\circ}$ : -7.7 for A+C and -7.5 for C+B;  $\Delta G_{CB-A}^{\circ}$ : -12.4;  $\Delta G_{AC-B}^{\circ}$ : -13.0;  $\Delta G_{AB-C}^{\circ}$ : -13.4; all values in kcal/mol; see Table 3.1). The deviation from a simple additive behavior of binding site energies is in the same range as observed for Network 1 and supports the initial conclusion ( $\Delta G_{CB-A}^{\circ} - \sum \Delta G_A^{\circ} = 2.8$ ;  $\Delta G_{AC-B}^{\circ} - \sum \Delta G_B^{\circ} = 2.0$ ;  $\Delta G_{AB-C}^{\circ} - \sum \Delta G_C^{\circ} = 1.8$ ; all values in kcal/mol).

Finally, a base mismatch between species A and B was introduced to further validate the

**Table 3.1** – Binding constants and Gibbs free energies for the three binding networks. The network is composed of six binding steps. The binding of A to B and C to B was further verified with the analytical steady state solution to the reversible binding of two species at low mediator concentration (results are shown in parentheses). The corresponding experimental data is shown in Figure 3.5. Network 3 shows the reference DNA construct without any mismatches. With Network 2, a C:G base pair was exchanged by A:T at binding site 3 and 3'. Hence, the binding affinity of species A to species C was found to reduce (lower  $\Delta G^{\circ}$  in comparison to Network 3). The binding of A to B for Network 1 is diminished compared to Network 2 and 3 through the introduction of a base mismatch at binding site 1 and 1'.

	Network 1		Network 2		Network 3	
	$K_d$ [nM]	$\Delta G^{\circ}$ [kcal/mol]	$K_d$ [nM]	$\Delta G^{\circ}$ [kcal/mol]	$K_d$ [nM]	$\Delta G^{\circ}$ [kcal/mol]
A + B $\rightleftharpoons$ AB	$9710^{+3310}_{-2730}$ (8070 $\pm$ 3100)	$-6.8^{+0.20}_{-0.17}$ (-6.9 $\pm$ 0.23)	$3180^{+540}_{-490}$ (2860 $\pm$ 530)	$-7.5^{+0.10}_{-0.09}$ (-7.6 $\pm$ 0.11)	$3000^{+400}_{-390}$ (2830 $\pm$ 370)	$-7.5^{+0.08}_{-0.08}$ (-7.6 $\pm$ 0.08)
A + C $\rightleftharpoons$ AC	$520^{+350}_{-190}$	$-8.6^{+0.40}_{-0.22}$	$2160^{+2190}_{-1370}$	$-7.7^{+0.60}_{-0.38}$	$970^{+1140}_{-570}$	$-8.2^{+0.70}_{-0.35}$
C + B $\rightleftharpoons$ CB	$1570^{+100}_{-90}$ (1410 $\pm$ 140)	$-7.9^{+0.04}_{-0.03}$ (-8.0 $\pm$ 0.06)	$3270^{+300}_{-280}$ (2720 $\pm$ 370)	$-7.5^{+0.05}_{-0.05}$ (-7.6 $\pm$ 0.08)	$4540^{+690}_{-620}$ (4390 $\pm$ 930)	$-7.3^{+0.09}_{-0.08}$ (-7.3 $\pm$ 0.13)
AB + C $\rightleftharpoons$ ABC	$0.14^{+0.14}_{-0.05}$	$-13.4^{+0.59}_{-0.21}$	$0.14^{+0.22}_{-0.08}$	$-13.4^{+0.93}_{-0.34}$	$0.20^{+0.20}_{-0.09}$	$-13.2^{+0.59}_{-0.27}$
AC + B $\rightleftharpoons$ ABC	$3.60^{+0.60}_{-0.60}$	$-11.5^{+0.10}_{-0.10}$	$0.30^{+0.17}_{-0.12}$	$-13.0^{+0.34}_{-0.24}$	$0.45^{+0.28}_{-0.13}$	$-12.8^{+0.37}_{-0.17}$
CB + A $\rightleftharpoons$ ABC	$2.20^{+1.30}_{-0.70}$	$-11.8^{+0.35}_{-0.19}$	$0.77^{+0.61}_{-0.32}$	$-12.4^{+0.47}_{-0.25}$	$0.09^{+0.08}_{-0.04}$	$-13.7^{+0.53}_{-0.26}$

experimental procedure (Table 3.1, Fig. 3.5, Network 1). In order to keep a uniform total binding energy, a single base pair within the poly(T) bridge was added that neighbors binding site 3 and 3'. The estimated affinity constant increased correspondingly (see Table 3.1). For this third network, the free energy between single and paired binding site proved again roughly a 2-fold increase ( $\Delta G_A^\circ$ : -6.8 for A+B and -8.6 for A+C;  $\Delta G_B^\circ$ : -6.8 for A+B and -7.9 for C+B;  $\Delta G_C^\circ$ : -8.6 for A+C and -7.9 for C+B;  $\Delta G_{CB-A}^\circ$ : -11.8;  $\Delta G_{AC-B}^\circ$ : -11.5;  $\Delta G_{AB-C}^\circ$ : -13.4; all values in kcal/mol; see Table 3.1). In contrast to the first two networks, the shortening of the poly(T) bridge was mirrored by a stronger deviation from the additive free energy behavior ( $\Delta G_{CB-A}^\circ - \sum \Delta G_A^\circ = 3.6$ ;  $\Delta G_{AC-B}^\circ - \sum \Delta G_B^\circ = 3.2$ ;  $\Delta G_{AB-C}^\circ - \sum \Delta G_C^\circ = 3.1$ ; all values in kcal/mol). Again, the increased steric hindrance of the now shortened DNA three-way junction could consistently explain this stronger deviation from the assumed additive free energy relation.

### 3.3 Discussion and Conclusion

An automatized measurement platform was developed to quantitatively investigate binding constants in reduced sample volumes of 500 nl and in high throughput with standardized 1,536-well plates. First, the platform was used to review known concepts and to compare its performance to commercial solutions.

Second, the formation of a heterotrimeric DNA complex with a three-way junction was investigated with an optimized titration scheme and fitting procedure. Base pair variations and mismatches were further screened within the binding sites. According to the error estimates, reliable binding constants can be given on each binding step and thus elucidate the thermodynamic properties of the entire system using a single fluorescence dye. A ~2-fold increase in Gibbs free energy was found for the paired binding sites of each species that is plausible with a homogenous base distribution. Strikingly, a coupling effect between independent binding sites was found that could be explained by the loss in conformational flexibility of the three-way junction in the fully bound state. The energy loss is in the range of ~2 and ~3 kcal/mol for a single-stranded region of three and two bases, respectively.

A limitation to thermophoretic measurements one has to bear in mind, is the necessity for separable Soret coefficients of the free, partially bound, and fully bound species in order to resolve the different molecular states of the interaction network. But, the results as obtained from the heterotrimeric DNA binding networks, should demonstrate how HT-MST is utilized to quantify the thermodynamics of supramolecular complex formation in general. HT-MST eases the way for the thermodynamic investigation of many more assemblies in the near future.

## 3.4 Materials and Methods

### 3.4.1 Assembly of the High-Throughput Thermophoresis Assay

To build a HT-MST instrument, a standard widefield microscope was equipped with a custom-made plate holder, an infrared laser for local heating ( $\lambda=1480$  nm, 500 mW, Fibotec Fiberoptics GmbH, Germany), and three linear stages in a XYZ configuration (xy: M414, Physik Instrumente GmbH, Germany; z: T68-636, Zaber Technologies Inc., Canada) to hold and align the entire optical setup. Optical filters and dichroic mirrors cleaned the emission and excitation (single-color LED light source; M625L2, Thorlabs Inc, USA) path; the infrared laser was coupled into the optical path with a single-mode fiber, aspheric collimator (CFC-C, Thorlabs Inc, USA), and dichroic mirror. The fluorescent signal was collected by an air objective (40x, 0.85 NA, Zeiss), focused by an infinity-corrected tube lens (ITL200, Thorlabs Inc, USA), and imaged onto an interline CCD camera (Stingray F-145B, Allied Vision Technologies GmbH, Germany). Custom-written routines for stage control and thermophoresis experiments were implemented in LabView 2010 (National Instruments). The detailed protocol steps during HT-MST measurements are given in pseudo-code.

**Table 3.2** – *Pseudo-code of high-throughput micro-scale thermophoresis workflow.*

- 1 Let WELLS be the  $n \times 2$  position matrix of  $n$  wells
- 2 Let CONV(image) be the convolution of image with Gaussian 3x3 kernel
- 3 For well in WELLS:
  - 4 Go to well coordinate
  - 5 XY focus = minimize  $\nabla \text{CONV}(\text{image})$  with  $s$  number of XY steps
  - 6 Go to well boarder by user-defined distance
  - 7 Acquire Z stack at equally spaced Z positions
  - 8 Z focus = fit  $\max(\|\nabla \text{CONV}(\text{image})\|)$  over  $Z$  to Gaussian
  - 9 Go to stored XY and Z focus
- 10 Execute MST procedure
- 11 Store raw images
- 12 End

An acoustic liquid handler (Echo 550, Labcyte Inc., USA) was used to generate the dilution series across the wells automatically. The droplet transfer and initial concentrations were given by home-written software in Python 2.7. As a first experimental step, 3 manual dilutions for the ligand had to be prepared because of the finite transfer droplet size with a minimum volume of 2.5 nl and a maximum volume of 500 nl sample volume. The destination 1,536-well plate

(#790801, Greiner Bio-One GmbH, Germany) was centrifuged after a transfer of a maximum of 64 samples for 5 sec at 1,000xg to coalesce and mix droplets. The samples were swiftly covered with 1  $\mu$ l mineral oil (HP50.2, Carl Roth, Germany) and centrifuged for 5 sec at 1,000xg for a second time. The above-mentioned steps were repeated until all concentration samples were transferred. As a final step, the microwell plate was centrifuged for 5 min at 1,000xg. The oil was briefly optimized by screening different kinds (Mineral oil (Carl Roth), Chill-out Liquid Wax (Bio-Rad), Paraffin oil (Carl Roth), Silicon oil (Merck), and Vapor Lock (Qiagen)).

The local temperature gradient was calibrated by first measuring the averaged fluorescence signal of 500 nM DNA-Cy5 as function of base temperature. Then, the solution was kept constant at 28 °C and locally heated with varying infrared irradiation powers. The temperature-dependent initial fluorescence signal drop and the calibration curve for different base temperatures were used to calibrate the gradient. All shown HT-MST experiments were measured with a local temperature gradient of  $\Delta T = 8$  K.

#### 3.4.2 ATP Aptamer

Binding of ATP Aptamer and its mutant to AMP was performed with the HT-MST method as reported in the literature (Baaske et al., 2010). Briefly, Aptamer sequences were ordered from Biomers with HPLC purification (Biomers GmbH, Ulm, Germany) and mixed with a serial dilution of AMP. The dilution series was done automatically with the acoustic liquid handler. The binding curve was fitted to the analytical steady-state solution of a single reversible binding reaction (Lippok et al., 2012) with a non-linear least square routine implemented in the scientific package SciPy (Jones et al., 2007).

#### 3.4.3 Synthetic DNA Binding Network

DNA sequences (see Table 3.3; B: 1 + poly(T) + 2; A: 4' + HP + 4 + 3 + poly(T) + 1'; C: 5 + HP + 5' + 2' + poly(T) + 3') were ordered from Biomers (Biomers GmbH, Ulm, Germany) with HPLC purification. All species were mixed in 500 nl sample volume (137 mM NaCl, 2.7 mM KCl, 12 mM  $\text{HPO}_4^{2-}/\text{H}_2\text{PO}_4^-$ ; 1xPBS) and the fluorescently labeled species was diluted to a final concentration of 50 nM. Samples were generated as explained above. All thermophoretic measurements were performed at 25 °C.

The orthogonal binding sites were designed with Python and the network library NetworkX (Hagberg et al., 2008). A fully connected graph was generated with a random subset of 500 sequences out of all  $4^8$  possible sequences. The edges between nodes (or binding sites) of the complete graph were thresholded according to their mutual Hamming distance and common string. The threshold was defined after empirically optimizing the number of binding sites per

### 3. Probing Binding Networks with High-Throughput Thermophoresis

**Table 3.3** – DNA sequences for the three different DNA reaction networks. The poly(T) bridges are indicated with underlined characters and mutations with uppercase characters. The specific reaction network for each DNA species is given in parentheses.

Name	Sequence (5' to 3')
Bv1 3xT (1, 2, 3)	tcacaagc <u>ttt</u> caaagttt-Cy5
HpAv1 3xT (3)	tagggcatcgcttacaatgccctagccacgatt <u>ttg</u> cttgtga
HpAv1 3xT 3:1bp 1':-1bp (1)	tagggcatcgcttacaatgccctagccacgatG <u>ttg</u> cttgtgG
HpAv1 3xT 3:-1bp (2)	tagggcatcgcttacaatgccctaTccacgatt <u>ttg</u> cttgtga
HpCv1 3xT (3)	gatgtcggcgcttacaccgacatcaaact <u>ttg</u> ttatcgtggc
HpCv1 3xT 3:+1bp (1)	gatgtcggcgcttacaccgacatcaaact <u>ttg</u> tCatcgtggc
HpCv1 3xT 3:C>A (2)	gatgtcggcgcttacaccgacatcaaact <u>ttg</u> ttatcgtggA

clique. Multiple executions of the same algorithm generated a list of cliques that were sorted according to Shannon entropy and lastly evaluated with NUPACK (Zadeh et al., 2010).

#### 3.4.4 Simulation and Optimization of Heterotrimeric Binding Networks

The simulations, optimizations, and visualizations were carried out with the scientific packages implemented in Scipy (Jones et al., 2007). Ordinary differential equations were solved numerically with *odeint* and pre-defined Jacobian matrix to speed up the calculations.

The entire system is defined with six association constants and four Soret coefficients. For optimization, the number of free parameters was further reduced and the value for  $K_a^{AC-B}$  was computed with  $K_a^{AC-B} = (K_a^{CB} K_a^{CB-A} / K_a^{AC} + K_a^{AB} K_a^{AB-C} / K_a^{AC}) / 2$ .

The parameters were log-scaled to further minimize scaling problems and to avoid negative values during fitting. Then, a non-linear gradient-based least square optimization routine using the Levenburg-Marquardt algorithm was employed to optimize the remaining nine parameters (Raue et al., 2013). The median and  $\pm 34\%$  percentile of the bootstrap parameter distributions (N=1000) were used for the parameter estimates and confidence intervals, respectively (Press, 2007).

All 2-Body dissociation constants (see Table 3.1, in brackets) were evaluated at low mediator concentration ( $[\text{mediator}] \approx 0$ ) with a non-linear optimization routine and the analytical steady state solution to the reversible binding of two species (Lippok et al., 2012).

# **A Assorted Project**

## A.1 Numerical Benchmarking of Standing-Wave Multi-Focal Microscopy for Rapid Volume Imaging

### A.1.1 Introduction and Motivation

For the life sciences, today's challenges in fluorescence microscopy lay in the realm of high spatiotemporal resolution. Several approaches were developed using the principles of light-sheet microscopy to reduce the background and, hence, improve the image quality. With these methods at hand, observations in the single eukaryotic cell and on the multi-cellular scale have given us intriguing insights into the stochastic behavior of single molecules to the complex processes of embryogenesis or neurobiology (Chen et al., 2014; Huisken and Stainier, 2009; Keller et al., 2008).

Still, most of the techniques are limited to the imaging of single 2-dimensional planes in the sample volume. The entire volume is only obtained by sequentially scanning the imaging plane across the volume. With this rather slow scanning process, the complex and quick 3-dimensional dynamics of biological processes are difficult to resolve. To this end, studies have demonstrated the successful implementation of simultaneous acquisition of multiple focal planes, either by using  $>1$  detection units that sample equally spaced planes in the observation volume (Ram et al., 2012), or using diffractive optical elements (DOE) (Abrahamsson et al., 2012).

The excitation for these techniques was deployed with an uniform illumination along the Z direction using widefield microscopy. Here, the out-of-focus blur heavily deteriorates the quality of microscopy images. For this purpose, I propose the combination of multi-focal microscopy with a standing-wave excitation pattern. In this study, I first discuss the experimental implementation of standing-wave illumination patterns and the combination with diffractive optical elements on the detection side. The performance of the proposed technique was further evaluated with numerical simulations on single particles and a 3-dimensional sample structure.

### A.1.2 Technology

The detection unit of fluorescence emission is based on the method published by Abrahamsson et al. (Abrahamsson et al., 2012) and describes the elegant realization of a single optical unit to split the different focal planes (3x3) across a 2-dimensional detection unit. Each image gives information from the different focal planes. The main weakness with this method is that the nine field of views need to be distributed across a single camera, but negligible considering the large sensor dimensions of modern scientific CMOS cameras.

The illumination pattern is generated by interference as discussed by Judkewitz et al. (Judke-

## A.1. Numerical Benchmarking of Standing-Wave Multi-Focal Microscopy for Rapid Volume Imaging

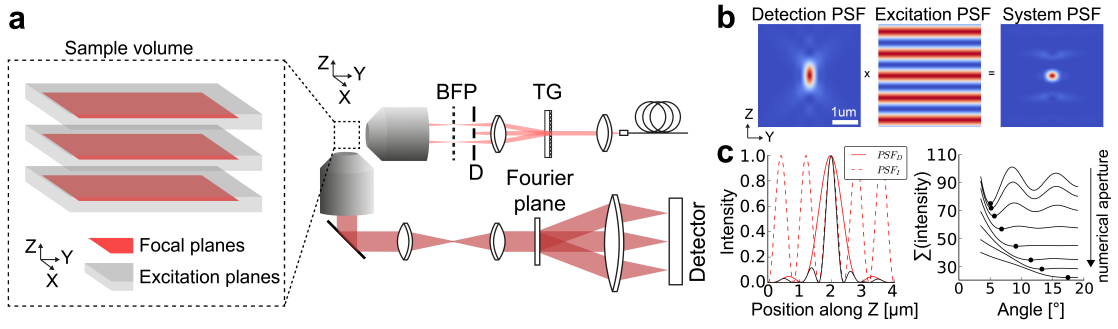


**Figure A.1** – Optical setup with standing-wave illumination and multi-focal detection unit. a) Detection and illumination objectives are orthogonally arranged to align the illumination pattern onto the focal planes. Two laser beams are generated with a transmission grating (TG), the 0-order is rejected by an annular aperture (D), and focused onto the back focal plane (BFP) of the illumination objective to interfere in the sample volume and give rise to the periodic excitation pattern. The fluorescent signal is collected by the detection objective, delayed, and separated by a diffractive optical element that is placed on the Fourier plane. b) The detection PSF is multiplied with the isotropic excitation PSF to compute the final system PSF. The system PSF displays significant side lobes because of the periodic illumination pattern. c) The integrated signal of the system PSF along the Z direction (black line in left graph) is minimized for different detection objectives (highlighted with black dots in right graph) to provide optimal optical sectioning.

witz and Yang, 2014) in the context of axial standing-wave imaging. A DOE is used to split a single laser beam into two, conjugate the two beams onto the back focal plane (BFP) of the objective, and let them interfere in the sample volume (see Fig. A.1a). An alternative approach was reported by Bailey et al. (Bailey et al., 1993) that is based on the idea to generate two beams with opposite propagation directions. However, the method has proven to strongly worsen with refractive index mismatches and sample depth (Bailey et al., 1993; Lanni and Bailey, 1994).

The periodic illumination pattern is defined by its node spacing  $\Delta s = \lambda / (2n \sin(\alpha))$  where  $\alpha$  is the half-angle between the two interfering laser beams after the illumination objective and  $n$  the refractive index of the sample. To find the optimal angle for the two laser beams to interfere, integrated intensity of the system PSF was numerically minimized along the Z direction. An optimal half-angle of  $17^\circ$  ( $NA \approx 0.39$ ) was found between the two illumination beams with a node spacing  $\Delta s \approx 0.79 \mu\text{m}$  for a detection objective with a numerical aperture of 1.2 and an excitation wavelength of 633 nm. Furthermore, an optimal half-angle of  $19^\circ$  ( $NA \approx 0.43$ ;  $\Delta s \approx 0.73 \mu\text{m}$ ) was found for the overall intensity distribution in two dimensions and the same numerical aperture (see Fig. A.1c). Because of the optimal optical sectioning and minor changes between the two modes, an half-angle of  $17^\circ$  was used in this study.

### A.1.3 Numerical Simulations

To verify the technical advantage of standing-wave multi-focal microscopy (SW-MFM), single point emitter were simulated using the isotropic diffraction as described by Richards and Wolf (Gohlke, 2016) and coupled with the various illumination patterns (widefield, standing-wave, and Gaussian profile for light-sheet microscopy). The emission point-spread function (PSF) was computed using an excitation wavelength of 633 nm and an emission wavelength of 700 nm. First, point sources were randomly distributed across a volume to compare the sectioning and background performance for single molecule detection. Second, a sphere was simulated within the detection volume and partially reconstructed using widefield, standing-wave illumination, and light-sheet microscopy.

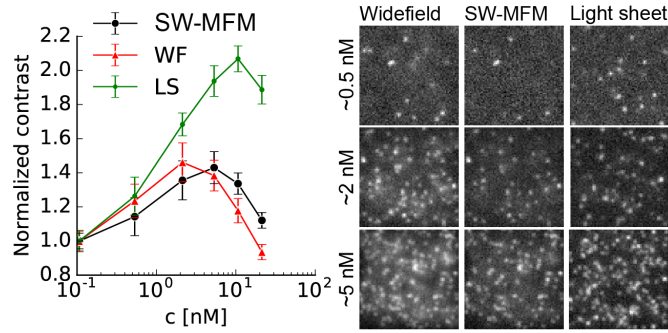


**Figure A.2** – Simulated single particle images for the three different illumination techniques and various particle concentrations. Single particles in volumes were placed randomly with a uniform distribution, a single sample plane at the illumination maximum was extracted, and the particular normalized contrast was computed and averaged. Error bars indicate S.D. from 20 independent simulations.

The single particle simulations were performed with different concentrations and a signal-to-noise ratio (S/N) of 10 for the ratio between emitter amplitude and background noise. Neglecting photon shot noise, only a background-noise limited scenario was simulated with normal distributed random noise (see Fig. A.2) (Thompson et al., 2002). A single plane along the Z position was extracted and the standard deviation of the energy-normalized histograms (Keller, Philipp J et al., 2010) was computed with

$$\sigma = \sqrt{\frac{\sum_i c_i (\frac{i-\bar{I}}{\bar{I}})^2}{1-C}} \quad (\text{A.1})$$

where  $c_i$  is the number of pixels with intensity  $i$ ,  $\bar{I}$  the average intensity of the image,  $C$  the total pixel count, and  $I$  the integrated intensity of the image. The quantity was used to compare the image quality between the different illumination methods. As expected, all techniques

### A.1. Numerical Benchmarking of Standing-Wave Multi-Focal Microscopy for Rapid Volume Imaging

performed similarly well at low particle numbers, but deviated at very high concentrations. SW-MFM performed better than widefield in the intermediate concentration regime, but never exceeded the image quality as found with light-sheet microscopy with a common thickness (FWHM) of  $1\ \mu\text{m}$  for single molecule imaging (Gebhardt et al., 2013; Greiss et al., 2016; Galland et al., 2015).

Here, I conclude that SW-MFM could be advantageous in the intermediate and high concentration regime for temporally demanding experiments. Furthermore, the parallel acquisition of multiple image planes enables to record even complex transportation and diffusion processes in a volume. For instance, while single molecules in a homogeneous environment are well described by uniform Brownian motion, it strongly changes in a local heterogeneous environment (e.g. nucleus) and describes a complex 3-dimensional problem that needs to be recorded in parallel at different positions. In addition, the directed transport of vesicles is again not limited to a single imaging plane and needs to be properly addressed.

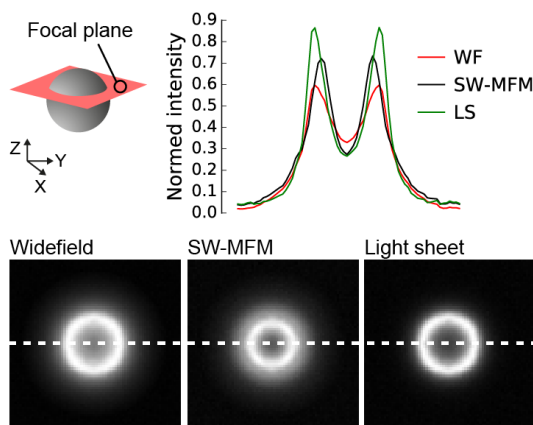


**Figure A.3** – Optical sectioning capabilities of SW-MFM in comparison to widefield and light-sheet microscopy. The shown line profiles are extracted from the image (bottom) and indicated as superimposed dotted white lines. The image plane of interest was chosen to correspond to the respective illumination maxima.

As second test, a sphere was simulated in the form of a giant unilamellar vesicle (GUV), yeast cells or single cells in a 3-dimensional matrix. These geometries are important model systems and well studied in biophysics. To quantify the potential benefits of SW-MFM is therefore essential. Single particle emitters were densely placed on a 3-dimensional sphere using spherical coordinates and transforming it back to the Cartesian system by rounding to the nearest integer position and eliminating  $>1$  point emitter per voxel. Only one emitter per voxel was chosen to obtain a homogeneously distributed “labeling” density. Then, different excitation patterns were used to compare the final image quality at the respective illumination maximum for widefield, SW-MFM, and light-sheet microscopy. The intensity was normalized by the peak intensity in the complete simulated sample volume.

Widefield microscopy performed rather poorly because of the “missing cone” problem (Gustafsson et al., 2008; Agard et al., 1989) that is including out-of-focus blur from other optical sections. Unlike light-sheet microscopy with the minimal background and superior sectioning capabilities, images simulated with SW-MFM demonstrates again intermediate quality. The side lobes of its system PSF deteriorate the quality that is readily seen with the highly demanding structure of a sphere. Nonetheless, the performance of SW-MFM provides the advantage of adequate optical sectioning in comparison to widefield microscopy and, in addition, gives the ability to record multiple focal planes in parallel.

### A.1.4 Conclusions

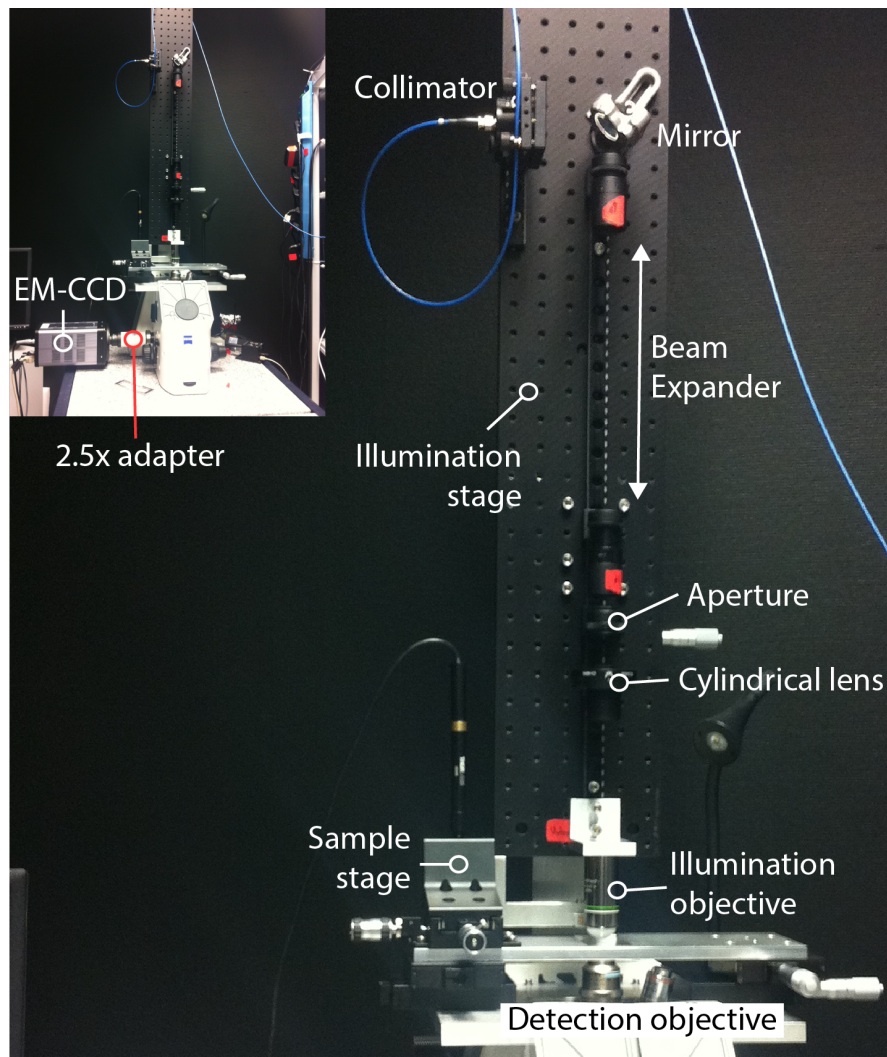
In this study, I sought to numerically approach the advantages of SW-MFM over today’s methods ranging from widefield to the modern implementations of light-sheet microscopy, e.g. lattice light-sheet microscopy (Chen et al., 2014). With the promising combination of rapid volume imaging and the superior optical sectioning over widefield microscopy, SW-MFM provides a valid alternative optical strategy to image fast processes in biology. Light-sheet microscopy gives superior capabilities of optical sectioning, but is limited to the sequential recording of single focal planes. However, the next step should be the experimental realization and testing of real biological samples.

Photo-toxic effects should be equally reduced for SW-MFM as was shown for light-sheet microscopy because of selective excitation and parallel acquisition (Stelzer, 2014).

With SW-MFM, potential applications would certainly be low light scenarios that are very common in biology due to the limited quantum yield of biological fluorescent probes or photo-toxic artifacts with intense exposures. While the periodic illumination pattern of SW-MFM introduces minor out-of-focus information, the signal could be further useful for potential post-processing of raw data to gain an improved reconstructed image.

## **B Supporting Material**

## B.1 Single Molecule Imaging in living *Drosophila* Embryos with Reflected Light-Sheet Microscopy



**Figure B.1** – Implementation of the reflected light-sheet microscope. An inverted microscope body was used as the central building block for the sample and illumination stage. The illumination stage was built on top of the rear's microscope stage. A XYZ motor enabled to translate the illumination unit to align the light sheet with the detection unit. The sample stage was custom-designed and supplemented with a linear motor along the Z direction. The sample was translated using a capillary. Further details can be found in the Materials and Methods section.

## B.2 Probing Binding Networks with High-Throughput Thermophoresis

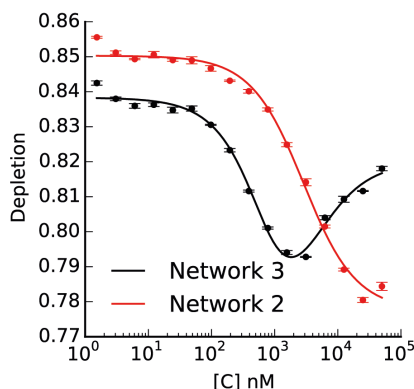


**Figure B.2** – Supplementing binding curves as found by titrating species A-Cy5 (instead of labeled species B) with species C. The fluorophore was attached at the 3'-end of A to minimize interference with the binding site (see Fig. 3.4b). The binding curves were measured in 1xPBS buffer at 26 °C using the commercial Monolith NT.015 (Nanotemper GmbH, Germany) and standard treated capillaries. The binding of species A-Cy5 and species C of Network 3 displayed a second low-affinity binding (with independent binding assumed:  $K_{d,AC} = 340 \pm 160$  nM and  $K_{d,AC} = 2880 \pm 1380$  nM). The obtained binding constant from the heterotrimeric titration scheme agrees considerably ( $K_{d,AC} = 970^{+1140}_{-570}$  nM). Also, the binding affinity between A-Cy5 and C of Network 2 ( $K_{d,AC} = 2610 \pm 180$  nM) agrees well with the binding constants as obtained by the proposed heterotrimeric titration scheme and fitting procedure ( $K_{d,AC} = 2160^{+2190}_{-1370}$  nM).

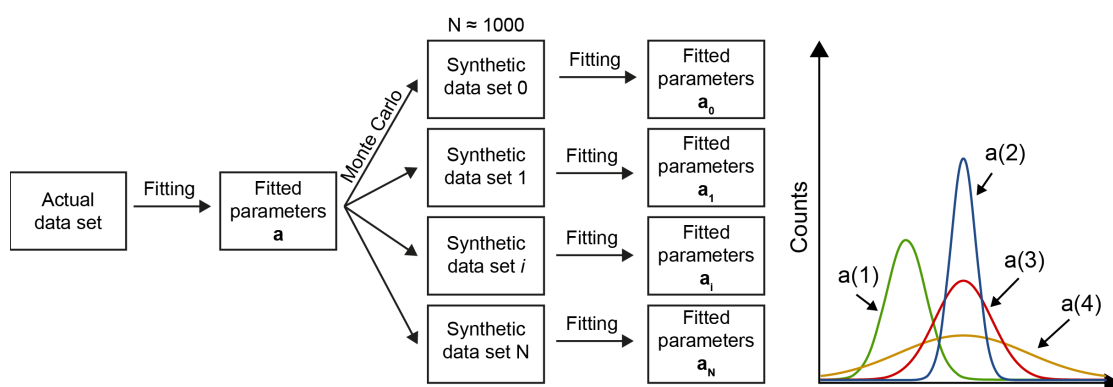


**Figure B.3** – The principle of bootstrapping confidence intervals. The graphical representation was adapted from (Press, 2007). First, parameters are fitted using the original data set. Then, the standard deviation between fitted and original data set is used as scaling factor for randomly generated values with a normal distribution (=synthetic errors). The synthetic errors are added to the original data set and used for fitting. The process is repeated to sample the entire parameter distributions. The median and  $\pm 34\%$  percentile of the parameter distributions were used for the parameter estimates and confidence intervals, respectively.

## Appendix B. Supporting Material

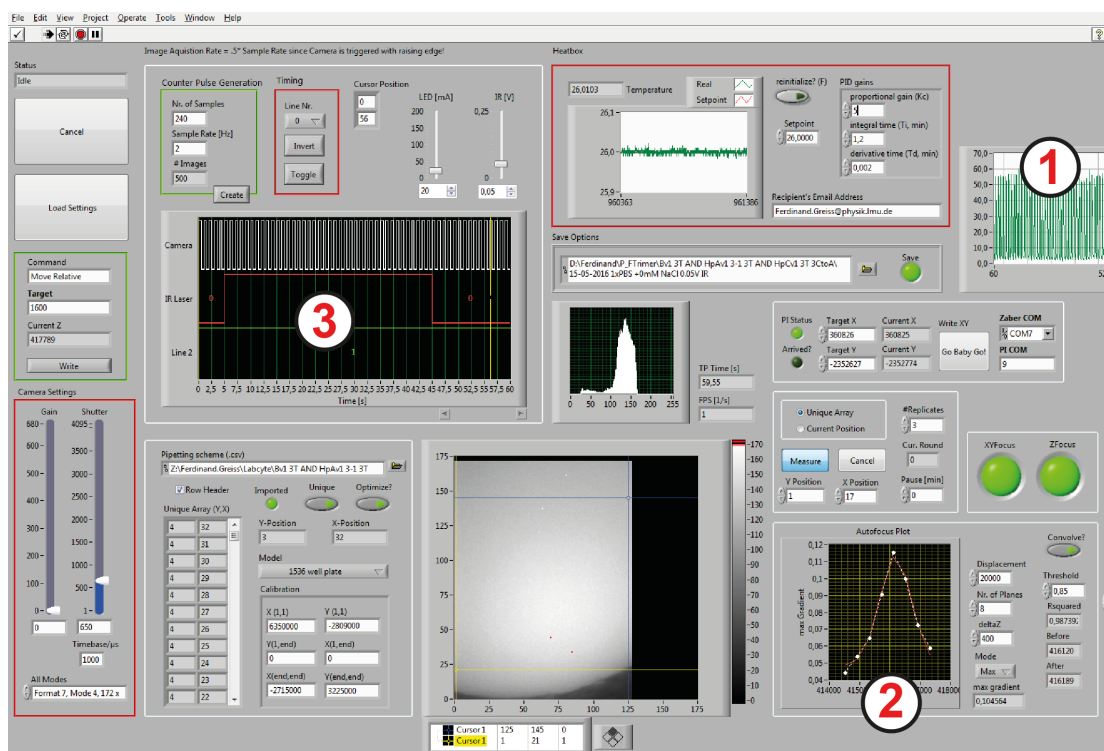


**Figure B.4** – The HT-MST graphical user interface and logic was implemented in LabView 2010 (National Instruments). A list of well coordinates (unique array) is processed according to the following protocol:

- ① Optimize XY position by moving along the image gradient to get a uniform fluorescent intensity.
- ② Optimize Z position by maximizing the image sharpness (maximal normed gradient) along the Z direction and obtain maximal image sharpness over Z by fitting a Gaussian function.
- ③ Trigger the camera acquisition with constant LED signal and temporary local heating by infrared irradiation.

A PID system controls the sample temperature through a heating foil that is attached to the custom-made plate chamber.

## B.2. Probing Binding Networks with High-Throughput Thermophoresis

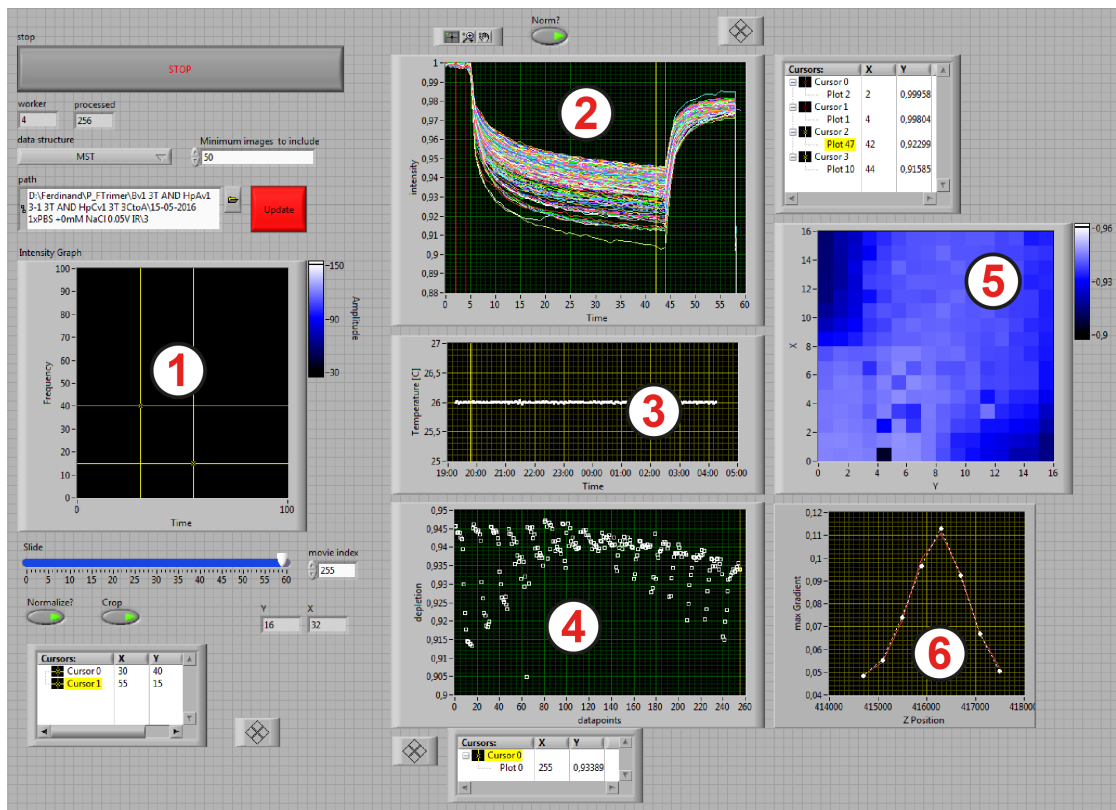


**Figure B.5** – The downstream analysis of HT-MST data was implemented in LabView 2010 (National Instruments).

① Image sequences for each well in the 1,536 well plate with time slider. ② Fluorescence time traces as averaged from rectangular region that is adjusted by the cursers in ①. ③ Tracked temperature over time in sample volume. ④ Depletion values averaged from regions controlled by the cursers in ② for each time trace. ⑤ Reshaped depletion value to show the actual positions in well plate. ⑥ Z optimization with raw (white dots) and fitted (red line) values.



# Acknowledgements

**Dieter:** Vielen Dank für Alles! Bei einer ruhigen Tasse Cappuccino, kamen öfters gute Ideen in stressigen Zeiten. In deinem Labor konnte ich viele Dinge lernen. Vor allem hast du mir beigebracht, wie eigene Ideen zu realisieren sind.

**Myrto:** I cherish your scientific talent and expertise. You helped me a lot learning a reasonable amount about fruit flies.

**Fruit flies:** Sorry for poking you once in a while. I always tried to be gentle and make you survive the experiments. I owe you a bucket of fruits!

**Monika:** Danke für die sorgsame Betreuung meiner Selbst und meiner Fruchtfliegen.

**Peter:** Vielen Dank! Ohne deinen Ideenreichtung wären einige Teile meiner Arbeit sehr schwer gewesen.

**Claudia:** Danke für die sympathische Betreuung und super Lerneinheiten.

**Ulrike:** Danke für die Zeit in deinem Labor.

**QBM:** QBM retreats are obviously the best! Thank you for the financial support, the opportunity to travel to distant places, and taking part in amazing conferences (Biophysical Society) and summer schools (CSHL).

**Braun Leute:** I am thankful to all you guys (special thanks goes to Soichi, Franzi, Maren, Georg, Manu, and Zhenya). Vielen Dank für alle passenden und besonders unpassenden Lebensratschlägen!

**Johanna:** Auf ein Leben mir dir!

*Wenn Du ein Schiff bauen willst, so trommle nicht Männer zusammen, um Holz zu beschaffen, Werkzeuge vorzubereiten, sondern lehre die Männer die Sehnsucht nach dem weiten, endlosen Meer!*

– Antoine de Saint-Exupéry



# Bibliography

- Abrahamsson, S., Chen, J., Hajj, B., Stallinga, S., Katsov, A. Y., Wisniewski, J., Mizuguchi, G., Soule, P., Mueller, F., Darzacq, C. D., Darzacq, X., Wu, C., Bargmann, C. I., Agard, D. A., Dahan, M., and Gustafsson, M. G. L. (2012). Fast multicolor 3D imaging using aberration-corrected multifocus microscopy. *Nature Methods*, 10(1):60–63.
- Agard, D. A., Hiraoka, Y., Shaw, P., and Sedat, J. W. (1989). Chapter 13 Fluorescence Microscopy in Three Dimensions. In *Fluorescence Microscopy of Living Cells in Culture Part B. Quantitative Fluorescence Microscopy—Imaging and Spectroscopy*, pages 353–377. Elsevier.
- Baaske, P., Wienken, C. J., Reineck, P., Duhr, S., and Braun, D. (2010). Optical Thermophoresis for Quantifying the Buffer Dependence of Aptamer Binding. *Angewandte Chemie International Edition*, 49(12):2238–2241.
- Bailey, B., Farkas, D. L., Taylor, D. L., and Lanni, F. (1993). Enhancement of axial resolution in fluorescence microscopy by standing-wave excitation. *Nature*, 366(6450):44–48.
- Buenrostro, J. D., Araya, C. L., Chircus, L. M., Layton, C. J., Chang, H. Y., Snyder, M. P., and Greenleaf, W. J. (2014). Quantitative analysis of RNA-protein interactions on a massively parallel array reveals biophysical and evolutionary landscapes. *Nature Biotechnology*, 32(6):562–568.
- Chen, B. C., Legant, W. R., Wang, K., and Shao, L. (2014). Lattice light-sheet microscopy: Imaging molecules to embryos at high spatiotemporal resolution. *Science*.
- Crank, J. (1975). *The mathematics of diffusion, 2nd Edn.* Clarendon Press, Oxford.
- Deligiannaki, M., Casper, A. L., Jung, C., and Gaul, U. (2015). Pasiflora proteins are novel core components of the septate junction. *Development*, 142(17):3046–3057.
- Deutman, A. B. C., Monnereau, C., Moalin, M., Coumans, R. G. E., Veling, N., Coenen, M., Smits, J. M. M., de Gelder, R., Elemans, J. A. A. W., Ercolani, G., Nolte, R. J. M., and Rowan, A. E. (2009). Squaring cooperative binding circles. *Proceedings of the National Academy of Sciences*, 106(26):10471–10476.

## Bibliography

---

- Dong, D., Ren, K., Qiu, X., Zheng, J., Guo, M., Guan, X., Liu, H., Li, N., Zhang, B., Yang, D., Ma, C., Wang, S., Wu, D., Ma, Y., Fan, S., Wang, J., Gao, N., and Huang, Z. (2016). The crystal structure of Cpf1 in complex with CRISPR RNA. *Nature*, 532(7600):522–526.
- Elowitz, M. and Lim, W. A. (2010). Build life to understand it. *Nature*.
- Fabrowski, P., Necakov, A. S., Mumbauer, S., Loeser, E., Reversi, A., Streichan, S., Briggs, J. A. G., and De Renzis, S. (2013). Tubular endocytosis drives remodelling of the apical surface during epithelial morphogenesis in *Drosophila*. *Nature Communications*, 4:1–12.
- Friedrich, M., Nozadze, R., Gan, Q., Zelman-Femiak, M., Ermolayev, V., Wagner, T. U., and Harms, G. S. (2009). Detection of single quantum dots in model organisms with sheet illumination microscopy. *Biochemical and Biophysical Research Communications*, 390(3):722–727.
- Galland, R., Greci, G., Aravind, A., Viasnoff, V., Studer, V., and Sibarita, J.-B. (2015). 3D high- and super-resolution imaging using single-objective SPIM. *Nature Methods*, 12(7):641–644.
- Garg, A., Lohmueller, J. J., Silver, P. A., and Armel, T. Z. (2012). Engineering synthetic TAL effectors with orthogonal target sites. *Nucleic Acids Research*, 40(15):7584–7595.
- Gebhardt, J. C. M., Suter, D. M., Roy, R., Zhao, Z. W., Chapman, A. R., Basu, S., Maniatis, T., and Xie, X. S. (2013). Single-molecule imaging of transcription factor binding to DNA in live mammalian cells. *Nature Methods*, 10(5):421–426.
- Genova, J. L. (2003). Neuroglian, Gliotactin, and the Na<sup>+</sup>/K<sup>+</sup> ATPase are essential for septate junction function in *Drosophila*. *The Journal of Cell Biology*, 161(5):979–989.
- Gohlke, C. (2016). Point spread function calculations for fluorescence microscopy. <http://www.lfd.uci.edu/gohlke/>.
- Greiss, F., Deligiannaki, M., Jung, C., Gaul, U., and Braun, D. (2016). Single-Molecule Imaging in Living *Drosophila* Embryos with Reflected Light-Sheet Microscopy. *Biophysical Journal*, 110(4):939–946.
- Gustafsson, M., Shao, L., Carlton, P. M., and Wang, C. (2008). Three-dimensional resolution doubling in wide-field fluorescence microscopy by structured illumination. *Biophysical Journal*.
- Hagberg, A. A., Schult, D. A., and Swart, P. J. (2008). Exploring Network Structure, Dynamics, and Function using NetworkX. In el Varoquaux, G., Vaught, T., and Millman, J., editors, *Proceedings of the 7th Python in Science Conference*, pages 11–15, Pasadena, CA USA.
- Huisken, J. (2004). Optical Sectioning Deep Inside Live Embryos by Selective Plane Illumination Microscopy. *Science*, 305(5686):1007–1009.

- Huisken, J. and Stainier, D. Y. R. (2009). Selective plane illumination microscopy techniques in developmental biology. *Development*, 136(12):1963–1975.
- Iordanou, E., Chandran, R. R., Blackstone, N., and Jiang, L. (2011). RNAi Interference by dsRNA Injection into *Drosophila* Embryos. *Journal of Visualized Experiments*, (50):1–4.
- Izeddin, I., Récamier, V., Bosanac, L., Cissé, I. I., Boudarene, L., Dugast-Darzacq, C., Proux, F., Bénichou, O., Voituriez, R., Bensaude, O., Dahan, M., and Darzacq, X. (2014). Author response. *eLife*, 3:23352–27.
- Jerabek-Willemsen, M., Wienken, C. J., Braun, D., Baaske, P., and Duhr, S. (2011). Molecular Interaction Studies Using Microscale Thermophoresis. *ASSAY and Drug Development Technologies*, 9(4):342–353.
- Jones, E., Oliphant, T., and Peterson, P. (2007). SciPy: Open source scientific tools for Python.
- Judkewitz, B. and Yang, C. (2014). Axial standing-wave illumination frequency-domain imaging (SWIF). *Optics Express*, 22(9):11001–11010.
- Keller, P. J., Schmidt, A. D., Wittbrodt, J., and Stelzer, E. H. K. (2008). Reconstruction of Zebrafish Early Embryonic Development by Scanned Light Sheet Microscopy. *Science*, 322(5904):1065–1069.
- Keller, Philipp J, Schmidt, Annette D, Santella, Anthony, Khairy, Khaled, Bao, Zhirong, Wittbrodt, Joachim, and Stelzer, Ernst H K (2010). Fast, high-contrast imaging of animal development with scanned light sheet-based structured-illumination microscopy. *Nature Methods*, 7(8):637–642.
- Kicheva, A., Pantazis, P., Bollenbach, T., Kalaidzidis, Y., Bittig, T., Jülicher, F., and González-Gaitán, M. (2007). Kinetics of Morphogen Gradient Formation. *Science*, 315(5811):521–525.
- Kues, T., Dickmanns, A., Lührmann, R., Peters, R., and Kubitscheck, U. (2001). High intranuclear mobility and dynamic clustering of the splicing factor U1 snRNP observed by single particle tracking. *Proceedings of the National Academy of Sciences*, 98(21):12021–12026.
- Lanni, F. and Bailey, B. (1994). Standing-wave excitation for fluorescence microscopy. *Trends in Cell Biology*, 4(7):262–265.
- Léger, H., Smet-Nocca, C., Attmane-Elakeb, A., Morley-Fletcher, S., Benecke, A. G., and Eilebrecht, S. (2014). A TDG/CBP/RAR $\alpha$  Ternary Complex Mediates the Retinoic Acid-dependent Expression of DNA Methylation-sensitive Genes. *Genomics, Proteomics & Bioinformatics*, 12(1):8–18.
- Li, G.-W. and Xie, X. S. (2011). Central dogma at the single-molecule level in living cells. *Nature*, 475(7356):308–315.

## Bibliography

---

- Lilley, D. M. J. (2000). Structures of helical junctions in nucleic acids. *Quarterly Reviews of Biophysics*, 33(2):109–159.
- Lippok, S., Seidel, S. A. I., Duhr, S., Uhland, K., Holthoff, H.-P., Jenne, D., and Braun, D. (2012). Direct Detection of Antibody Concentration and Affinity in Human Serum Using Microscale Thermophoresis. *Analytical Chemistry*, 84(8):3523–3530.
- Maeda, Y. T., Tlustý, T., and Libchaber, A. (2012). Effects of long DNA folding and small RNA stem-loop in thermophoresis. *Proceedings of the National Academy of Sciences*, 109(44):17972–17977.
- Mantovani, R. (1999). The molecular biology of the CCAAT-binding factor NF-Y. *Gene*, 239(1):15–27.
- Metzler, R. and Klafter, J. (2000). The random walk's guide to anomalous diffusion: a fractional dynamics approach. *Physics Reports*, 339(1):1–77.
- Morin, X., Daneman, R., Zavortink, M., and Chia, W. (2001). A protein trap strategy to detect GFP-tagged proteins expressed from their endogenous loci in *Drosophila*. *Proceedings of the National Academy of Sciences*, 98(26):15050–15055.
- Nikolov, D. B., Chen, H., Halay, E. D., Usheva, A. A., Hisatake, K., Lee, D. K., Roeder, R. G., and Burley, S. K. (1995). Crystal structure of a TFIIB–TBP–TATA-element ternary complex. *Nature*, 377(6545):119–128.
- Nutiu, R., Friedman, R. C., Luo, S., Khrebtukova, I., Silva, D., Li, R., Zhang, L., Schroth, G. P., and Burge, C. B. (2011). Direct measurement of DNA affinity landscapes on a high-throughput sequencing instrument. *Nature Biotechnology*, 29(7):659–664.
- Ouyang, Q., Kaplan, P. D., Liu, S., and Libchaber, A. (1997). DNA Solution of the Maximal Clique Problem. *Science*, 278(5337):446–449.
- Pampaloni, F., Chang, B.-J., and Stelzer, E. H. K. (2015). Light sheet-based fluorescence microscopy (LSFM) for the quantitative imaging of cells and tissues. *Cell and Tissue Research*, 360(1):129–141.
- Pluen, A., Netti, P. A., Jain, R. K., and Berk, D. A. (1999). Diffusion of Macromolecules in Agarose Gels: Comparison of Linear and Globular Configurations. *Biophysical Journal*, 77(1):542–552.
- Potvin-Trottier, L., Chen, L., Horwitz, A. R., and Wiseman, P. W. (2013). A nu-space for image correlation spectroscopy: characterization and application to measure protein transport in live cells. *New Journal of Physics*, 15(8):085006–21.

- Press, W. H. (2007). *Numerical Recipes 3rd Edition*. The Art of Scientific Computing. Cambridge University Press.
- Ram, S., Kim, D., Ober, R. J., and Ward, E. S. (2012). 3D Single Molecule Tracking with Multifocal Plane Microscopy Reveals Rapid Intercellular Transferrin Transport at Epithelial Cell Barriers. *Biophysical Journal*, 103(7):1594–1603.
- Raue, A., Schilling, M., Bachmann, J., Matteson, A., Schelke, M., Kaschek, D., Hug, S., Kreutz, C., Harms, B. D., Theis, F. J., Klingmüller, U., and Timmer, J. (2013). Lessons Learned from Quantitative Dynamical Modeling in Systems Biology. *PLoS ONE*, 8(9):e74335.
- Reichl, M., Herzog, M., Götz, A., and Braun, D. (2014). Why Charged Molecules Move Across a Temperature Gradient: The Role of Electric Fields. *Physical Review Letters*, 112(19):198101.
- Reichl, M., Herzog, M., Greiss, F., Wolff, M., and Braun, D. (2015). Understanding the similarity in thermophoresis between single- and double-stranded DNA or RNA. *Physical Review E*, 91(6):062709.
- Reverey, J. F., Jeon, J.-H., Bao, H., Leippe, M., Metzler, R., and Selhuber-Unkel, C. (2015). Superdiffusion dominates intracellular particle motion in the supercrowded cytoplasm of pathogenic *Acanthamoeba castellanii*. *Scientific Reports*, pages 1–14.
- Ritter, J. (2011). *Single molecule tracking with light sheet microscopy*. PhD thesis, Mathematisch-Naturwissenschaftliche Fakultät, Universität Bonn.
- Ritter, J. G., Veith, R., Veenendaal, A., Siebrasse, J. P., and Kubitscheck, U. (2010). Light Sheet Microscopy for Single Molecule Tracking in Living Tissue. *PLoS ONE*, 5(7):e11639–9.
- Rossi, A. M. and Taylor, C. W. (2011). Analysis of protein-ligand interactions by fluorescence polarization. *Nature Protocols*, 6(3):365–387.
- Sanamrad, A., Persson, F., Lundius, E. G., Fange, D., Gynnå, A. H., and Elf, J. (2014). Single-particle tracking reveals that free ribosomal subunits are not excluded from the *Escherichia coli* nucleoid. *Proceedings of the National Academy of Sciences*, 111(31):11413–11418.
- Sandison, D. R. and Webb, W. W. (1994). Background rejection and signal-to-noise optimization in confocal and alternative fluorescence microscopes. *Applied Optics*, 33(4):603–615.
- Sayou, C., Nanao, M. H., Jamin, M., Posé, D., Thévenon, E., Grégoire, L., Tichtinsky, G., Denay, G., Ott, F., Peirats Llobet, M., Schmid, M., Dumas, R., and Parcy, F. (2016). A SAM oligomerization domain shapes the genomic binding landscape of the LEAFY transcription factor. *Nature Communications*, 7:11222.

## Bibliography

---

- Schindelin, J., Arganda-Carreras, I., Frise, E., Kaynig, V., Longair, M., Pietzsch, T., Preibisch, S., Rueden, C., Saalfeld, S., Schmid, B., Tinevez, J.-Y., White, D. J., Hartenstein, V., Eliceiri, K., Tomancak, P., and Cardona, A. (2012). Fiji: an open-source platform for biological-image analysis. *Nature Methods*, 9(7):676–682.
- Schlessinger, J., Plotnikov, A. N., Ibrahimi, O. A., Eliseenkova, A. V., Yeh, B. K., Yayon, A., Linhardt, R. J., and Mohammadi, M. (2000). Crystal Structure of a Ternary FGF-FGFR-Heparin Complex Reveals a Dual Role for Heparin in FGFR Binding and Dimerization. *Molecular Cell*, 6(3):743–750.
- Schütz, G. J., Schindler, H., and Schmidt, T. (1997). Single-molecule microscopy on model membranes reveals anomalous diffusion. *Biophysical Journal*, 73:1073–1080.
- Seidel, S. A. I., Dijkman, P. M., Lea, W. A., van den Bogaart, G., Jerabek-Willemsen, M., Lasic, A., Joseph, J. S., Srinivasan, P., Baaske, P., Simeonov, A., Katritch, I., Melo, F. A., Ladbury, J. E., Schreiber, G., Watts, A., Braun, D., and Duhr, S. (2013). Microscale thermophoresis quantifies biomolecular interactions under previously challenging conditions. *Methods*, 59(3):301–315.
- Seidel, S. A. I., Markwardt, N. A., Lanzmich, S. A., and Braun, D. (2014). Thermophoresis in Nanoliter Droplets to Quantify Aptamer Binding. *Angewandte Chemie International Edition*, 53(30):7948–7951.
- Seidel, S. A. I., Wienken, C. J., Geissler, S., Jerabek-Willemsen, M., Duhr, S., Reiter, A., Trauner, D., Braun, D., and Baaske, P. (2012). Label-Free Microscale Thermophoresis Discriminates Sites and Affinity of Protein-Ligand Binding. *Angewandte Chemie International Edition*, 51(42):10656–10659.
- Sharon, E., Kalma, Y., Sharp, A., Raveh-Sadka, T., Levo, M., Zeevi, D., Keren, L., Yakhini, Z., Weinberger, A., and Segal, E. (2012). Inferring gene regulatory logic from high-throughput measurements of thousands of systematically designed promoters. *Nature Biotechnology*, 30(6):521–530.
- Spirin, V. and Mirny, L. A. (2011). Protein complexes and functional modules in molecular networks. *Proceedings of the National Academy of Sciences*, 100(21):12123–12128.
- Stelzer, E. H. K. (2014). Light-sheet fluorescence microscopy for quantitative biology. *Nature Methods*, 12(1):23–26.
- Thompson, R. E., Larson, D. R., and Webb, W. W. (2002). Precise nanometer localization analysis for individual fluorescent probes. *Biophysical Journal*, 82(5):2775–2783.
- Tian, F., Jiao, D., Biedermann, F., and Scherman, O. A. (2012). Orthogonal switching of a single supramolecular complex. *Nature Communications*, 3:1207.

- Tokunaga, M., Imamoto, N., and Sakata-Sogawa, K. (2008). Highly inclined thin illumination enables clear single-molecule imaging in cells. *Nature Methods*, 5(2):159–161.
- Uetz, P., Giot, L., Cagney, G., Mansfield, T. A., Judson, R. S., Knight, J. R., Lockshon, D., Narayan, V., Srinivasan, M., Pochart, P., Qureshi-Emili, A., Li, Y., Godwin, B., Conover, D., Kalbfleisch, T., Vijayadamar, G., Yang, M., Johnston, M., Fields, S., and Rothberg, J. M. (2000). A comprehensive analysis of protein-protein interactions in *Saccharomyces cerevisiae*. *Nature*, 403(6770):623–627.
- Ulbrich, M. H. and Isacoff, E. Y. (2007). Subunit counting in membrane-bound proteins. *Nature Methods*, pages 1–3.
- Verstraete, K., van Schie, L., Vyncke, L., Bloch, Y., Tavernier, J., Pauwels, E., Peelman, F., and Savvides, S. N. (2014). Structural basis of the proinflammatory signaling complex mediated by TSLP. *Nature Structural & Molecular Biology*, 21(4):375–382.
- Wolff, M., Mittag, J. J., Herling, T. W., Genst, E. D., Dobson, C. M., Knowles, T. P. J., Braun, D., and Buell, A. K. (2016). Quantitative thermophoretic study of disease-related protein aggregates. *Scientific Reports*, 6:22829.
- Xie, X. S., Choi, P. J., Li, G.-W., Lee, N. K., and Lia, G. (2008). Single-Molecule Approach to Molecular Biology in Living Bacterial Cells. *Annual Review of Biophysics*, 37(1):417–444.
- Yu, S. R., Burkhardt, M., Nowak, M., Ries, J., Petrášek, Z., Scholpp, S., Schwille, P., and Brand, M. (2009). Fgf8 morphogen gradient forms by a source-sink mechanism with freely diffusing molecules. *Nature*, 461(7263):533–536.
- Zadeh, J. N., Steenberg, C. D., Bois, J. S., Wolfe, B. R., Pierce, M. B., Khan, A. R., Dirks, R. M., and Pierce, N. A. (2010). NUPACK: Analysis and design of nucleic acid systems. *Journal of Computational Chemistry*, 32(1):170–173.
- Zhan, H., Stanciauskas, R., Stigloher, C., Dizon, K. K., Jospin, M., Bessereau, J.-L., and Pinaud, F. (2014). In vivo single-molecule imaging identifies altered dynamics of calcium channels in dystrophin-mutant *C. elegans*. *Nature Communications*, 5:1–12.



## Associated Publications

Ferdinand Greiss, Myrto Deligiannaki, Christophe Jung, Ulrike Gaul, & Dieter Braun:

**Single-Molecule Imaging in Living *Drosophila* Embryos with Reflected Light-Sheet Microscopy**

Biophysical Journal (2016), 110(4), 939–946, <http://doi.org/10.1016/j.bpj.2015.12.035>, Copyright ©2016 Biophysical Society. Published by Elsevier Inc.

Ferdinand Greiss, Franziska Kriegel, Dieter Braun:

**Probing the Cooperativity of Binding Networks with High-Throughput Thermophoresis**

Analytical Chemistry (2017), 89(4), 2592–2597, <http://doi.org/10.1021/acs.analchem.6b04861>, Copyright ©2017 American Chemical Society.



## Article

# Single-Molecule Imaging in Living *Drosophila* Embryos with Reflected Light-Sheet Microscopy

Ferdinand Greiss,<sup>1</sup> Myrto Deligiannaki,<sup>2</sup> Christophe Jung,<sup>2</sup> Ulrike Gaul,<sup>2</sup> and Dieter Braun<sup>1,\*</sup><sup>1</sup>System Biophysics, Department of Physics and <sup>2</sup>Gene Center, Department of Biochemistry, Center of Protein Science CIPSM, Ludwig Maximilians University, Munich, Germany

**ABSTRACT** In multicellular organisms, single-fluorophore imaging is obstructed by high background. To achieve a signal/noise ratio conducive to single-molecule imaging, we adapted reflected light-sheet microscopy (RLSM) to image highly opaque late-stage *Drosophila* embryos. Alignment steps were modified by means of commercially available microprisms attached to standard coverslips. We imaged a member of the septate-junction complex that was used to outline the three-dimensional epidermal structures of *Drosophila* embryos. Furthermore, we show freely diffusing single 10 kDa Dextran molecules conjugated to one to two Alexa647 dyes inside living embryos. We demonstrate that Dextran diffuses quickly ( $\sim 6.4 \mu\text{m}^2/\text{s}$ ) in free space and obeys directional movement within the epidermal tissue ( $\sim 0.1 \mu\text{m}^2/\text{s}$ ). Our single-particle-tracking results are supplemented by imaging the endosomal marker Rab5-GFP and by earlier reports on the spreading of morphogens and vesicles in multicellular organisms. The single-molecule results suggest that RLSM will be helpful in studying single molecules or complexes in multicellular organisms.

## INTRODUCTION

The high autofluorescence background present in living animals usually obstructs single-molecule imaging with wide-field microscopy. For the purpose of reducing this background, several techniques have been developed that are able to excavate the signal from dim light sources. With its excellent signal/noise ratio (SNR), total-internal-reflection microscopy is widely used for single-molecule studies in vitro and to observe membrane-associated events at the single-molecule level in vivo (1,2). Although out-of-focus signal is greatly reduced by the selective excitation of only a few hundred nanometers, total-internal-reflection microscopy is intrinsically restricted to image regions near a refractive index mismatch. Highly inclined laminated microscopy was developed for three-dimensional (3D) single-molecule imaging within single cells and has been shown to be able to detect single membrane proteins in living animals by virtue of optimized protein labeling (3). Difficulties arise, however, when an attempt is made to image dense regions where the increased highly inclined laminated microscopy light-sheet thickness lowers the SNR (4).

We believe that the development of novel microscopic techniques with optimized detection and illumination efficiency will bring new information about the connection between stochastic single-molecule behavior and multicellular pattern formation. Moreover, studying stochastic events in naturally embedded cells that have previously only been

studied in cell culture will bring us closer to authentic observations.

Originally developed for imaging morphogenetic processes on a multicellular scale (5), light-sheet microscopy (LSM) offers the most promising addition to single-molecule imaging techniques (6–10). Several groups have been able to demonstrate protein binding to DNA in the nucleus of salivary gland cells (7) and stem cell spheroids (6). Samples are optically sectioned via sheet-like excitation volumes parallel to the focal plane of the detection objective. The orthogonal arrangement of the illumination and detection objectives restricts the use to low to medium numerical-aperture objectives that result in a poor photon transmission efficiency. Maximizing photon yield is, however, crucially needed for single-molecule imaging.

We adapted the principles of reflected LSM (RLSM) as introduced by Gebhardt et al. (8) and recently implemented as single-objective RLSM (or single-objective selective-plane illumination microscopy) by Galland et al. (10). RLSM uses a small reflective element to circumvent the spatial limitations imposed by conventional LSM. The excitation light beam is deflected shortly after the illumination objective onto the focal plane of a detection objective.

In this report, we show that the alignment can be readily performed with commercially available microprisms that are attached to standard microscope coverslips (custom made by Optikron, Jena, Germany). Thus, samples can be placed directly onto the disposable platform without time-consuming handling or preparation. In fact, we reconstructed the 3D epidermal structure and, moreover, were able to observe single Dextran-Alexa647 molecules in the

Submitted October 9, 2015, and accepted for publication December 28, 2015.

\*Correspondence: dieter.braun@lmu.de

Editor: David Wolf.

© 2016 by the Biophysical Society  
0006-3495/16/02/0939/8



<http://dx.doi.org/10.1016/j.bpj.2015.12.035>

surrounding of the epidermis of living and highly opaque late-stage *Drosophila* embryos.

## MATERIALS AND METHODS

### Optical setup

Two laser lines were collinearly aligned via mirror and dichroic beam splitter (488 nm, 50 mW 488-50 Sapphire, Coherent, Santa Clara, CA; 642 nm, 140 mW LuxX642, Scienta Omicron, Taunusstein, Germany). Laser lines were modulated by an acousto-optical tunable filter (AOTF:4C-VIS-TN, Optoelectronics, Hawthorne, CA) within a few microseconds and triggered with the camera TTL exposure output signal. The beam was collimated after the optical fiber by a reflective collimator (RC04FC-P01, Thorlabs, Newton, NJ) to a beam diameter of 4 mm. A cylindrical 5× Keplerian beam telescope expanded the beam diameter (cylindrical achromatic doublets 50/250 mm; ACY254-050-A/ACY254-250-A, Thorlabs). A spherical aperture (SM1D12C, Thorlabs) further controlled the final beam diameter (4–12 mm) and, hence, the light-sheet thickness. A single cylindrical lens (150 mm cylindrical achromatic doublets, ACY254-150-A, Thorlabs) conjugated the back focal plane of a 20×, 0.95 NA water-immersion objective (working distance 2 mm;

XLUMPLFL20XWIR, Olympus, Center Valley, PA) to define the light-sheet width (Fig. 1). The entire optical illumination block was moved with an XYZ manual translation stage (PT3/M, Thorlabs) on a custom-made breadboard that was attached to a commercial inverted Zeiss microscope (Axiovert Observer D1.m, Carl Zeiss, Oberkochen, Germany).

The coverslip (no. 1.5, 22 × 60 mm, Menzel, Berlin, Germany) with custom-attached 500 × 500 × 500- $\mu\text{m}$  micro prism (Optikron) was placed under the microscope to reflect the illumination beam onto the focal plane of a high-NA water-immersion objective (40×, 1.25 NA, CFI Apochromat 40× WI Lambda-S, Nikon, Tokyo, Japan). Collected fluorescent signal was cleaned by a double-color emission filter for 642 nm and 488 nm (ZET488/640, AHF Analysentechnik, Tübingen, Germany) and projected onto the electron-multiplying charge-coupled device camera (Cascade II 512, Photometrics, Tucson, AZ) after further 2.5× magnification (2.5× C-Mount Adaptor, Carl Zeiss).

### Light-sheet characterization

Light-sheet profiles were obtained by imaging the beam without reflection by the microprism. By moving along the propagation direction of the illumination beam in a stepwise manner, cross sections at every position were extracted and fitted to width  $(x, w) = a \exp(-2(x - b)^2/w^2) + d$ , where  $b$  is the lateral shift,  $d$  the baseline,  $w$  the width of the Gaussian beam,

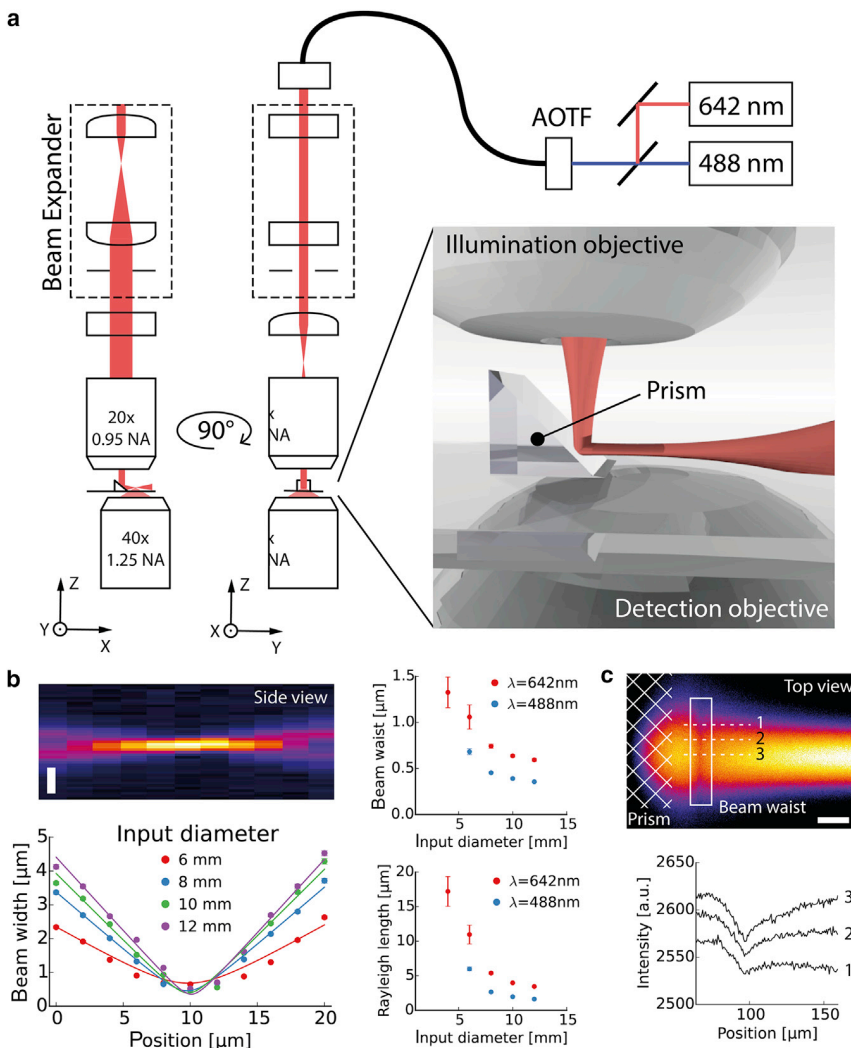


FIGURE 1 Optical setup. (a) Schematic depicting the optical setup of our reflected-light-sheet microscope (RLSM). The 642 nm and 488 nm laser lines are modulated via AOTF and coupled into the optical system. A cylindrical beam expander forms an elliptical beam profile that is dynamically controlled by the beam input diameter. The third cylindrical lens conjugates the back focal plane of the illumination objective. The light sheet is reflected via a microprism onto the focal plane of a high-NA detection objective. The setup is illustrated from two different directions to highlight the elliptical beam geometry. (b) Raw data for the measured light-sheet profile along the propagation direction every 2  $\mu\text{m}$  without reflection at 488 nm. Vertical scale bar, 2  $\mu\text{m}$ . Gaussian beam propagation and fits are shown for 488 nm and four different beam input diameters. Beam waist and Rayleigh length were extracted from fits for both wavelengths. (c) Imaging of the light sheet after reflection of the microprism in Cy5 in water. Line profiles are shown for three different positions along the light-sheet width. Scale bar, 40  $\mu\text{m}$ .

$a$  the amplitude, and  $x$  the position. The extracted beam widths at different  $z$ -positions were then fitted to Gaussian beam propagation. Beam waist and Rayleigh length were extracted with width  $(z, \lambda) = w \sqrt{1 + ((z - b)/(\pi w^2/\lambda))^2}$  and  $f(w, \lambda) = 2 \pi w^2/\lambda$ , where  $b$  is the lateral shift,  $z$  the propagation position,  $\lambda$  the wavelength, and  $w$  the beam waist, respectively. All fits were performed with a nonlinear least-square algorithm implemented in SciPy (11).

### 3D volume imaging

*Drosophila* embryos endogenously expressing green-fluorescent-protein (GFP)-tagged neuroglian were raised at 25°C and prepared according to established protocols. Briefly, embryos were picked at embryonic stages 14–15, dechorionated for 5 min with 50% household bleach, washed with H<sub>2</sub>O, and placed on a fresh grape juice agar stripe. Single embryos were placed on a coverslip with their anterior or posterior site pointing toward the capillary holder. A mounted 180  $\mu\text{m}$  capillary (TSP180350, Optronis, Kehl, Germany) with heptane glue was then slowly moved toward the embryo and lifted after a few seconds of drying time. A motorized linear actuator ( $z$  steps of 0.5  $\mu\text{m}$ ; Z625B, Thorlabs) controlled the custom-made capillary holder along the  $z$ -direction. The camera exposure time was set to 50 ms with 2500 Gain. The power of the 488 nm illumination laser was kept at 130  $\mu\text{W}$  ( $\sim 130 \text{ W/cm}^2$ ). Images were analyzed and visualized with Fiji (ImageJ) and the plugin Volume Viewer.

### In vivo single-molecule experiments

In typical injection experiments, embryos are dechorionated and covered with halocarbon oil to prevent dehydration while supplying sufficient oxygen. To accommodate the use of the water-dipping illumination objective, the injection protocol (12) was modified as follows: *pasifloral* <sup>$\Delta$</sup>  embryos (13) expressing GFP-tagged neuroglian were picked at the syncytial blastoderm stage, placed on a double-sided tape, and desiccated for 10 min. Embryos were covered with halocarbon oil to avoid further desiccation and injected with a solution of 1  $\mu\text{g}/\mu\text{L}$  10 kDa Dextran-Alexa Fluor 647 in PBS (1 $\times$  phosphate-buffered saline, Life Technology, Carlsbad, CA). After the injection, the embryos were placed in a dark and humid chamber to incubate for  $\sim 20$  h until they had reached embryonic stages 14–15. Embryos were carefully washed with *n*-heptane in a collection vial to remove residual halocarbon oil, rinsed three times with PBTw buffer (phosphate-buffered saline with 0.1% Tween 20), and further processed as described in the previous section. Under wide-field microscopy, the gut morphology served as a marker for the final staging (stages 15 to early 16) just before the single-molecule experiments were conducted. Normally developed embryos were closely positioned with their anterior-posterior axis parallel to the micropipette without overlapping with each other. All steps of this procedure, except for the imaging, were carried out at 18°C. The following fly strains were obtained from published sources: *pasifloral* <sup>$\Delta$</sup>  (13), GFP-trap Nrg<sup>G00305</sup> (14), *paired-Gal4*, and *UAS-Rab5-GFP* (Bloomington *Drosophila* Stock Center, Bloomington, IN). All strains were raised at 25°C.

Camera settings were chosen to optimize image quality (50 ms exposure time, 3800 gain, 1 $\times$  binning, frame shift with 10 MHz read-out speed). The laser intensity was set to 60  $\mu\text{W}$  ( $\sim 60 \text{ W/cm}^2$ ) at 488 nm and 1.4 mW ( $\sim 1.4 \text{ kW/cm}^2$ ) at 642 nm. Other single-molecule studies have used comparable laser power densities (8).

### Single-particle detection and tracking

Inspired by image correlation spectroscopy (15), we propose a Gaussian window filter in the frequency space to simplify the automatic spot detection. The filtering removed the immobile fraction and bleaching kinetics. For this purpose, image stacks were fast-Fourier transformed (FFT), multi-

plied with the transmission window,  $w(f) = (1 - \exp(-f^2/(2 \text{cut}^2)))$ , where  $f$  is the frequency and *cut* the cut-off frequency (0.08 s<sup>-1</sup>), and transformed back into real space. First, the FFT filter was benchmarked with tracks obtained from beads with 46 nm diameter (FluoSpheres 660/680, Thermo Scientific, Waltham, MA) diffusing in water. Settings were chosen to obtain similar raw images as acquired during *Drosophila* imaging (50 ms exposure time, 0 gain, 1 $\times$  binning, frame shift with 10 MHz read-out speed). All the spots and tracks were then extracted from image sequences with TrackMate (16).

Next, the cumulative distribution of jump distances extracted from *Drosophila* embryos was fitted to four different models (Eqs. 1 and 2) with incremental species components (6) and compared using residuals between predicted and actual data:

$$CDF(r, \tau) = 1 - \sum_{i=1}^N A_i \exp(-r^2/(4 D_i \tau)) \quad (1)$$

$$\sum_{i=1}^N A_i = 1, \quad (2)$$

where  $D_i$  and  $A_i$  are the diffusion coefficient and fraction of diffusive species, respectively. Mean-square displacement (MSD) curves for directional movement were fitted to the anomalous diffusion model

$$MSD = 4 D \tau^\alpha, \quad (3)$$

where  $D$  is the diffusion coefficient and  $\alpha$  is the exponent accounting for anomalous diffusion. All steps were processed with Python 2.7 and the SciPy packages for optimization, data handling, and visualization (11).

## RESULTS AND DISCUSSION

### Optical setup

The assembly of our optical setup with opposed detection and illumination objective was realized with a few custom-made and commercial parts on an inverted microscope. An autonomous illumination module with lasers, fast AOTF, and single-mode optical fiber was assembled to easily connect the light source with our optical block. We further used achromatic lenses to maintain constant dimensions of the beam input diameter across different illumination wavelengths. A maximal beam input diameter of  $\sim 12$  mm was obtained with the 5 $\times$  beam expander and the calibrated spherical aperture. A 150 mm achromatic cylindrical lens controlled the light-sheet width by conjugating the back focal plane of the illumination objective (Fig. 1 a).

We then sought to quantify the geometrical properties of the excitation light sheet with different beam input diameters. Therefore, we measured the light sheet's cross-section by projecting it without reflection onto the focal plane of the detection objective in water. By moving the detection objective across the beam waist in a stepwise fashion, we determined the beam widths at 11 different propagation depths. The reconstructed profile was fitted to Gaussian beam propagation to obtain the beam waist for different beam input diameters (Fig. 1 b). In all our single-molecule experiments, we used a 642 nm laser line for excitation,

which results in lower autofluorescence from the biological sample, and the 488 nm laser line to localize the epidermal structure. The beam input diameter was adjusted to 7 mm to create a final light sheet of  $\sim 1 \mu\text{m}$  thickness ( $\sim 11 \mu\text{m}$  Rayleigh length) at 642 nm and  $\sim 0.6 \mu\text{m}$  ( $\sim 8 \mu\text{m}$  Rayleigh length) at 488 nm wavelength. Furthermore, we visualized the light-sheet profile after reflection of the microprism by illuminating 500 nM Atto488 and Cy5 in water. By estimating the light-sheet waist position, we found that along the detection objective's focal plane, a total light-sheet tilt of  $< \sim 1.5^\circ$  was achieved (Fig. 1 c).

### 3D imaging capabilities

To investigate the ability of 3D sectioning with our optical setup, we positioned late-stage *Drosophila* embryos expressing GFP-tagged neuroglial (NrgGFP) on the tip of a microscale capillary with 180  $\mu\text{m}$  inner diameter (Fig. 2 a). Mounting the embryo with common heptane glue, as used during live imaging of *Drosophila* with a confocal microscope on the glass capillary rendered a fast, robust, and user-friendly method of micrometer positioning. We implemented a linear actuator that offered a resolution of 0.5  $\mu\text{m}$  in the  $z$ -direction, which was sufficient to obtain image stacks of the epidermal structure (Fig. 2).

It is important to note that the penetration depth is limited by light scattering as experienced with Gaussian-based

light-sheet techniques. Furthermore, the light-sheet thickness of  $\sim 1 \mu\text{m}$  provided a good SNR for single molecule imaging, but reduced the applicability on the global embryonic scale. Therefore, we primarily focused on the outer epidermal structure to test the volume-imaging capabilities of our RLSM implementation (17).

As a member of the membrane-associated septate junction (SJ) complex, neuroglial is strongly expressed and readily detected with  $13 \mu\text{W}$  ( $\sim 130 \text{ W/cm}^2$ ) at an excitation wavelength of 488 nm. As expected, NrgGFP accumulated at the apicolateral site where the properly formed SJ complex impedes free diffusion along the paracellular space (Fig. 2, b and c) (18). We further analyzed the data by measuring the intensity profile along the lateral membrane of some cells. Background-corrected intensity profiles (Fig. 2 d) show intensity peaks (200–300 counts) at 0  $\mu\text{m}$  with lower-intensity plateaus (gray bar, 50–100 counts). The roughly twofold increase of NrgGFP signal toward the apicolateral site holds true for all three spatial projections, which indicates homogeneous illumination within the region of interest.

### Single-molecule imaging in vivo

In recent years, single-molecule imaging has been successfully applied to a wide array of biological specimens ranging from the nuclei of single eukaryotic cells (6–8,10)

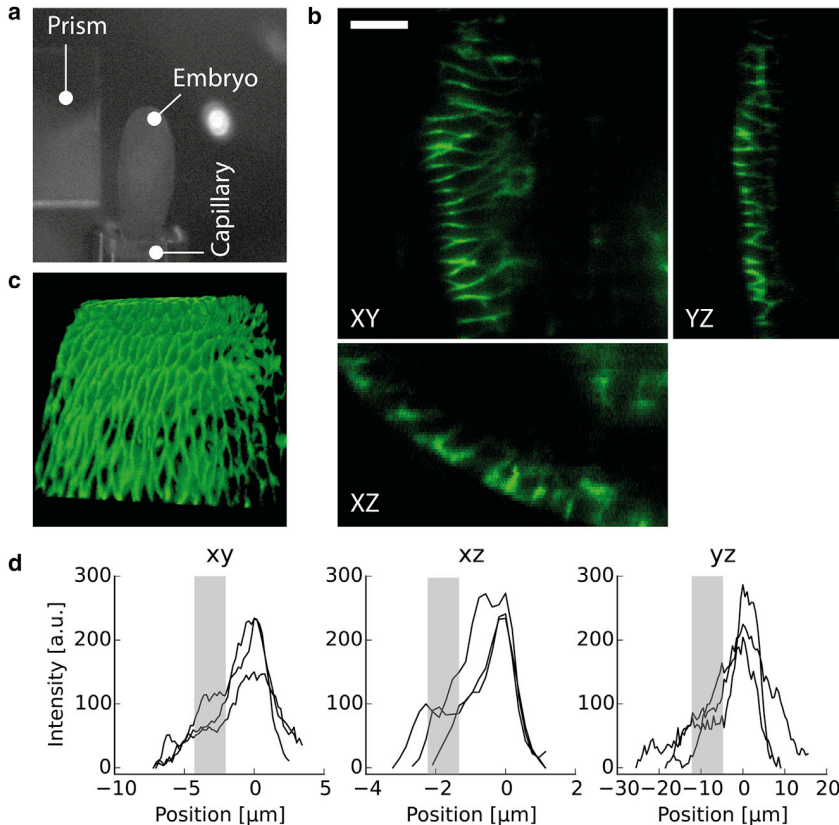


FIGURE 2 Volume imaging. (a) Positioning of *Drosophila* embryo with a capillary in front of the microprism's reflective surface. A motorized linear actuator moved the capillary and the embryo in the  $z$ -direction. (b) Orthogonal views of images acquired with 0.5  $\mu\text{m}$  resolution along the  $z$ -direction. Scale bar, 10  $\mu\text{m}$ . NrgGFP accumulates at the apicolateral site of epithelial cells to hinder free diffusion along the paracellular space. (c) Reconstructed 3D volume of the epidermal structure. Single cells were readily resolved with RLSM. The  $\sim 1 \mu\text{m}$  light-sheet thickness for optimal single-molecule imaging is accompanied by a limited region of homogeneous illumination (Fig. 1, b and c). Thus, we restricted the 3D volume imaging on the outer epidermal layer. (d) Line profiles along the cell-cell junction reveal an  $\sim 2$ -fold increase in the NrgGFP signal at the apicolateral site (0  $\mu\text{m}$ ) compared to what we found at the basolateral site (gray bar) in all three directions of space.

to membrane proteins in *Caenorhabditis elegans* (3). To test whether we could detect freely diffusing single molecules in the highly opaque *Drosophila* embryo (17), we decided to follow known paths and introduced a solution of 10 kDa Dextran as a single-molecule probe, since Dextran is being widely used for transportation studies in the biological context (13,19,20).

We first confirmed that single molecules of Dextran-Alexa647 are indeed detectable in living *Drosophila* embryos, and in a second step, we addressed questions regarding the diffusive behavior of Dextran on the multicellular scale. To this end, syncytial blastoderm embryos were collected and immediately injected with 10 kDa Dextran-Alexa647 and placed in a dark humid chamber. Embryos were staged (15 h after egg laying) and individually placed in H<sub>2</sub>O with their anterior-posterior axis parallel to the microprism's reflective surface (Fig. 3 a). 3D mounting was unpractical for this purpose, because high-speed image acquisition is essential for single-molecule imaging in solution. As schematically depicted in Fig. 3 a, the light-sheet waist was positioned in the lower-left quadrant, since we expected that optical aberrations along the illumination as well as the emission path would worsen the SNR when imaging in deeper tissue (17).

Because morphogenetic movement was negligible during the timescale of imaging, the GFP and Alexa647 channels could be acquired consecutively. Again, NrgGFP (488 nm laser line for excitation with  $\sim 60$  W/cm<sup>2</sup>) was used to adjust the light sheet and the focal position of the detection objec-

tive. Due to the interdependence of SJ proteins for localization, NrgGFP is now evenly distributed along the lateral membrane in the SJ mutant *pasiflora*<sup>Δ</sup> (13) and therefore clearly outlines the epidermal structure (Fig. 3 b, center; Movie S1 in the Supporting Material).

In the Alexa647 channel, immobilized intensity spots that showed bleaching steps during the first few seconds of acquisition confirmed that we were indeed detecting single molecules in living *Drosophila* embryos (one to two dyes per Dextran according to the manufacturer). Particle locations of bleaching-step trajectories were found manually and their intensity was corrected for background signal. A locally dependent emission justifies the uneven level of signal counts for spatially separated fluorophores (Fig. 3 d).

For single-particle tracking, the immobile fraction and low-frequency bleaching kinetics were removed via FFT filtering (Fig. 4; Movie S2). Before applying the FFT filter to the biological data, we imaged and tracked 46-nm-diameter beads with and without filtered image sequences to exclude possible artifacts introduced by the proposed temporal filter. As seen in Fig. 4 b, no apparent difference between the cumulative distributions of the two data sets could be observed. Fitting the jump-distance cumulative distribution to a single-component model led to the same diffusion coefficient for both data sets ( $D_{\text{raw}} = 4.62 \pm 0.04$   $\mu\text{m}^2/\text{s}$ ,  $D_{\text{filtered}} = 4.63 \pm 0.03$   $\mu\text{m}^2/\text{s}$ ).

Single particles in *Drosophila* embryos were then detected and tracked with TrackMate after FFT filtering.

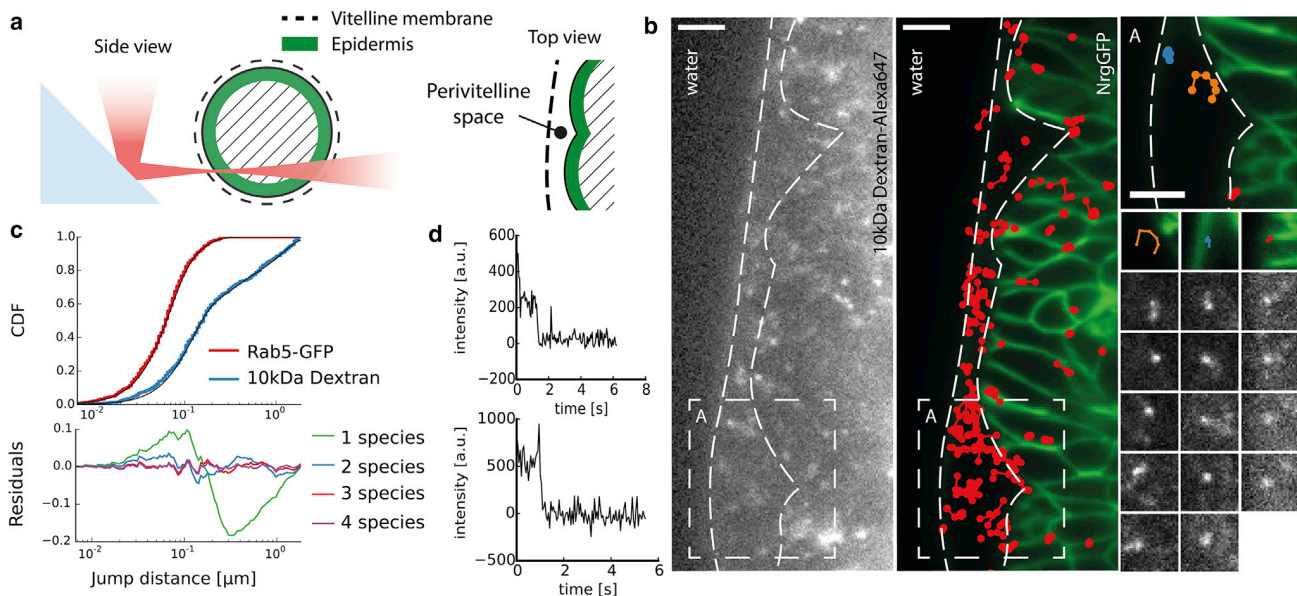


FIGURE 3 Single-molecule detection and tracking. (a) Illustration of the excitation path and cross section of the embryo at the region of interest. Imaging at the lower left quadrant of the embryo reduced optical aberrations. (b) Single raw image of 10 kDa Dextran-Alexa647 and the temporal average of NrgGFP with superimposed trajectories. Scale bar, 10  $\mu\text{m}$ . Subregion and tracks show examples for fast (left), medium (center), and slow (right) particles. Scale bar, 5  $\mu\text{m}$ . (c) Cumulative distribution function (CDF) of jump distances pooled from three different embryos and a three-component fitted model. Additionally, the CDF and a fitted curve (two-component model) are shown for Rab5-GFP particles found in the *Drosophila* embryo. (d) Example of Alexa647 bleaching steps found during the first seconds of imaging with the 642 nm laser line.

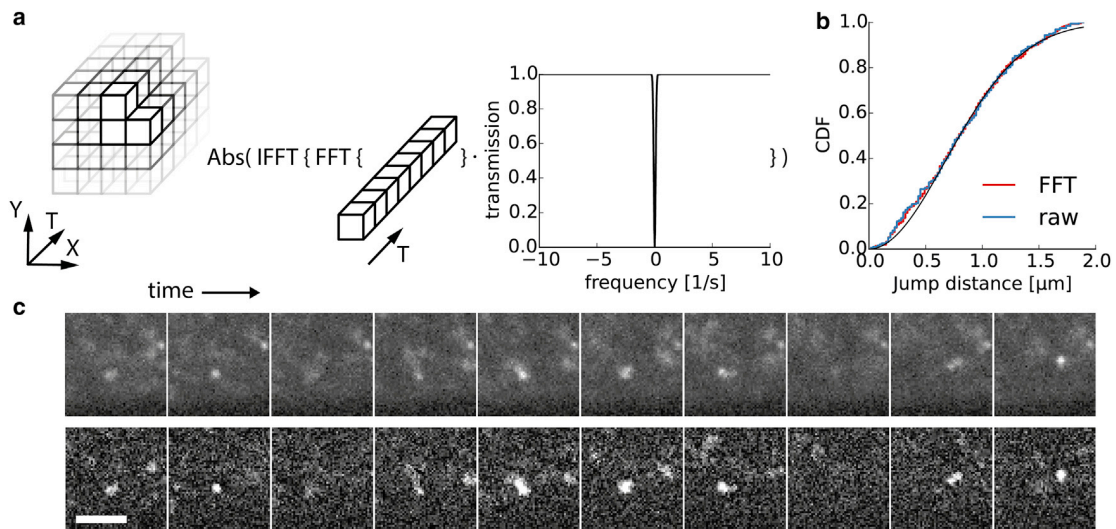


FIGURE 4 FFT filtering. (a) Every pixel in the image stack was independently processed using the temporal FFT filter. A Gaussian window was applied to remove immobile fraction and bleaching kinetics to improve the automatic spot detection. (b) CDF of freely diffusing 46-nm-diameter beads before and after FFT filtering. (c) Sequences of single frames of freely diffusing 10 kDa Dextran-Alexa647 in *Drosophila* embryos are shown for unfiltered (upper row) and filtered (lower row) movies. Scale bar, 5  $\mu\text{m}$ . To see this figure in color, go online.

Particles were excluded from further analysis when exceeding a certain size (diameter  $>1.84 \mu\text{m}$ ) or tracks being outside of the expected lifetime range (3 frames  $\leq$  included tracks  $\leq$  30 frames). The cumulative jump-distance distribution for all tracks was fitted to models consisting of 1, 2, 3, or 4 diffusive components. We found that our data were best described by a three-component model without overfitting, as indicated by the calculated residuals (Fig. 3 c;  $A_1 = 0.56$  with  $D_1 = 0.068 \pm 0.001 \mu\text{m}^2/\text{s}$ ,  $A_2 = 0.16$  with  $D_2 = 0.520 \pm 0.032 \mu\text{m}^2/\text{s}$ , and  $A_3 = 0.28$  with  $D_3 = 6.404 \pm 0.072 \mu\text{m}^2/\text{s}$ ).

To investigate the spatial distribution of fast-, medium-, and slow-diffusing components, we calculated the apparent diffusion coefficient for a time lag of 50 ms, averaged over all equally spaced time lags in each track, and superimposed the color-coded mean track position onto the temporal averaged NrgGFP image stack. Diffusion coefficients are plotted on a log scale to account for the wide range of values (Fig. 5 a). It appears that fast tracks ( $\sim 6.4 \mu\text{m}^2/\text{s}$ ) occur in the free space between the vitelline membrane and the epidermis. A similar diffusion coefficient of  $7 \mu\text{m}^2/\text{s}$  was reported for a 23 kDa morphogen in the extracellular space of living zebrafish embryos by fluorescence correlation spectroscopy (21).

In contrast, slower particles were mostly found in the epidermal structure and seemed to obey directional movement, challenging the Brownian motion model. Clearly visible and long-living candidates were manually extracted and tracked, and the MSD for every track was fitted to the anomalous diffusion model (Fig. 5, b and c) (22,23). We found that slow particles move in a directed manner (anomalous diffusion coefficient  $\alpha > 1$ ) along the cell cortex as well as the paracellular space ( $D_1 = 0.87 \pm 0.03 \mu\text{m}^2/\text{s}^{1.81}$ ,

$\alpha_1 = 1.81 \pm 0.05$ ;  $D_2 = 0.37 \pm 0.02 \mu\text{m}^2/\text{s}^{1.97}$ ,  $\alpha_2 = 1.97 \pm 0.09$ ;  $D_3 = 0.47 \pm 0.03 \mu\text{m}^2/\text{s}^{1.57}$ ,  $\alpha_3 = 1.57 \pm 0.08$ ). The slow directional movement of particles suggests active vesicle trafficking as a possible explanation. This interpretation is supported by a study that proposed dynamin-dependent vesicle transportation of morphogens ( $D = 0.10 \mu\text{m}^2/\text{s}$ ) during wing development in *Drosophila* (24). In addition, previous experimental data showed that  $\sim 80\%$  of Dextran-positive structures colocalize with the GFP-tagged endosomal marker Rab5 during cellularization of early *Drosophila* embryos (19).

To further test our theory about endosomal trafficking, we expressed Rab5-GFP and acquired image stacks of *Drosophila*. Before analysis, the image sequence was postprocessed according to the proposed FFT filter with the same frequency transmission window as used for the single-molecule tracking. We found that the transportation direction appeared to align perpendicular to the anterior-posterior embryonic axis. The same preferred directionality could be observed for the Dextran-Alexa647 particles. Moreover, similar diffusion coefficients found by the cumulative distribution (Fig. 3 c;  $A_1 = 0.78$  with  $D_1 = 0.0112 \pm 0.0001 \mu\text{m}^2/\text{s}$  and  $A_2 = 0.22$  with  $D_2 = 0.052 \pm 0.002 \mu\text{m}^2/\text{s}$ ) and the MSDs (Fig. 5 b;  $D_1 = 0.270 \pm 0.019 \mu\text{m}^2/\text{s}^{2.341}$ ,  $\alpha_1 = 2.341 \pm 0.138$ ;  $D_2 = 0.148 \pm 0.005 \mu\text{m}^2/\text{s}^{2.108}$ ,  $\alpha_2 = 2.108 \pm 0.007$ ;  $D_3 = 0.020 \pm 0.001 \mu\text{m}^2/\text{s}^{1.578}$ ,  $\alpha_3 = 1.578 \pm 0.046$ ) support our interpretation. The key problem with this comparison of fitted diffusion coefficients is due to the strong influence of the particle's transportation direction with respect to the imaging plane. Particles that translate along the light sheet will exhibit a higher diffusion coefficient than particles traversing across it.

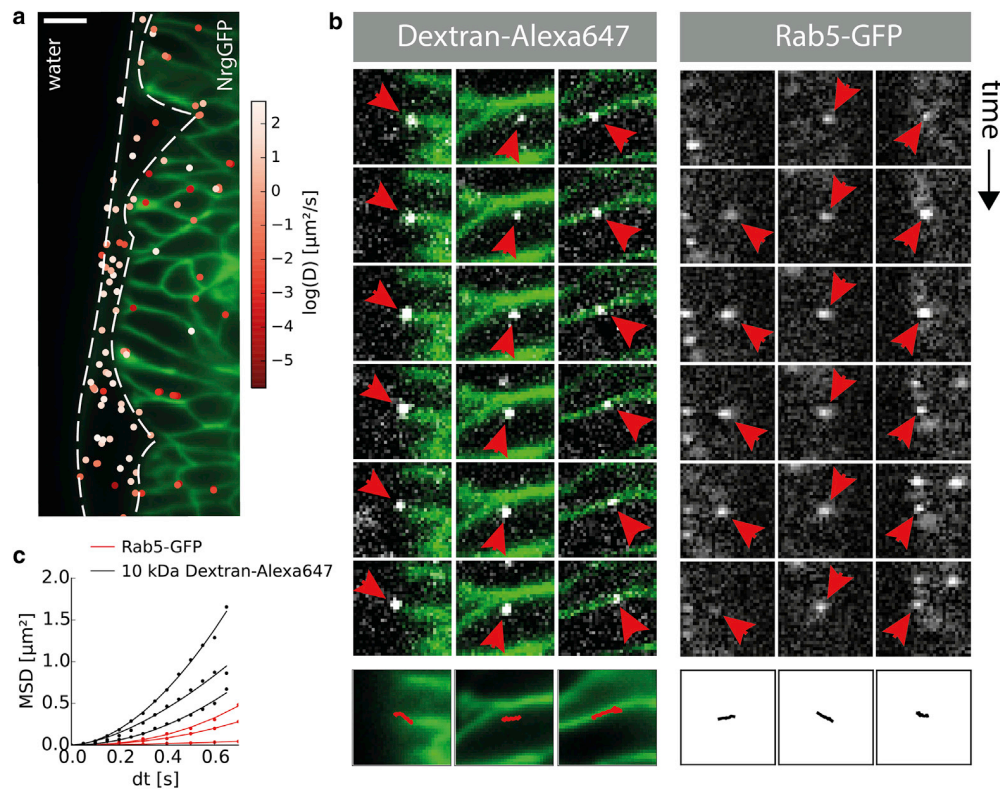


FIGURE 5 Spatial heterogeneity of diffusion. (a) Superimposed mean track position with color-coded apparent diffusion coefficient. The apparent diffusion coefficient was calculated for all equally spaced time lags of 50 ms along entire individual trajectories. Fast diffusion coefficients are mainly found in the perivitelline space. In contrast, slow particles are mostly found in the paracellular space or at the cell cortex of epidermal cells. Scale bar, 10  $\mu\text{m}$ . (b) Six representative time-lapse image sequences for particles associated with Dextran-Alexa647 (left three columns, green, NrgGFP) and Rab5-GFP (right three columns), with directional movement indicated by arrowheads. (c) Tracks were extracted and MSD curves reveal an anomalous diffusion coefficient of  $\alpha > 1$ .

## CONCLUSIONS

We report on an optical setup for imaging single molecules to entire cellular structures in 3D of living late-stage *Drosophila* embryos. Methodologically, we show that by adapting RLSM, single-molecule imaging is readily achievable even within the highly opaque *Drosophila* embryo. Using commercially available microprisms offers a user-friendly and fast way to obtain the reflective surface that is necessary for RLSM. Our setup could easily be supplemented with oil-immersion detection objectives that would, however, limit the accessible imaging depth. In principle, the same optical approach could be used for single-cell studies when grown in 3D cell culture. However, it is important to note here that RLSM techniques are currently constrained to a few micrometers above the coverslip surface and consequently make the relative positioning of mirror and sample of central importance (8,10).

We believe that the RLSM implementation presented here will not only offer an alternative to high-resolution particle-imaging techniques, e.g., spinning disk microscopy, but most importantly will provide a way to study the fundamental level of stochastic single-molecule dynamics from the multicellular perspective. In addition, more relevant

data for cell biology will be generated, since the principles of LSM give the additional advantage of reduced photobleaching and phototoxic effects (25).

## SUPPORTING MATERIAL

Two movies are available at [http://www.biophysj.org/biophysj/supplemental/S0006-3495\(16\)00042-4](http://www.biophysj.org/biophysj/supplemental/S0006-3495(16)00042-4).

## AUTHOR CONTRIBUTIONS

F.G. and D.B. constructed the optical setup and F.G. analyzed the data. F.G. and M.D. performed the experiments. F.G., M.D., C.J., U.G., and D.B. contributed to designing the experiments, discussion, and writing the manuscript.

## ACKNOWLEDGMENTS

We thank the Fabrication team of the Physics Department and Gene Center of Ludwig Maximilians Universität München, and P. Bandilla, M. Hanf, and C. Ludwig for their technical and experimental expertise.

F.G. is supported by a Deutsche Forschungsgemeinschaft Fellowship through the Graduate School of Quantitative Biosciences Munich (QBM). Financial support from SFB 1032 Project A4 (D.B.), from the Alexander von Humboldt-Professorship by the Bundesministerium für Bildung und Forschung (U.G.) is acknowledged.

## REFERENCES

1. Li, G.-W., and X. S. Xie. 2011. Central dogma at the single-molecule level in living cells. *Nature*. 475:308–315.
2. Ulbrich, M. H., and E. Y. Isacoff. 2007. Subunit counting in membrane-bound proteins. *Nat. Methods*. 4:319–321.
3. Zhan, H., R. Stanciuskas, ..., F. Pinaud. 2014. In vivo single-molecule imaging identifies altered dynamics of calcium channels in dystrophin-mutant *C. elegans*. *Nat. Commun.* 5:4974.
4. Tokunaga, M., N. Imamoto, and K. Sakata-Sogawa. 2008. Highly inclined thin illumination enables clear single-molecule imaging in cells. *Nat. Methods*. 5:159–161.
5. Huisken, J., J. Swoger, ..., E. H. Stelzer. 2004. Optical sectioning deep inside live embryos by selective plane illumination microscopy. *Science*. 305:1007–1009.
6. Chen, B. C., W. R. Legant, ..., E. Betzig. 2014. Lattice light-sheet microscopy: imaging molecules to embryos at high spatiotemporal resolution. *Science*. 346:1257998.
7. Ritter, J. G., R. Veith, ..., U. Kubitschek. 2010. Light sheet microscopy for single molecule tracking in living tissue. *PLoS One*. 5:e11639.
8. Gebhardt, J. C. M., D. M. Suter, ..., X. S. Xie. 2013. Single-molecule imaging of transcription factor binding to DNA in live mammalian cells. *Nat. Methods*. 10:421–426.
9. Friedrich, M., R. Nozadze, ..., G. S. Harms. 2009. Detection of single quantum dots in model organisms with sheet illumination microscopy. *Biochem. Biophys. Res. Commun.* 390:722–727.
10. Galland, R., G. Greci, ..., J.-B. Sibarita. 2015. 3D high- and super-resolution imaging using single-objective SPIM. *Nat. Methods*. 12:641–644.
11. Jones, E., T. Oliphant, and P. Peterson. 2007. SciPy: Open source scientific tools for Python. <http://www.scipy.org>.
12. Iordanou, E., R. R. Chandran, ..., L. Jiang. 2011. RNAi interference by dsRNA injection into *Drosophila* embryos. *J. Vis. Exp.* 50:2795.
13. Deligiannaki, M., A. L. Casper, ..., U. Gaul. 2015. Pasiflora proteins are novel core components of the septate junction. *Development*. 142:3046–3057.
14. Morin, X., R. Daneman, ..., W. Chia. 2001. A protein trap strategy to detect GFP-tagged proteins expressed from their endogenous loci in *Drosophila*. *Proc. Natl. Acad. Sci. USA*. 98:15050–15055.
15. Potvin-Trottier, L., L. Chen, ..., P. W. Wiseman. 2013. A nu-space for image correlation spectroscopy: characterization and application to measure protein transport in live cells. *New J. Phys.* 15:085006–085021.
16. Schindelin, J., I. Arganda-Carreras, ..., A. Cardona. 2012. Fiji: an open-source platform for biological-image analysis. *Nat. Methods*. 9:676–682.
17. Keller, P. J., A. D. Schmidt, ..., E. H. K. Stelzer. 2010. Fast, high-contrast imaging of animal development with scanned light sheet-based structured-illumination microscopy. *Nat. Methods*. 7:637–642.
18. Genova, J. L., and R. G. Fehon. 2003. Neuroglian, Gliotactin, and the Na<sup>+</sup>/K<sup>+</sup> ATPase are essential for septate junction function in *Drosophila*. *J. Cell Biol.* 161:979–989.
19. Fabrowski, P., A. S. Necakov, ..., S. De Renzis. 2013. Tubular endocytosis drives remodelling of the apical surface during epithelial morphogenesis in *Drosophila*. *Nat. Commun.* 4:2244.
20. Pluen, A., P. A. Netti, ..., D. A. Berk. 1999. Diffusion of macromolecules in agarose gels: comparison of linear and globular configurations. *Biophys. J.* 77:542–552.
21. Yu, S. R., M. Burkhardt, ..., M. Brand. 2009. Fgf8 morphogen gradient forms by a source-sink mechanism with freely diffusing molecules. *Nature*. 461:533–536.
22. Metzler, R., and J. Klafter. 2000. The random walk's guide to anomalous diffusion: a fractional dynamics approach. *Phys. Rep.* 339:1–77.
23. Reverey, J. F., J.-H. Jeon, ..., C. Selhuber-Unkel. 2015. Superdiffusion dominates intracellular particle motion in the supercrowded cytoplasm of pathogenic *Acanthamoeba castellanii*. *Sci. Rep.* 5:11690.
24. Kicheva, A., P. Pantazis, ..., M. González-Gaitán. 2007. Kinetics of morphogen gradient formation. *Science*. 315:521–525.
25. Pampaloni, F., B.-J. Chang, and E. H. K. Stelzer. 2015. Light sheet-based fluorescence microscopy (LSFM) for the quantitative imaging of cells and tissues. *Cell Tissue Res.* 360:129–141.

# PROBING THE COOPERATIVITY OF BINDING NETWORKS WITH HIGH-THROUGHPUT THERMOPHORESIS

Ferdinand Greiss<sup>1</sup>, Franziska Kriegel<sup>2</sup>, and Dieter Braun<sup>1,\*</sup>

<sup>1</sup>Systems Biophysics, <sup>1,2</sup>Physics Department, Nanosystems Initiative Munich and Center for NanoScience, Ludwig-Maximilians-Universität München, Amalienstraße 54, 80799 München, Germany

\*To whom correspondence may be addressed:

Prof. Dieter Braun, e-mail: [dieter.braun@lmu.de](mailto:dieter.braun@lmu.de), tel. ++49 89 - 2180 2317, fax. ++49 89 - 2180 16558

---

**ABSTRACT:** The formation of supramolecular complexes is found in many natural systems and is the basis for cooperative behavior. Here, we report on the development of a high-throughput platform to measure the complex binding behavior in 500 nl volumes and 1,536-well plates. The platform enabled us to elucidate the thermodynamic properties of a heterotrimeric DNA complex that portrays the structure of a biological relevant three-way junction. In a complementing set of cooperative networks, binding constants from ~0.1 nM to ~10  $\mu$ M were measured by sampling a high-dimensional concentration space. Each intermediate binding state was probed simultaneously with one single fluorescent dye. Through systematic base pair variations, we observed the influence of the cooperative effect on single base pair mismatches. We further found coupled binding between seemingly independent binding sites through the complex structure of the three-way junction that could not have been observed without the measurement of the entire network. These results promote automated high-throughput thermophoresis to characterize arbitrary binding networks.

---

*Keywords: high-throughput binding assay, thermophoresis, binding networks, thermodynamics*

## INTRODUCTION

The binding of two molecules is probed in high throughput by a number of automatized assays. The emergent results have given us a thorough thermodynamic understanding of bimolecular interactions. They also enriched our view on the complexity of bimolecular binding<sup>1-3</sup>. In comparison, the development of high-throughput assays to investigate the formation of supramolecular complexes is still lacking behind. Interestingly, though, researchers found that most of the protein-protein interactions in biology consist of fully connected networks with 6-7 proteins<sup>4</sup>.

In this study, we therefore describe the development of a high-throughput micro-scale thermophoresis (HT-MST) setup that is able to measure in addition to simple two molecular binding, also the formation of larger complexes in small volumes using 1,536-well plates. Unlike other methods, thermophoretic measurements do not require a size difference between fluorescent ligand and bound protein<sup>5</sup> or the immobilization of biomolecules<sup>2,3</sup>, but they give a sensitive measure for a multitude of different molecular properties. That is a combination of size, effective charge, and the hydration shell<sup>6</sup>, which can change upon binding to its partner. The measurements are performed purely optically in bulk fluid and have successfully been applied to a number of challenging experimental conditions<sup>7-17</sup>, e.g. in cell-free extract and human blood serum.

Using HT-MST, we further report on the thermodynamic properties of a positive heterotrimeric DNA binding network<sup>18</sup>. The system under study illustrates a relevant biological structure of bulged three-way junctions that describes a possible intermediate for the various processes in molecular rearrangement, repair, and recombination<sup>19</sup>. For the 3-body system, one species is defined as mediator for the binding of two other species. However, in the case of similar strong or weak intermolecular interactions between all three species, the classification of mediator is justified for each alike. Since free energy is a path-independent state function, each path from the unbound to the fully bound molecular state is equal (see details in the Supporting Information):

$$\Delta G_{AB}^o + \Delta G_{AB-C}^o = \Delta G_{CB}^o + \Delta G_{CB-A}^o = \Delta G_{AC}^o + \Delta G_{AC-B}^o \quad (1)$$

Using the principles of thermophoresis, the complete system is probed with a single fluorescently labeled species that gives distinctive information about each molecular state (Figure 1).

Thermophoretic binding measurements employ the movement of molecules along a temperature gradient that is described by the thermal mass flux  $j_{T,i} = -c_i D_{T,i} \nabla T$  where  $\nabla T$  is the local temperature gradient and  $D_{T,i}$  the thermal diffusion coefficient for species  $i$  with concentration  $c_i$ . The diffusion term  $j_{D,i} = -D_i \nabla c_i$  counteracts the thermal movement. At steady state, the total mass flux is then described by  $0 = -D_i \nabla c_i - c_i D_{T,i} \nabla T$  and integrated to give  $c_{Hot,i} = c_{Cold,i} \exp(-S_{T,i} \Delta T)$  with the ratio  $S_{T,i} = D_{T,i} / D_i$  termed the

Soret coefficient. The linearization for moderate temperature gradients leads to  $c_{T,i} = c_i (1 - S_{T,i} \Delta T)$ . Most importantly for the consideration of binding networks, the change in fluorescent signal  $\Delta F$  as experimental readout then permits the quantification of multiple molecular states because of the linear superposition principle:

$$\Delta F/F \approx \Delta T \frac{\sum_i c_i S_{T,i}}{\sum_i c_i} \quad (2)$$

As a direct consequence, the different states given by  $S_{T,i}$  and  $S_{T,j}$  with  $i \neq j$  are readily extracted and enable the complete thermodynamic mapping of systems with more than two species. However, since the movement of molecules along a temperature gradient is not fully understood, predicting the actual Soret coefficient for the different states is currently limited and has to be explored experimentally<sup>6,20-22</sup>.

With HT-MST, we could show exhaustive sampling of the otherwise prohibitive large concentration space to quantify the heterotrimeric DNA binding network in a rapid, robust, and automatized way. We were able to comprehensively resolve the complete system and study individual binding steps by orthogonal single-point mutations.

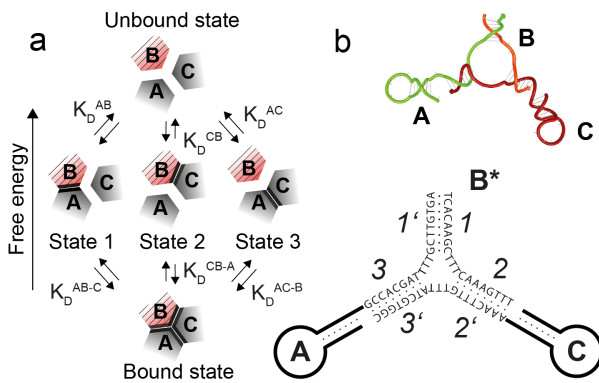


Figure 1: Heterotrimeric binding. (a) Free energy graph of reaction pathways from monomeric state, partially bound states 1, 2, and 3, to the fully bound heterotrimeric state of species A, fluorescently labeled species B, and species C. (b) Three DNA constructs with orthogonal binding sites, interdomain poly(T) junction, and hairpin structures. The poly(T) three-way junction enabled us to shorten the single-stranded regions for base pairs and hence break binding symmetries to study different heterotrimeric binding scenarios. The 3-dimensional structure was created with NUPACK.

## EXPERIMENTAL SECTION

**Building the HT-MST platform.** To build a HT-MST instrument, a standard widefield microscope was equipped with a custom-made plate holder, an infrared laser for local heating ( $\lambda=1480$  nm, 500 mW, Fibotec Fiberoptics GmbH, Germany), and three linear stages in a XYZ configuration (XY: M414, Physik Instrumente GmbH, Germany; Z: T68-636, Zaber Technologies Inc., Canada) to hold and align the entire optical setup. Optical filters and dichroic mirrors cleaned the emission and excitation (single-color LED light source; M625L2, Thorlabs Inc., USA) path; the infrared laser was coupled into the optical path with a single-mode fiber, aspheric collimator (CFC-C, Thorlabs Inc., USA) and dichroic mirror. The fluorescent signal was collected by an air objective (40x, 0.85 NA, Zeiss), focused by an infinity-corrected tube lens (ITL200, Thorlabs Inc., USA)

and imaged onto an interline CCD camera (Stingray F-145B, Allied Vision Technologies GmbH, Germany). Custom-written routines for stage control and thermophoresis experiments were implemented in LabView 2010 (National Instruments). See the Supporting Information for further details on the protocol steps during HT-MST measurements (see Figure S1 and Table S1).

We used an acoustic liquid handler (Echo 550, Labcyte Inc., USA) to generate the dilution series across the wells automatically. The droplet transfer and initial concentrations were given by home-written software in Python 2.7. The software can be provided upon request. As a first experimental step, three manual dilutions for the ligand had to be prepared because of the finite transfer droplet size with a minimum volume of 2.5 nl and a maximum volume of 500 nl sample volume. The destination 1,536-well plate (790801, Greiner Bio-One GmbH, Germany) was centrifuged after a transfer of a maximum of 64 samples for 5 sec at 1,000xg to coalesce and mix droplets. The samples were swiftly covered with 1  $\mu$ l mineral oil (HP50.2, Carl Roth, Germany) and centrifuged for 5 sec at 1,000xg for a second time. The above-mentioned steps were repeated until all concentration samples were transferred. As a final step, the microwell plate was centrifuged for 5 min at 1,000xg.

The local temperature gradient was calibrated by first measuring the average fluorescence signal of 500 nM DNA-Cy5 as function of base temperature. Then, the solution was kept constant at 28  $^{\circ}$ C and locally heated with varying infrared irradiation powers. The temperature-dependent initial fluorescence signal drop and the calibration curve for different base temperatures were used to calibrate the gradient. All shown HT-MST experiments were measured with a local temperature gradient of  $\Delta T = 8$  K.

A solution of 1  $\mu$ M DNA-Cy5 dissolved in water was used for the error measurements as function of sample volume.

**Binding of an ATP Aptamer to AMP.** Binding of ATP Aptamer and its mutant to AMP was performed with the HT-MST method as reported in literature<sup>23</sup>. Aptamer sequences were ordered from Biomers with HPLC purification (Biomers GmbH, Ulm, Germany) and mixed with a serial dilution of AMP. The dilution series was done automatically with the acoustic liquid handler. The binding curve was fitted to the analytical steady-state solution of a single reversible binding reaction<sup>9</sup> with a non-linear least square routine implemented in the scientific package SciPy.

**Probing a heterotrimeric DNA binding network.** DNA sequences (see Table S2; B: 1 + poly(T) + 2; A: 4' + HP + 4 + 3 + poly(T) + 1'; C: 5 + HP + 5' + 2' + poly(T) + 3') were ordered from Biomers (Biomers GmbH, Ulm, Germany) with HPLC purification. All species were mixed in 500 nl sample volume (137 mM NaCl, 2.7 mM KCl, 12 mM  $\text{HPO}_4^{2-}/\text{H}_2\text{PO}_4^-$ ; 1xPBS) and the fluorescently labeled species was diluted to a final concentration of 50 nM. All thermophoretic measurements were performed at 25  $^{\circ}$ C.

The orthogonal binding sites were designed with Python 2.7 and the network library NetworkX. A fully connected graph was generated with a random subset of 500 sequences out of all  $4^8$  possible sequences. Thresholds were applied to the edges between nodes (or binding sites) of the complete graph when exceeding Hamming distance and common string. The threshold was defined after empirically optimizing the number of binding sites per clique. Multiple executions of the same algorithm generated a list of cliques that were sorted according to Shannon entropy and lastly evaluated with NUPACK<sup>24</sup>.

For the final parameter optimization, the corresponding ordinary differential equations of mass action law were numerically simulated; their equilibrium steady state solutions extracted and their concentrations converted to depletion values (see Supporting Information for further details).

## RESULTS AND DISCUSSION

**High-Throughput MST Binding Assay.** To allow measurements in a high-throughput manner, we extended the already well-established technique of micro-scale thermophore-

sis (MST) using standardized 1,536-well plates. To this end, a custom-build optical setup with infrared laser, LEDs for excitation, multiple filter sets and a detection unit (CCD) was supplemented by a motorized 3-axis stage to approach individual microwells<sup>23,25</sup>.

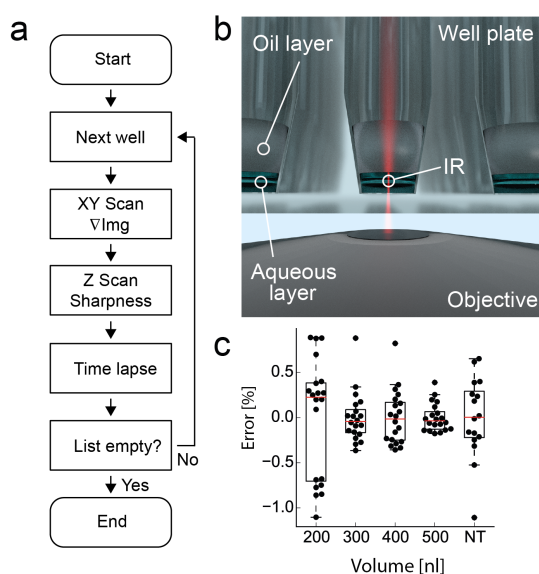


Figure 2: The principle schematic of HT-MST, workflow, and experimental results. (a) Automated workflow for each well in the 1,536-well plate. X, Y and Z scan minimized the overall measurement error. (b) Sample is covered with mineral oil and imaged from bottom. An infrared laser (IR) induces the local temperature gradient for MST measurements. (c) Total measurement error with different sample volumes and in comparison with the commercial Nanotemper (NT) instrument.

We used an acoustic liquid handler (Labcyte) to transfer nano-sized droplets (2.5 nl) into 1,536-well plates and to concurrently generate the titration of one species for the evaluation of binding constants. After the volume transfer, the plate was centrifuged to coalesce droplets and each well was manually covered with mineral oil to prevent evaporation. Furthermore, the oil layer maintained a fairly constant boundary during thermophoresis measurements. As published recently, the oil-water interface is known to induce Marangoni convection upon heating. According to numerical simulation, the thermophoretic contribution is however still pronounced and can be extracted with minor compromise<sup>25</sup>. A detailed description of all parts and protocol steps can be found in the Methods section.

Before actual thermophoretic experiments were started, each well was automatically aligned along the X, Y and Z direction in order to minimize variations across data points (~1 min for all alignment steps). Notably, the water-oil interface was observed to tilt during centrifugation and subsequently accumulated sample volume asymmetrically. The alignment along the X and Y direction was therefore implemented in a first optimization step to ensure a constant sample layer thickness at the desired region of interest. In a second step, the well border was moved into the region of interest and the image sharpness was maximized along the Z direction. The image sharpness was defined as the maximum of the normed gradient in each fluorescence slice along the acquired Z stack. Both on-

the-fly procedures proved to be robust and even helped to overcome minor initial misalignments (Figure 2 and Figure S1).

Taken together, the commercial MST setup (Monolith NT.015, Nanotemper GmbH, Germany) with standard treated capillaries and the newly developed HT-MST performed similarly well. The error was measured as the depletion deviation from the average for different well positions and capillaries as obtained by HT-MST and the commercial MST setup, respectively. Settings for both benchmarking protocols were chosen to maximize signal-to-noise while minimizing bleaching and to reach comparable depletion values (~0.8). For optimal dilution and depletion reproducibility, we continued to use a sample volume of 500 nl (Figure 2c).

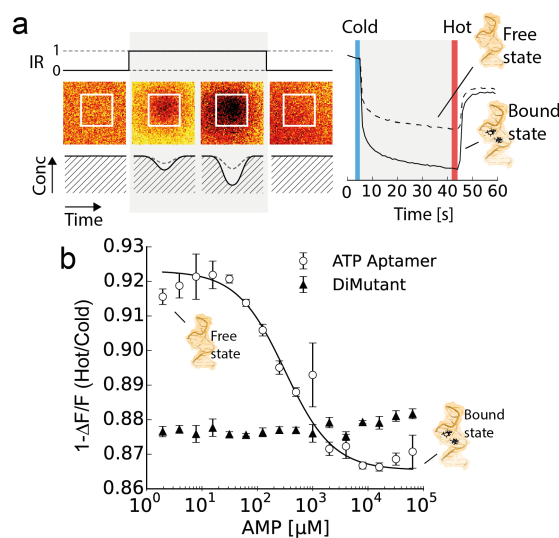


Figure 3: Binding measurement with HT-MST. (a) Time-lapse movie shows the fluorescent signal of constant labeled species with time and local IR heating between 5 and 45 sec at low and high concentrations of ligand. The signal is integrated in the indicated box. (b) The binding curve is displayed for the ATP Aptamer to adenosine-5'-monophosphate (AMP) and with the control of a dinucleotide mutant in selection buffer. Error bars represent SD (N=3).

As first realistic performance test, we measured the affinity of an ATP-Aptamer and its dinucleotide mutant to adenosine-5'-monophosphate (AMP). The *in vitro* design of aptamers provides a powerful way for the production of strongly binding receptors to arbitrary molecules of interest. We found a slightly increased dissociation constant to AMP for the ATP-Aptamer (310±40 μM versus 87±5 μM) and no detectable binding to its mutant after ~24 h of incubation<sup>23,25</sup>. The data were averaged between three different experiments. In summary, the acoustic liquid transfer, the automated dilution series, and thermophoretic measurements were optimized to give robust binding curves (Figure 3).

**Probing the heterotrimeric DNA binding network.** For this purpose, each DNA species was designed to contain two orthogonal binding sites that could bind to the reverse complement of the other species and therefore cooperatively supports the binding of the third species. In addition, two species featured a hairpin structure in order to increase the depletion resolution between free, intermediate, and fully bound states (see Figure 1b). The three species were then assembled to-

gether with the orthogonal sequences, their reverse complements, a poly(T) bridge between adjacent binding sites and the hairpin structure. As a final step, the three compiled species

were cross-checked with NUPACK<sup>24</sup> for unwanted side reactions.

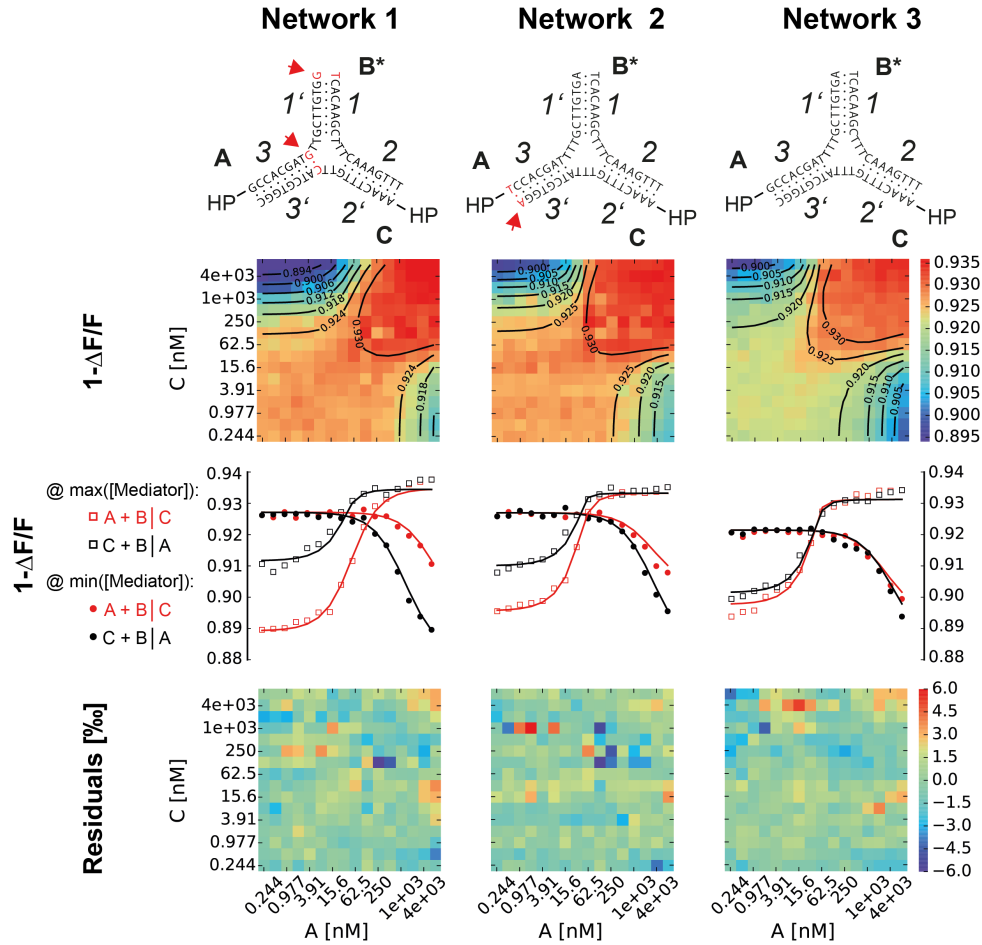


Figure 4: HT-MST data for heterotrimeric DNA binding networks. Experimental HT-MST depletion data with superimposed fit (second row, shown as black contour lines) are shown for all three DNA networks with orthogonal single-point mutations (first row, mutations highlighted in red and arrow; HP = hair pin). The parameter and error estimates are given in Table 1. Single binding curves of experimental data (squares and dots) and fits for the heterotrimeric system (lines) taken from 2-dimensional depletion data for minimal and maximal mediator (as indicated after the vertical line in the legend) concentration (third row). Unlike for low mediator concentration, a standard 2-body binding behavior can in general no longer be assumed for high mediator concentration. Fitting residuals are randomly distributed and demonstrated no systematic error between model and data (fourth row). Every final data set for each network was averaged from three independent replicates.

For the thermodynamic mapping, we developed a 2D titration scheme that superseded the widely known procedure that is commonly being used for the binding of two species. That is keeping one fluorescently labeled species at constant concentration and titrating the non-labeled species. Since the binding of heterotrimeric systems is described by 6 affinity constants and 4 Soret coefficients, we extended the data sampling from the 1-dimensional to a 2-dimensional space and increased the number of data points from 16 to 256. More precisely, the fluorescently labeled species was kept constant and the two other non-labeled species were titrated across the predicted binding constants. In this way, an orthogonal and log-spaced 2-dimensional grid in concentration space was generated (Figure 4). In spite of that we found that the 2-dimensional concentration space is sufficient for the parameter estimation,

including the spared dimension of the third species could potentially optimize the parameter estimation even further.

For the following discussion, the estimated dissociation constants were converted to Gibbs free energy with  $\Delta G_i^o = RT \ln(K_d^i)$ . Here, the thermodynamic relation of equation 1 holds within the limits of experimental errors (see Table 1 in main text and Figure S2). Assuming independent binding of two adjacent binding sites of a single DNA species, the sum of Gibbs free energy of the two individual binding sites should further equal that of the combined sites, e.g.  $\Delta G_{AB}^o + \Delta G_{AC}^o = \Delta G_{CB-A}^o$  (Figure 5).

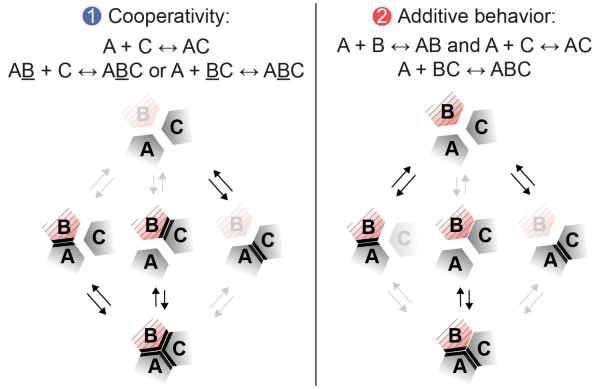


Figure 5: Example for cooperativity (left) and additive behavior of individual binding sites (right) in heterotrimeric binding networks. Cooperative binding is shown with the binding of species A to species C and species B as mediator (underlined). The additive behavior is shown for the binding of species A for each individual binding site to species C and B, respectively. The paired binding of both binding sites is shown for A to CB to form the fully bound state ABC.

First, we measured the binding of the reference DNA binding network without any mismatches (see Figure 4, Network 3). As expected, the free energy between the single binding site of the dimeric state, and the paired binding site with mediator demonstrated the expected strong cooperative effect ( $\Delta G_A^{\circ}$ : -7.5 for the binding of A+B and -8.2 for A+C;  $\Delta G_B^{\circ}$ : -7.5 for A+B and -7.3 for C+B;  $\Delta G_C^{\circ}$ : -8.2 for A+C and -7.3 for C+B;  $\Delta G_{CB-A}^{\circ}$ : -13.7;  $\Delta G_{AC-B}^{\circ}$ : -12.8;  $\Delta G_{AB-C}^{\circ}$ : -13.2; all values are given in kcal/mol; see Table 1). However, a fairly constant reduced Gibbs free energy between the paired and summed

binding sites ( $\Delta G_{CB-A}^{\circ} - \sum \Delta G_A^{\circ} = 2.0$ ;  $\Delta G_{AC-B}^{\circ} - \sum \Delta G_B^{\circ} = 2.0$ ;  $\Delta G_{AB-C}^{\circ} - \sum \Delta G_C^{\circ} = 2.3$ ; all values in kcal/mol) was found to contradict the assumption about independent binding sites. This deviation can be explained by the loss in conformational flexibility of the poly(T) junction through the transition to the heterotrimeric state. Other studies supportingly showed that bulged DNA three-way junctions could further stabilize the heterotrimeric complex by an extension of the single-stranded region<sup>26</sup>.

By exchanging one single base pair of C:G with one base pair of A:T at the 3 and 3' binding site (Network 2; Figure 4; Table 1), we could show the expected reduction in binding affinity between species A and C. Interestingly, a single base pair mismatch introduced an affinity loss that was found to be fully counterbalanced by the cooperative effect of the mediator species B in this case. This observation further confirmed that the proposed titration scheme is able to inclusively resolve the remaining 2-Body binding that is not directly accessible by the fluorescence readout (see Figure 1a, state 3). The fitted binding constant was verified through the direct labeling of species A and a standard binding curve between species A-Cy5 and species C ( $\Delta G_{AC}^{\circ} = -7.6 \pm 0.04$  kcal/mol; see Figure S3). Again, the free energy between the two single binding sites and mediator proved the expected cooperative binding energy ( $\Delta G_A^{\circ}$ : -7.5 for A+B and -7.7 for A+C;  $\Delta G_B^{\circ}$ : -7.5 for A+B and -7.5 for C+B;  $\Delta G_C^{\circ}$ : -7.7 for A+C and -7.5 for C+B;  $\Delta G_{CB-A}^{\circ}$ : -12.4;  $\Delta G_{AC-B}^{\circ}$ : -13.0;  $\Delta G_{AB-C}^{\circ}$ : -13.4; all values in kcal/mol; see Table 1). The deviation from a simple additive behavior of binding site energies is in the same range as observed for Network 3 and supports our initial conclusion ( $\Delta G_{CB-A}^{\circ} - \sum \Delta G_A^{\circ} = 2.8$ ;  $\Delta G_{AC-B}^{\circ} - \sum \Delta G_B^{\circ} = 2.0$ ;  $\Delta G_{AB-C}^{\circ} - \sum \Delta G_C^{\circ} = 1.8$ ; all values in kcal/mol).

**Table 1: Binding constants and Gibbs free energies for the three binding networks. The network is composed of six binding steps. The binding of A to B and C to B was further verified with the analytical steady state solution to the reversible binding of two species at low mediator concentration (results are shown in parentheses). The corresponding experimental data is shown in Figure 4. Network 3 shows the reference DNA construct without any mismatches. With Network 2, a C:G base pair was exchanged by A:T at binding site 3 and 3'. Hence, the binding affinity of species A to species C was found to reduce (lower  $\Delta G^{\circ}$  in comparison to Network 3). The binding of A to B for Network 1 is diminished compared to Network 2 and 3 through the introduction of a base mismatch at binding site 1 and 1'.**

	Network 1		Network 2		Network 3	
	$K_d$ [nM]	$\Delta G^{\circ}$ [kcal/mol]	$K_d$ [nM]	$\Delta G^{\circ}$ [kcal/mol]	$K_d$ [nM]	$\Delta G^{\circ}$ [kcal/mol]
$A + B = AB$	$9710_{-2730}^{+3310}$ (8070±3100)	-6.8 <sup>+0.20</sup> <sub>-0.17</sub>	$3180_{-490}^{+540}$ (2860±530)	-7.5 <sup>+0.10</sup> <sub>-0.09</sub>	$3000_{-390}^{+400}$ (2830±370)	-7.5 <sup>+0.08</sup> <sub>-0.08</sub>
$A + C = AC$	$520_{-190}^{+350}$	-8.6 <sup>+0.40</sup> <sub>-0.22</sub>	$2160_{-1370}^{+2190}$	-7.7 <sup>+0.60</sup> <sub>-0.38</sub>	$970_{-570}^{+1140}$	-8.2 <sup>+0.70</sup> <sub>-0.35</sub>
$C + B = CB$	$1570_{-80}^{+100}$ (1410±140)	-7.9 <sup>+0.04</sup> <sub>-0.03</sub>	$3270_{-280}^{+300}$ (2720±370)	-7.5 <sup>+0.05</sup> <sub>-0.05</sub>	$4540_{-620}^{+690}$ (4390±930)	-7.3 <sup>+0.09</sup> <sub>-0.08</sub>
$AB + C = ABC$	$0.14_{-0.05}^{+0.14}$	-13.4 <sup>+0.59</sup> <sub>-0.21</sub>	$0.14_{-0.08}^{+0.22}$	-13.4 <sup>+0.93</sup> <sub>-0.34</sub>	$0.20_{-0.09}^{+0.20}$	-13.2 <sup>+0.59</sup> <sub>-0.27</sub>
$AC + B = ABC$	$3.60_{-0.60}^{+0.60}$	-11.5 <sup>+0.10</sup> <sub>-0.10</sub>	$0.30_{-0.12}^{+0.17}$	-13.0 <sup>+0.34</sup> <sub>-0.24</sub>	$0.45_{-0.13}^{+0.28}$	-12.8 <sup>+0.37</sup> <sub>-0.17</sub>
$CB + A = ABC$	$2.20_{-0.70}^{+1.30}$	-11.8 <sup>+0.35</sup> <sub>-0.19</sub>	$0.77_{-0.32}^{+0.61}$	-12.4 <sup>+0.47</sup> <sub>-0.25</sub>	$0.09_{-0.04}^{+0.08}$	-13.7 <sup>+0.53</sup> <sub>-0.26</sub>

Finally, we sought to validate the procedure with the mutation of a second binding site and therefore introduced a base mismatch between species A and B (Network 1; Figure 4; Table 1). In order to keep an uniform total binding energy, we furthermore added a single base pair within the poly(T) bridge that neighbors binding site 3 and 3'. The estimated affinity constant increased correspondingly ( $\Delta G_A^o$ : -6.8 for A+B and -8.6 for A+C;  $\Delta G_B^o$ : -6.8 for A+B and -7.9 for C+B;  $\Delta G_C^o$ : -8.6 for A+C and -7.9 for C+B;  $\Delta G_{CB-A}^o$ : -11.8;  $\Delta G_{AC-B}^o$ : -11.5;  $\Delta G_{AB-C}^o$ : -13.4; all values in kcal/mol; see Table 1). In contrast to the first two networks, the shortening of the poly(T) bridge was mirrored by a stronger deviation from the additive free energy behavior ( $\Delta G_{CB-A}^o - \sum \Delta G_A^o = 3.6$ ;  $\Delta G_{AC-B}^o - \sum \Delta G_B^o = 3.2$ ;  $\Delta G_{AB-C}^o - \sum \Delta G_C^o = 3.1$ ; all values in kcal/mol). Again, the increased steric hindrance of the now shortened DNA three-way junction can consistently explain this stronger deviation from the assumed additive free energy relation.

## CONCLUSIONS

In this study, we developed an automatized measurement platform to quantitatively investigate binding constants in reduced sample volumes of 500 nl and in high throughput with standardized 1,536-well plates. We first used our platform to review known concepts and to compare its performance to commercial solutions. With the high-throughput data acquisition, we then proposed a titration scenario with 256 data points to investigate the formation of a heterotrimeric DNA complex with three-way junction. We screened base pair variations and mismatches within the binding sites. According to the error estimates, reliable binding constants can be given on each reaction step and thus elucidate the thermodynamic properties of the entire system using a single fluorescence dye. A ~2-fold increase in Gibbs free energy was found for the paired binding sites of each species, which is plausible with a homogenous base distribution. Strikingly, we found a coupling effect between independent binding sites that could be explained by the loss in conformational flexibility of the three-way junction in the fully bound state. The energy loss is in the range of ~2 and ~3 kcal/mol for a single-stranded region of three and two bases, respectively.

A limitation to thermophoretic measurements one has to bear in mind, is the necessity for separable Soret coefficients of the free, partially bound, and fully bound species in order to resolve the different molecular states of the interaction network.

The results as obtained from the heterotrimeric DNA binding networks, should demonstrate how HT-MST is utilized to quantify the thermodynamics of supramolecular complex formation in general. The heterotrimeric network provides one striking instance that is frequently encountered as structural intermediate and as topological analog in biological systems such as signal transduction and transcription regulation<sup>27-29</sup>. More complex networks could be studied by sampling a higher dimensional concentration space and an increase in the number of data points. In addition, multicolor detection could be used to integrate the information obtained from subnetworks in order to map a complete binding network. We believe that HT-MST eases the way for the thermodynamic investigation of many more supramolecular assemblies in the near future.

## ASSOCIATED CONTENT

### Supporting Information

The Supporting Information is available free of charge on the ACS Publications website.

A detailed description of the thermodynamics of heterotrimeric binding networks, numerical simulations, and parameter fitting, Figure S1-S3, and Table S1-S2 (PDF)

## AUTHOR INFORMATION

### Corresponding Author

Prof. Dieter Braun  
Systems Biophysics  
Ludwig-Maximilians-Universität München  
Amalienstr. 54  
D - 80799 München, Germany  
e-mail: [dieter.braun@lmu.de](mailto:dieter.braun@lmu.de)  
tel. ++49 89 - 2180 2317  
fax. ++49 89 - 2180 16558

### Author Contributions

The manuscript was written through contributions of all authors.

### Funding Sources

SFB 1032 Project A4

## ACKNOWLEDGMENT

F.G. is supported by a DFG Fellowship through the Graduate School of Quantitative Biosciences Munich (QBM). We thank E. Agerschou for critically reading the manuscript.

## ABBREVIATIONS

MST, micro-scale thermophoresis; HT-MST, high-throughput micro-scale thermophoresis; LED, light-emitting diode; CCD, charged-coupled device; AMP, adenosine-5'-monophosphate; HP, hairpin; NT, Nanotemper GmbH

## REFERENCES

- (1) Sharon, E.; Kalma, Y.; Sharp, A.; Raveh-Sadka, T.; Levo, M.; Zeevi, D.; Keren, L.; Yakhini, Z.; Weinberger, A.; Segal, E. *Nat. Biotechnol.* **2012**, *30*, 521–530.
- (2) Buenostro, J. D.; Araya, C. L.; Chircus, L. M.; Layton, C. J.; Chang, H. Y.; Snyder, M. P.; Greenleaf, W. J. *Nat. Biotechnol.* **2014**, *32*, 562–568.
- (3) Nutiu, R.; Friedman, R. C.; Luo, S.; Khrebtukova, I.; Silva, D.; Li, R.; Zhang, L.; Schroth, G. P.; Burge, C. B. *Nat. Biotechnol.* **2011**, *29*, 659–664.
- (4) Spirin, V.; Mirny, L. A. *Proc. Natl. Acad. Sci. U. S. A.* **2003**, *100*, 12123–12128.
- (5) Rossi, A. M.; Taylor, C. W. *Nat. Protoc.* **2011**, *6*, 365–387.
- (6) Reichl, M.; Herzog, M.; Greiss, F.; Wolff, M.; Braun, D. *Phys. Rev. E* **2015**, *91*, 062709–1–062709–7.
- (7) Seidel, S. A. I.; Wienken, C. J.; Geissler, S.; Jerabek-Willemsen, M.; Duhr, S.; Reiter, A.; Trauner, D.; Braun, D.; Baaske, P. *Angew. Chem. Int. Ed.* **2012**, *51*, 10656–10659.
- (8) Seidel, S. A. I.; Dijkman, P. M.; Lea, W. A.; van den Bogaart, G.; Jerabek-Willemsen, M.; Lazic, A.; Joseph, J. S.; Srinivasan, P.; Baaske, P.; Simeonov, A.; Katritch, I.; Melo, F. A.; Ladbury, J. E.; Schreiber, G.; Watts, A.; Braun, D.; Duhr, S. *Meth-*

- ods **2013**, *59*, 301–315.
- (9) Lippok, S.; Seidel, S. A. I.; Duhr, S.; Uhland, K.; Holthoff, H.-P.; Jenne, D.; Braun, D. *Anal. Chem.* **2012**, *84*, 3523–3530.
- (10) Dong, D.; Ren, K.; Qiu, X.; Zheng, J.; Guo, M.; Guan, X.; Liu, H.; Li, N.; Zhang, B.; Yang, D.; Ma, C.; Wang, S.; Wu, D.; Ma, Y.; Fan, S.; Wang, J.; Gao, N.; Huang, Z. *Nature* **2016**, *532*, 522–526.
- (11) Parker, J. L.; Newstead, S. *Nature* **2014**, *507*, 68–72.
- (12) Xiong, X.; Coombs, P. J.; Martin, S. R.; Liu, J.; Xiao, H.; McCauley, J. W.; Locher, K.; Walker, P. A.; Collins, P. J.; Kawaoka, Y.; Skehel, J. J.; Gambelin, S. J. *Nature* **2013**, *497*, 392–396.
- (13) Bhogaraju, S.; Cajanek, L.; Fort, C.; Blisnick, T.; Weber, K.; Taschner, M.; Mizuno, N.; Lamla, S.; Bastin, P.; Nigg, E. A.; Lorentzen, E. *Science* **2013**, *341*, 1009–1012.
- (14) Srinivasan, V.; Pierik, A. J.; Lill, R. *Science* **2014**, *343* (6175), 1137–1140.
- (15) Linke, P.; Amaning, K.; Maschberger, M.; Vallee, F.; Steier, V.; Baaske, P.; Duhr, S.; Breitsprecher, D.; Rak, A. *J. Biomol. Screening* **2016**, *21*, 414–421.
- (16) Jerabek-Willemsen, M.; André, T.; Wanner, R.; Roth, H. M.; Duhr, S.; Baaske, P.; Breitsprecher, D. *J. Mol. Struct.* **2014**, *1077*, 101–113.
- (17) Breitsprecher, D.; Schlinck, N.; Witte, D.; Duhr, S.; Baaske, P.; Schubert, T. In *Nucleic Acid Aptamers*; Mayer, G., Ed.; Springer New York: New York, NY, 2016; Vol. 1380, pp 99–111.
- (18) Deutman, A. B. C.; Monnereau, C.; Moalin, M.; Coumans, R. G. E.; Veling, N.; Coenen, M.; Smits, J. M. M.; de Gelder, R.; Elemans, J. A. A. W.; Ercolani, G.; Nolte, R. J. M.; Rowan, A. E. *Proc. Natl. Acad. Sci. U. S. A.* **2009**, *106*, 10471–10476.
- (19) Stühmeier, F.; Welch, J. B.; Murchie, A.; Lilley, D. *Biochemistry* **1997**, *36*, 13530–13538.
- (20) Reichl, M.; Herzog, M.; Götz, A.; Braun, D. *Phys. Rev. Lett.* **2014**, *112*, 198101.
- (21) Wolff, M.; Mittag, J. J.; Herling, T. W.; Genst, E. D.; Dobson, C. M.; Knowles, T. P. J.; Braun, D.; Buell, A. K. *Sci. Rep.* **2016**, *6*, 22829.
- (22) Maeda, Y. T.; Tlustý, T.; Libchaber, A. *Proc. Natl. Acad. Sci. U. S. A.* **2012**, *109*, 17972–17977.
- (23) Baaske, P.; Wienken, C. J.; Reineck, P.; Duhr, S.; Braun, D. *Angew. Chem. Int. Ed.* **2010**, *49*, 2238–2241.
- (24) Zadeh, J. N.; Steenberg, C. D.; Bois, J. S.; Wolfe, B. R.; Pierce, M. B.; Khan, A. R.; Dirks, R. M.; Pierce, N. A. *J. Comput. Chem.* **2010**, *32*, 170–173.
- (25) Seidel, S. A. I.; Markwardt, N. A.; Lanzmich, S. A.; Braun, D. *Angew. Chem. Int. Ed.* **2014**, *53*, 7948–7951.
- (26) Lilley, D. M. J. *Q. Rev. Biophys.* **2000**, *33*, 109–159.
- (27) Schlessinger, J.; Plotnikov, A. N.; Ibrahimi, O. A.; Eliseenkova, A. V.; Yeh, B. K.; Yayon, A.; Linhardt, R. J.; Mohammadi, M. *Mol. Cell* **2000**, *6*, 743–750.
- (28) Mantovani, R. *Gene* **1999**, *239*, 15–27.
- (29) Verstraete, K.; van Schie, L.; Vyncke, L.; Bloch, Y.; Tavernier, J.; Pauwels, E.; Peelman, F.; Savvides, S. N. *Nat. Struct. Mol. Biol.* **2014**, *21*, 375–382.

## **Supporting Information**

### **PROBING THE COOPERATIVITY OF BINDING NETWORKS WITH HIGH-THROUGHPUT THERMOPHORESIS**

Ferdinand Greiss<sup>1</sup>, Franziska Kriegel<sup>2</sup>, and Dieter Braun<sup>1\*</sup>

<sup>1</sup>Systems Biophysics, <sup>1,2</sup>Physics Department, Nanosystems Initiative Munich and Center for NanoScience, Ludwig-Maximilians-Universität München, Amalienstraße 54, 80799 München, Germany

#### **Table of Contents**

<b>The theory of heterotrimeric binding networks .....</b>	<b>2</b>
<b>Figure S1 .....</b>	<b>4</b>
<b>Figure S2 .....</b>	<b>5</b>
<b>Figure S3 .....</b>	<b>6</b>
<b>Table S1 .....</b>	<b>7</b>
<b>Table S2 .....</b>	<b>8</b>
<b>References .....</b>	<b>9</b>

## The theory of heterotrimeric binding networks

We can readily derive the thermodynamic relation of path independence from the mass action law by looking at each isolated binding step:

$$K_d^{AB} = [A][B][AB]^{-1} \quad (1)$$

$$K_d^{CB} = [C][B][CB]^{-1} \quad (2)$$

$$K_d^{AC} = [A][C][AC]^{-1} \quad (3)$$

$$K_d^{AB-C} = [AB][C][ABC]^{-1} \quad (4)$$

$$K_d^{CB-A} = [CB][A][ABC]^{-1} \quad (5)$$

$$K_d^{AC-B} = [AC][B][ABC]^{-1} \quad (6)$$

The product of the dissociation constants for the free to partially bound states 1, 2, and 3 and from the intermediate states to the fully bound state is therefore equal:  $K_d^{AB} K_d^{AB-C} = K_d^{CB} K_d^{CB-A} = K_d^{AC} K_d^{AC-B}$ . This relation holds for all heterotrimeric networks at equilibrium and is readily expanded to more complex systems. Using the Gibbs free energy  $\Delta G_i^o = RT \ln(K_d^i)$ , we finally arrive at our initial statement about path independence with:

$$\Delta G_{AB}^o + \Delta G_{AB-C}^o = \Delta G_{CB}^o + \Delta G_{CB-A}^o = \Delta G_{AC}^o + \Delta G_{AC-B}^o \quad (7)$$

The ordinary differential equations for a heterotrimeric interaction network are derived according to mass action law and further simplified to compute the association constants  $K_a^i = 1/K_d^i = k_{on}^i/k_{off}^i$  with  $k_{off}^i = 1 \text{ s}^{-1}$ .

$$[\dot{A}] = -K_a^{AB}[A][B] - K_a^{AC}[C][A] - K_a^{CB-A}[CB][A] + [AB] + [AC] + [ABC] \quad (8)$$

$$[\dot{B}] = -K_a^{AB}[A][B] - K_a^{CB}[B][C] - K_a^{AC-B}[AC][B] + [AB] + [CB] + [ABC] \quad (9)$$

$$[\dot{C}] = -K_a^{AC}[C][A] - K_a^{CB}[B][C] - K_a^{AB-C}[AB][C] + [AC] + [CB] + [ABC] \quad (10)$$

$$[\dot{AB}] = -[AB] - K_a^{AB-C}[AB][C] + K_a^{AB}[A][B] + [ABC] \quad (11)$$

$$[\dot{AC}] = -[AC] - K_a^{AC-B}[AC][B] + K_a^{AC}[C][A] + [ABC] \quad (12)$$

$$[\dot{CB}] = -[CB] - K_a^{CB-A}[CB][A] + K_a^{CB}[B][C] + [ABC] \quad (13)$$

$$[\dot{ABC}] = K_a^{AB-C}[AB][C] + K_a^{AC-B}[AC][B] + K_a^{CB-A}[CB][A] - 3[ABC] \quad (14)$$

The simulations, optimizations, and visualizations were carried out with the scientific packages implemented in Scipy<sup>1</sup>. Ordinary differential equations were solved numerically with *odeint* and pre-defined Jacobian matrix to speed up the calculations. The simulations were carried out until the steady state for all species was reached. Since species B was fluorescently labeled, the depletion at steady state is computed with  $1 - \frac{\Delta F}{F} = 1 - \left( \frac{S_{T,B}[B]}{[B]_T} + \frac{S_{T,AB}[AB]}{[B]_T} + \frac{S_{T,BC}[CB]}{[B]_T} + \frac{S_{T,ABC}[ABC]}{[B]_T} \right)$  with  $[B]_T = [B] + [AB] + [CB] + [ABC]$ . Thus, the entire system is defined with six association constants and four Soret coefficients. For optimization, we further reduced the number of free parameters and computed the value for  $K_a^{AC-B} = \frac{1}{2} \left( \frac{K_a^{CB} K_a^{CB-A}}{K_a^{AC}} + \frac{K_a^{AB} K_a^{AB-C}}{K_a^{AC}} \right)$ .

The parameters were log-scaled to further minimize scaling problems and to avoid negative values during fitting. Then, a non-linear gradient-based least square optimization routine using the Levenburg-Marquardt algorithm was employed to optimize the remaining nine parameters<sup>2</sup>. The median and  $\pm 34\%$  percentile of the bootstrap parameter distributions (see Fig. S2, SI, N=1000) were used for the parameter estimates and confidence intervals, respectively<sup>3</sup>. All 2-Body dissociation constants (see Table 1 in main text in parentheses) were evaluated at low mediator concentration ( $[\text{mediator}] \approx 0$ ) with a non-linear optimization routine and the analytical steady state solution to the reversible binding of two species<sup>4</sup>.

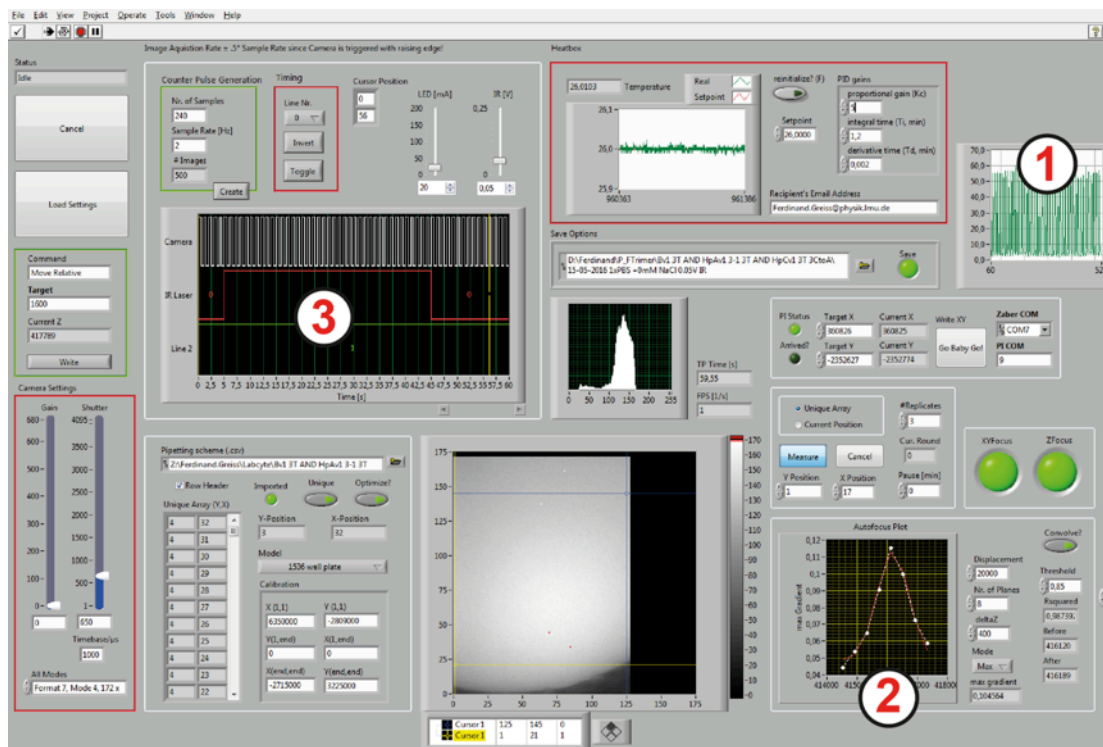


**Figure S1**

The HT-MST graphical user interface and logic was implemented in LabView 2010 (National Instruments). A list of well coordinates (unique array) is processed according to the following protocol:

1. Optimize XY position by moving along the image gradient to get a uniform fluorescent intensity
2. Optimize Z position by maximizing the image sharpness (maximal normed gradient) along the Z direction and obtain maximal image sharpness over Z by fitting a Gaussian function
3. Trigger the camera acquisition with constant LED signal and temporary local heating by infrared irradiation.

A PID system controls the sample temperature through a heating foil that is attached to the custom-made plate chamber.

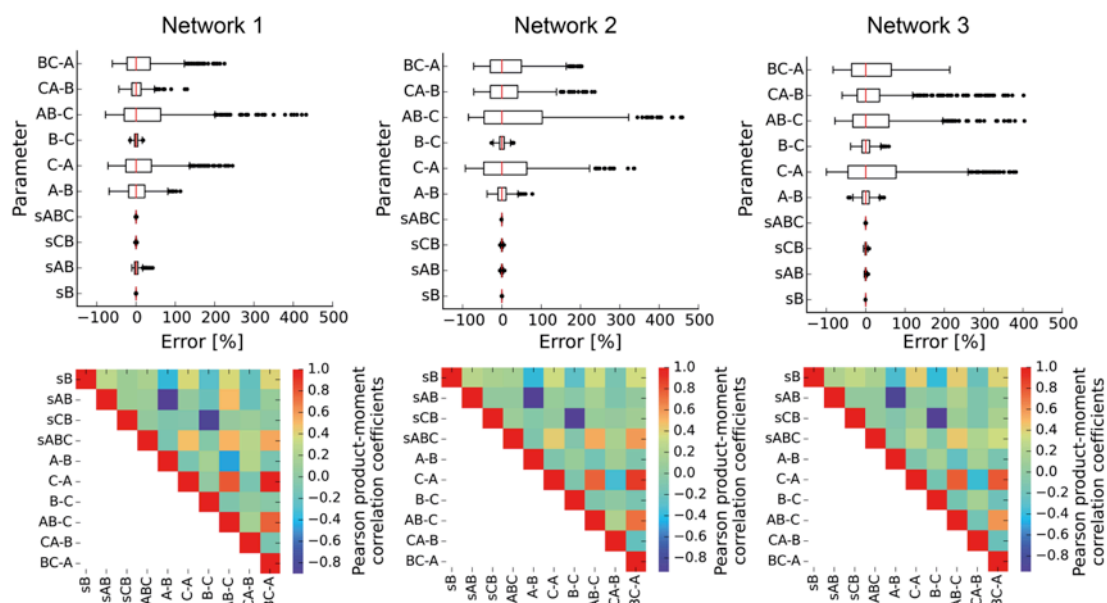


**Figure S2**

Bootstrapped parameter distribution of the three different DNA binding networks (Network 1, 2, and 3) for parameters (upper row) and their correlations (lower row).

Estimated parameter distributions for the heterotrimeric network as obtained by bootstrapping (N=1000). The optimal parameter estimate of the actual data set was used to get residuals between fit and data. Normal distributed random values with  $\mu=0$  and  $\sigma=\text{std}(\text{error})$  generated new synthetic data sets that were used to bootstrap the parameter distribution. The distributions were skewed for most of the binding affinity parameters (CB-A, AC-B, AB-C, B-C, C-A, A-B) while the different Soret coefficients (sABC, sCB, sAB, sB) demonstrated a symmetric distribution with smaller error.

The correlation matrix was estimated linearly according to Pearson's correlation with the experimentally obtained data and the bootstrapped distributions. A fairly strong correlation exists between the non-labeled species AC and the trimeric binding constants. Also, a negative correlation of the Soret coefficients of AB and CB was found that could be explained by the insufficient maximal concentration of titrated ligand (binding plateau at high ligand concentration not reached). The amount of DNA we could use was limited because of secondary low-affinity side-reactions (Fig. S3, SI).

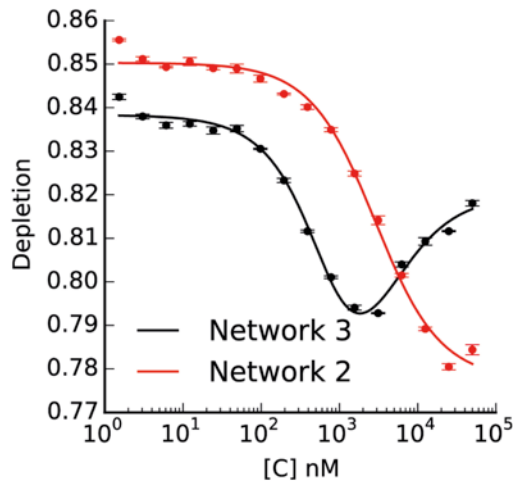


**Figure S3**

Supplementing binding curves as found by titrating species A-Cy5 (instead of labeled species B) with species C for two different binding networks. The fluorophore was attached at the 3'-end of A to minimize interference with the binding site (see Fig. 1 in the manuscript). The binding curves were measured in 1xPBS buffer at 26 °C using the commercial Monolith NT.015 (Nanotemper GmbH, Germany) and standard treated capillaries. Fluorescently labeled species A was kept at a final concentration of 500 nM. Error bars represent SD.

The binding of species A-Cy5 and species C of Network 3 displayed a second low-affinity binding (with independent binding assumed:  $K_d^{AC} = 340 \pm 160$  nM and  $K_d^{AC} = 2880 \pm 1380$  nM). We argue that the low-affinity binding does not interfere with the heterotrimeric state because of its overall high-affinity binding. The obtained binding constant from the heterotrimeric titration scheme agrees considerably ( $K_d^{AC} = 970_{-570}^{+1140}$  nM).

Also, the binding affinity between species A-Cy5 and species C of Network 2 ( $K_d^{AC} = 2610 \pm 180$  nM) agrees well with the binding constants as obtained by the proposed heterotrimeric titration scheme and fitting procedure ( $K_d^{AC} = 2160_{-1370}^{+2190}$  nM).

1	Let <i>WELLS</i> be the $n \times 2$ position matrix of $n$ wells
2	Let $\text{CONV}(image)$ be the convolution of <i>image</i> with Gaussian 3x3 kernel
3	For <i>well</i> in <i>WELLS</i> :
4	Go to <i>well</i> coordinate
5	<i>XY focus</i> = minimize $\text{grad}(\text{CONV}(image))$ with XY movement
6	Go to <i>well</i> boarder by user-defined distance
7	Acquire Z stack at equally spaced Z positions
8	<i>Z focus</i> = fit $\{\max(\ \text{grad}(\text{CONV}(image))\ \}$ over $z$ to Gaussian
9	Go to stored <i>XY</i> and <i>Z focus</i>
10	Execute MST procedure
11	Store raw images
12	End

**Table S1**

The workflow of HT-MST as described in pseudo-code.

Name	Sequence
Bv1 3xT (1,2,3)	tcacaagctttcaaagttt-Cy5
HpAv1 3xT (3)	tagggcatcgcttacaatgccctagccacgattttgcttgtga
HpAv1 3xT 3:1bp 1':-1bp (1)	tagggcatcgcttacaatgccctagccacgatGttgcttgtgG
HpAv1 3xT 3:-1bp (2)	tagggcatcgcttacaatgccctaTccacgattttgcttgtga
HpCv1 3xT(3)	gatgtcggcgcttacaccgacatcaaactttgttatcgtggc
HpCv1 3xT 3:+1bp (1)	gatgtcggcgcttacaccgacatcaaactttgttCatcgtggc
HpCv1 3xT 3:C>A (2)	gatgtcggcgcttacaccgacatcaaactttgttatcgtggA

### Table S2

DNA sequences for the three different DNA interaction networks. The poly(T) bridges are indicated with underlined characters and mutations with uppercase characters. The corresponding network for each DNA species is given in parentheses.

## References

- (1) Jones, E.; Oliphant, T.; Peterson, P. 2007.
- (2) Raue, A.; Schilling, M.; Bachmann, J.; Matteson, A.; Schelke, M.; Kaschek, D.; Hug, S.; Kreutz, C.; Harms, B. D.; Theis, F. J.; Klingmüller, U.; Timmer, J. *PLoS ONE* 2013, 8 (9), e74335.
- (3) Press, W. H. *Numerical Recipes 3rd Edition*; Cambridge University Press, 2007.
- (4) Lippok, S.; Seidel, S. A. I.; Duhr, S.; Uhland, K.; Holthoff, H.-P.; Jenne, D.; Braun, D. *Anal. Chem.* 2012, 84 (8), 3523.